SANDIA REPORT

SAND2003-4078
Unlimited Release
Printed November 2003

Ionization Coefficient Approach to Modeling Breakdown in Nonuniform Geometries

Larry K. Warne and Roy E. Jorgenson
Electromagnetics and Plasma Physics Analysis Dept.

Scott D. Nicolaysen
Integrated Surety Mechanisms Dept. 1

Prepared by
Sandia National Laboratories
Albuquerque, New Mexico 87185 and Livermore, California 94550

Sandia is a multiprogram laboratory operated by Sandia Corporation,
a Lockheed Martin Company, for the United States Department of Energy's
National Nuclear Security Administration under Contract DE-AC04-94AL85000.

Sandia National Laboratories

Issued by Sandia National Laboratories, operated for the United States Department of Energy by Sandia Corporation.

Available to DOE and DOE contractors from
U.S. Department of Energy
Office of Scientific and Technical Information
P.O. Box 62
Oak Ridge, TN 37831

Telephone: (865)576-8401
Facsimile: (865)576-5728
E-Mail: reports@adonis.osti.gov
Online ordering: http://www.doe.gov/bridge

Available to the public from
U.S. Department of Commerce
National Technical Information Service
5285 Port Royal Rd
Springfield, VA 22161

Telephone: (800)553-6847
Facsimile: (703)605-6900
E-Mail: orders@ntis.fedworld.gov
Online order: http://www.ntis.gov/help/ordermethods.asp?loc=7-4-0#online

SAND2003-4078
Unlimited Release
Printed November 2003

Ionization Coefficient Approach to Modeling Breakdown in Nonuniform Geometries

Larry K. Warne and Roy E. Jorgenson
Electromagnetics and Plasma Physics Analysis Dept.

Scott D. Nicolaysen
Integrated Surety Mechanisms Dept. 1

Sandia National Laboratories
P. O. Box 5800
Albuquerque, NM 87185-1152

Abstract

This report summarizes the work on breakdown modeling in nonuniform geometries by the ionization coefficient approach. Included are: 1) fits to primary and secondary ionization coefficients used in the modeling; 2) analytical test cases for sphere-to-sphere, wire-to-wire, corner, coaxial, and rod-to-plane geometries; a compilation of experimental data with source references; comparisons between code results, test case results, and experimental data. A simple criterion is proposed to differentiate between corona and spark. The effect of a dielectric surface on avalanche growth is examined by means of Monte Carlo simulations. The presence of a clean dry surface does not appear to enhance growth.

Contents

Figures

Tables

Intentionally Left Blank

Ionization Coefficient Approach to Modeling Breakdown in Nonuniform Geometries

1 INTRODUCTION

This report summarizes work done to model breakdown in inhomogeneous field geometries. Some general references for breakdown are [1], [2], [3], [4], [5], [6], [7], [8], [9], [10], [11], [12], [13], [14], [15]. The macroscopic approach taken here, in contrast to the microscopic kinetic modeling done as part of the investigation of dielectric surface breakdown (LDRD), is directed at obtaining an algorithm that can be efficiently implemented in complex geometries using the basic electrostatic field solution. This approach relies on the fact that, near atmospheric pressure, the electron mean free path is extremely small compared to macroscopic dimensions in typical geometries.

The field solution is obtained by application of the boundary element code EIGER_S, part of the EMPHASIS code suite of the ASCI program. Conducting and dielectric boundaries can be included in the field solution. Post-processing algorithms have been implemented to track field lines between conductors at different potentials. The user specifies starting locations (for, example, on one of the electrodes) and the algorithm adaptively follows a field line, calculating the integral of quantities dependent on the field. Alternatively, other user specified paths can be followed.

The approach implemented uses ionization coefficients, which are dependent on the field, to evaluate the breakdown condition, over the specified paths. The ionization coefficients are defined using experimental data. Air and two other gases of interest in stronglink switches (nitrogen and krypton) are considered.

Canonical problems are used for verification and validation purposes. Analytic solutions to the fields in plane-plane, coaxial, cylinder-cylinder, corner-plane, sphere-sphere, and rod-plane geometries are used for verification purposes. Because of convergence difficulties near the edge of the corner-plane gap, it was necessary to include a sub-cell integration near the edge to account for the field singularity. Experimental data for the coaxial, cylinder-cylinder, sphere-sphere, and rod-plane gaps are used for validation.

An approximate criterion, using the minimum field levels in the gap, is proposed to help distinguish between localized breakdown (corona) and bridging of the gap (spark). Comparisons are made with coaxial and rod-plane experimental air breakdown data.

Monte Carlo simulations are made to examine the affects of dielectric surface processes on ionization growth. A continuing current, simulating triple-point emissions, is used to investigate surface charging. Reference is made to some low frequency breakdown experiments on dielectric surfaces and how the results of these simulations relate to the measurements.

2 BREAKDOWN CONDITION

The condition leading to a self sustaining breakdown of the gas filled gap is summarized in this section [1]. We start with a uniform field and secondary electrons produced by ionic impact with the cathode. Secondary photon emission is introduced. Finally the streamer criterion is reviewed. The results are then generalized to nonuniform fields. A means of combining the secondary mechanisms is discussed.

2.1 Uniform Field

The uniform field is useful to review since the nonuniform field often reduces to similar formulas [1].

2.1.1 ion impact secondaries

This is the simplest case [1]. Given n_0 electrons liberated from the cathode by photons from some external source, the total number of electrons leaving the cathode are

$$n_0' = n_0 + \gamma_i \left(n - n_0'\right)$$

where $n - n_0'$ is the number of ions produced in the gas by collisions, $\gamma_i \left(n - n_0'\right)$ is the number of additional active electrons emitted at the cathode (in addition to the $n - n_0'$ neutralizing electrons). Solving for n_0'

$$n_0' = \frac{n_0 + \gamma_i n}{1 + \gamma_i}$$

These electrons avalanche producing a total number

$$n = n_0' e^{\alpha d} \tag{1}$$

at the anode a distance d away. Thus we have

$$n/n_0 = \frac{e^{\alpha d}}{1 - \gamma_i \left(e^{\alpha d} - 1\right)} \tag{2}$$

The breakdown condition for a self-sustaining discharge (where n is independent of n_0) is

$$\gamma_i \left(e^{\alpha d} - 1\right) = 1 \tag{3}$$

or

$$\alpha d = \ln\left(1 + 1/\gamma_i\right) \approx \ln\left(1/\gamma_i\right) \tag{4}$$

2.1.2 photon impact secondaries

The case where the secondary electrons are emitted from the cathode by photon impact is somewhat more complicated [1]. We denote the number of excited states per unit length due to electron collision in the field direction by θ. Letting Δ be the probability of photoelectric emission due to radiation falling on the cathode by photons from the gas and z be the number of photons falling on the cathode per unit area, we can write the number of electrons leaving the cathode per unit area as

$$n_0' = n_0 + \Delta z$$

The number of excited states produced per unit area in a slab of thickness dx is

$$n\theta dx = n_0' e^{\alpha x} \theta dx$$

The released photon flux decays as

$$I = I_0 e^{-\mu x} \tag{5}$$

Not all of these photons hit the cathode (half are traveling in the anode direction). For a three dimensional geometry of radius r we might take this fraction as

$$g = 0.5\left(1 - \frac{x}{\sqrt{x^2 + r^2}}\right)$$

In any event the differential number per unit area hitting the cathode from the slab of thickness dx is

$$dz = n_0' e^{\alpha x} \theta dx g e^{-\mu x}$$

Integration gives (ignoring the variation of g with x)

$$z = \int_0^d n_0' \theta g e^{x(\alpha-\mu)} dx = \frac{n_0' g\theta}{\alpha - \mu}\left[e^{(\alpha-\mu)d} - 1\right]$$

Thus

$$n_0' = n_0 + \frac{\Delta n_0' g\theta}{\alpha - \mu}\left[e^{(\alpha-\mu)d} - 1\right]$$

and

$$n/n_0 = \frac{e^{\alpha d}}{1 - \frac{\Delta g\theta}{\alpha-\mu}\left[e^{(\alpha-\mu)d} - 1\right]} \tag{6}$$

The breakdown condition is

$$\gamma_p\left[e^{(\alpha-\mu)d} - 1\right] = 1 \tag{7}$$

where

$$\gamma_p = \frac{\Delta g\theta}{\alpha - \mu}$$

This could be rewritten as

$$(\alpha - \mu)\, d = \ln\left(1 + 1/\gamma_p\right) \approx \ln\left(1/\gamma_p\right) \tag{8}$$

2.1.3 combination of secondary effects

When the several secondary processes are all present at once we can take

$$\gamma = \gamma_i + \gamma_p e^{-\mu d} + \cdots \tag{9}$$

where there may be others in addition to the two we discussed [1]. The breakdown condition is then

$$\alpha d = \ln\left(1 + 1/\gamma\right) \approx \ln\left(1/\gamma\right)$$

If we factor out pressure we find

$$\frac{\alpha}{p}pd = \ln\left(1 + 1/\gamma\right) \tag{10}$$

$$\gamma = \gamma_i + \gamma_p e^{-(\mu/p)pd} + \cdots \tag{11}$$

2.1.4 photoionization in gas and streamer breakdown

The case where most of the secondary electrons are produced by photons in the gas volume is now discussed [1]. If the photon energy is high enough to produce ionization in the gas, then the absorption decay length is quite short (compared to the typical gap). These photons thus produce photoelectrons in the gas without electrode interaction. A form of breakdown where this is the dominant secondary emission mechanism is brought about by the streamer.

The criterion for streamer development is not arrived at in the same way as the Townsend mechanism discussed above, but instead is determined by finding the level of ionization at which significant field distortion from space charge in the gap arises. Taking all the electrons to be in a spherical volume, with radius r, at the tip of the avalanche, the field is

$$E_r = \frac{\mathbf{e}e^{\alpha x}}{4\pi\varepsilon_0 r^2}$$

where $\mathbf{e}$ is the electronic charge magnitude. The radius can be approximated by the diffusion radius

$$r \approx \sqrt{3Dt}$$

where D is the diffusion coefficient. The transit time of the electrons can be found from the avalanche length x, and the drift velocity v_d or the electron mobility k_e

$$t = \frac{x}{v_d} = \frac{x}{k_e E}$$

Thus

$$r = \sqrt{\frac{3Dx}{k_e E}}$$

and

$$E_r = \frac{\mathbf{e}e^{\alpha x}}{4\pi\varepsilon_0 \left[3Dx/\left(k_e E\right)\right]}$$

The diffusion coefficient is found from

$$\frac{D}{k_e} = \frac{\kappa T_e}{\mathbf{e}}$$

where T_e is the electron temperature and κ is Boltzmann's constant. Using

$$\frac{3}{2}\kappa T_e = \mathbf{e}V$$

where V is the electron energy in volts, we have

$$D = \frac{2}{3} V k_e$$

$$r \approx \sqrt{2Vx/E}$$

$$E_r = \frac{\mathbf{e} e^{\alpha x}}{4\pi\varepsilon_0 \left(2Vx\right)} E \tag{12}$$

Now let x_c designate the distance at which E_r becomes comparable with E. This yields Raether's avalanche-streamer criterion [1]

$$\alpha x_c = 17.7 + \ln x_c \tag{13}$$

where x_c is in centimeters. In the uniform field the occurrence of a critical avalanche usually develops into a spark. Thus we can substitute $x_c = d$

$$\alpha d = \frac{\alpha}{p} p d = 17.7 + \ln\left(d/1 \text{ cm}\right) \tag{14}$$

2.1.5 combined mechanisms

The preceding two breakdown mechanisms could be combined by determining the gap distance d_c where the two right hand sides are equal

$$\ln\left[1 + 1/\gamma\left(d_c\right)\right] = 17.7 + \ln d_c \tag{15}$$

where d_c is in centimeters. We then use the Townsend condition for $d < d_c$ and the streamer threshold condition for $d > d_c$. Thus

$$\alpha d = F \tag{16}$$

where

$$F = \ln\left(1 + 1/\gamma\right),\ d \leq d_c$$

$$= 17.7 + \ln d_c,\ d > d_c \tag{17}$$

In this report, because we are primarily interested in gas pressures near atmospheric and sizable gaps, we sometimes ignore ionic impact [2]. This means that

$$\ln\left(1 + 1/\gamma\right) \approx \ln\left(1/\gamma_p\right) + \mu d \tag{18}$$

The photon decay is caused by gas molecule excitation in the intervening volume. For example Figure 1, taken from [1], shows the absorption coefficient for oxygen as a function of photon energy. The first continuum band (on the left side of the plot) results from dissociation of the molecule.

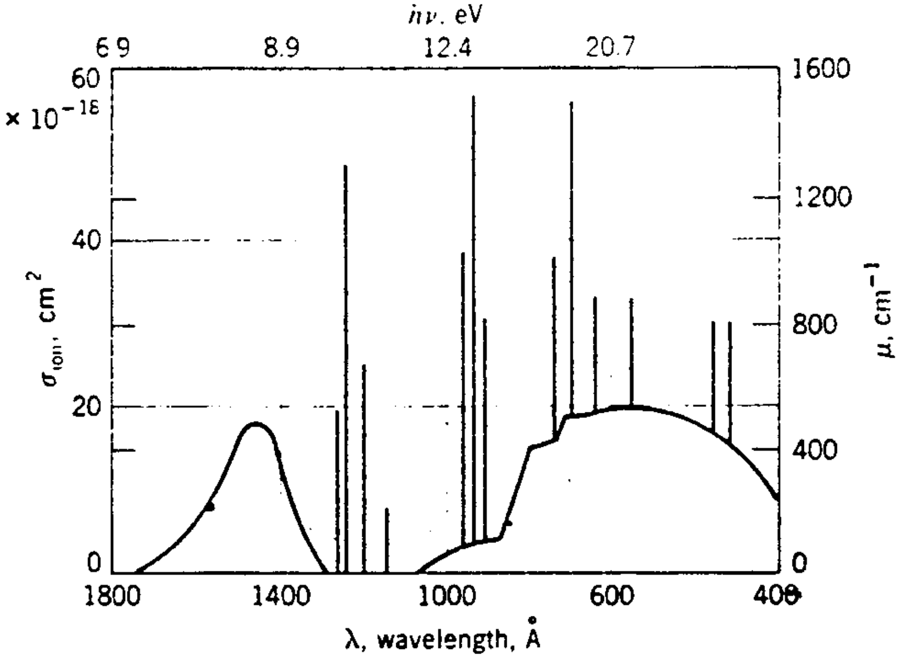

Figure 1. Absorption cross section and coefficient in oxygen as a function of photon energy (from "Fundamentals of Gaseous Ionization and Plasma Electronics," by E. Nasser [1]).

2.2 Nonuniform Field

The previous conditions are now generalized to a nonuniform field.

2.2.1 ion impact secondaries

The number of ions generalizes to [1]

$$n = n_0' e^{\int_0^d \alpha dx} \tag{19}$$

Thus we have

$$n/n_0 = \frac{e^{\int_0^d \alpha dx}}{1 - \gamma_i \left(e^{\int_0^d \alpha dx} - 1\right)} \tag{20}$$

The breakdown condition for a self-sustaining discharge (where n is independent of n_0) is

$$\gamma_i \left(e^{\int_0^d \alpha dx} - 1\right) = 1 \tag{21}$$

or

$$\int_0^d \alpha ds = \ln\left(1 + 1/\gamma_i\right) \approx \ln\left(1/\gamma_i\right) \tag{22}$$

where s describes a path in the nonuniform field.

2.2.2 photon impact secondaries

The number of excited states produced per unit area in a slab of thickness dx in this case is

$$n\theta dx = n_0' e^{\int_0^x \alpha x'} \theta dx$$

The released photon flux again decays as

$$I = I_0 e^{-\mu x}$$

where we take μ to be independent of the field and we assume that $\alpha > \mu$. The differential number per unit area hitting the cathode from the slab of thickness dx is

$$dz = n_0' e^{\int_0^x \alpha dx'} \theta dx g e^{-\mu x}$$

Integration gives (ignoring the variation of g with x if it exists)

$$z = \int_0^d n_0' e^{\int_0^x \alpha dx'} \theta g e^{-\mu x} dx = n_0' \int_0^d \frac{\theta g}{\alpha - \mu} (\alpha - \mu) e^{\int_0^x \alpha dx'} e^{-\mu x} dx \approx n_0' \theta g \int_0^d e^{\int_0^x \alpha dx' - \mu x} dx$$

Thus

$$n_0' = n_0 + n_0' \int_0^d \gamma_p \left(\alpha - \mu\right) e^{\int_0^x \alpha dx' - \mu x} dx$$

If we approximate γ_p as constant we find

$$n_0' \approx n_0 + n_0' \gamma_p \left(e^{\int_0^d \alpha dx - \mu d} - 1 \right)$$

and

$$n/n_0 = \frac{e^{\int_0^d \alpha dx}}{1 - \gamma_p \left(e^{\int_0^d \alpha dx - \mu d} - 1 \right)} \tag{23}$$

The breakdown condition is

$$\gamma_p \left(e^{\int_0^d \alpha dx - \mu d} - 1 \right) = 1 \tag{24}$$

This could be rewritten as

$$\int_0^d \alpha ds - \mu d = \ln\left(1 + 1/\gamma_p\right) \approx \ln\left(1/\gamma_p\right) \tag{25}$$

2.2.3 streamer threshold

The generalization of the streamer criterion is [1]

$$E_r = \frac{\mathbf{e} e^{\int_0^x \alpha dx'}}{4\pi\varepsilon_0 r^2}$$

The radius can be approximated by the diffusion radius

$$r \approx \sqrt{3Dt}$$

The transit time of the electrons can be found from the avalanche length x, and the drift velocity v_d or the electron mobility k_e

$$\int_0^t v_d dt' = k_e \int_0^t E dt' = k_e \left\langle E \right\rangle t = x$$

Thus

$$r = \sqrt{\frac{3Dx}{k_e \left\langle E \right\rangle}}$$

and

$$E_r = \frac{\mathbf{e} e^{\int_0^x \alpha dx'}}{4\pi\varepsilon_0 \left[3Dx/\left(k_e \left\langle E \right\rangle\right)\right]}$$

The diffusion coefficient is found from

$$\frac{D}{k_e} = \frac{\kappa \langle T_e \rangle}{\mathbf{e}}$$

where $\langle T_e \rangle$ is the mean electron temperature. Using

$$\frac{3}{2}\kappa \langle T_e \rangle = \mathbf{e} \langle V \rangle$$

where $\langle V \rangle$ is the mean electron energy in volts, we have

$$D = \frac{2}{3} \langle V \rangle k_e$$

$$r \approx \sqrt{2 \langle V \rangle x / \langle E \rangle}$$

$$E_r = \frac{\mathbf{e} e^{\int_0^x \alpha dx'}}{4\pi\varepsilon_0 \left(2 \langle V \rangle x\right)} \langle E \rangle \tag{26}$$

Now let x_c designate the distance at which E_r becomes comparable with $\langle E \rangle$ and again take $\langle V \rangle$ to be the same as used in the uniform field case. This yields

$$\int_0^{x_c} \alpha ds = 17.7 + \ln x_c \tag{27}$$

where x_c is in centimeters. If we substitute $x_c = d$ to obtain the threshold criterion

$$\int_0^{d} \alpha ds = 17.7 + \ln\left(d/1 \text{ cm}\right) \tag{28}$$

2.3 Minimum Sustaining Field

Streamers require a certain minimum field level for sustained propagation. These levels have been measured in a few gases [2] at atmospheric pressure. The level in air is [2]

$$E_{\min} \approx 4.7 \text{ kV/m} \tag{29}$$

The level in technical grade nitrogen is [2]

$$E_{\min} \approx 1.5 \text{ kV/m} \tag{30}$$

These levels increase with humidity and decrease with temperature [2].

One question of interest with regard to the above breakdown levels is whether the breakdown is localized (corona) and hence limited in current carrying capability or bridges the entire gap (spark) and capable of conducting large currents. Differentiating between these two classes of breakdown is a difficult problem involving many complicating physical phenomena [20]. These complications include: volumetric space charge in the gap, resulting in field modifications, and leader processes, resulting in low impedance extensions of the electrodes causing changes of the effective gap geometry.

We propose in this report to make use of the minimum sustaining field levels to give some clue as to whether a spark will bridge the entire gap. We propose to compare the minimum streamer sustaining field with the minimum field level existing in the gap (usually occurring between electrodes or at the larger electrode surface). The idea being that the streamer will penetrate the low field region and bridge the gap, eventually leading to gap breakdown (how wide such a gap is required to be is beyond the scope of this investigation). Comparisons will be made on some canonical problems (coaxial and rod-to-plane gaps) for which data is available to test the usefulness of this criterion. To minimize leader effects we will focus on shorter gaps (less than about 5 cm) since these are of primary interest in our applications. To reduce space charge we will only consider asymmetrical gap geometries which have one smooth electrode.

3 IONIZATION COEFFICIENTS

This section constructs fits to the ionization coefficients using experimental data.

3.1 Primary Coefficient

This section constructs simple one term fit functions for the effective primary ionization coefficient.

3.1.1 air

Although air contains oxygen (an electro-negative gas) and thus has an attachment process, we use the ionization coefficient to describe the apparent ionization including attachment. The fit function is taken as

$$\alpha/p \approx Ae^{-Bp/E} \tag{31}$$

Using two data points near the lowest E/p values available [6]

$$\alpha/p \approx 3.4 \times 10^{-5}/\,(\text{cm-T}) \;\text{ for } E/p \approx 20 \text{ V}/\,(\text{cm-T})$$

$$\alpha/p \approx 8.2 \times 10^{-3}/\,(\text{cm-T}) \;\text{ for } E/p \approx 36 \text{ V}/\,(\text{cm-T})$$

gives

$$B \approx 246.85 \text{ V}/\,(\text{cm-T}) \tag{32}$$

$$A \approx 7.79/\,(\text{cm-T}) \tag{33}$$

This fit does a reasonable job of matching data [6] at larger E/p

$$\alpha/p \approx 9 \times 10^{-2}/\,(\text{cm-T}) \text{ - fit} \approx 8.76 \times 10^{-2}/\,(\text{cm-T}) \;\text{ for } E/p \approx 55 \text{ V}/\,(\text{cm-T})$$

$$\alpha/p \approx 2.8 \times 10^{-1}/\,(\text{cm-T}) \text{ - fit} \approx 2.9 \times 10^{-1}/\,(\text{cm-T}) \;\text{ for } E/p \approx 75 \text{ V}/\,(\text{cm-T})$$

$$\alpha/p \approx 6.4 \times 10^{-1}/\,(\text{cm-T}) \text{ - fit} \approx 6.6 \times 10^{-1}/\,(\text{cm-T}) \;\text{ for } E/p \approx 100 \text{ V}/\,(\text{cm-T})$$

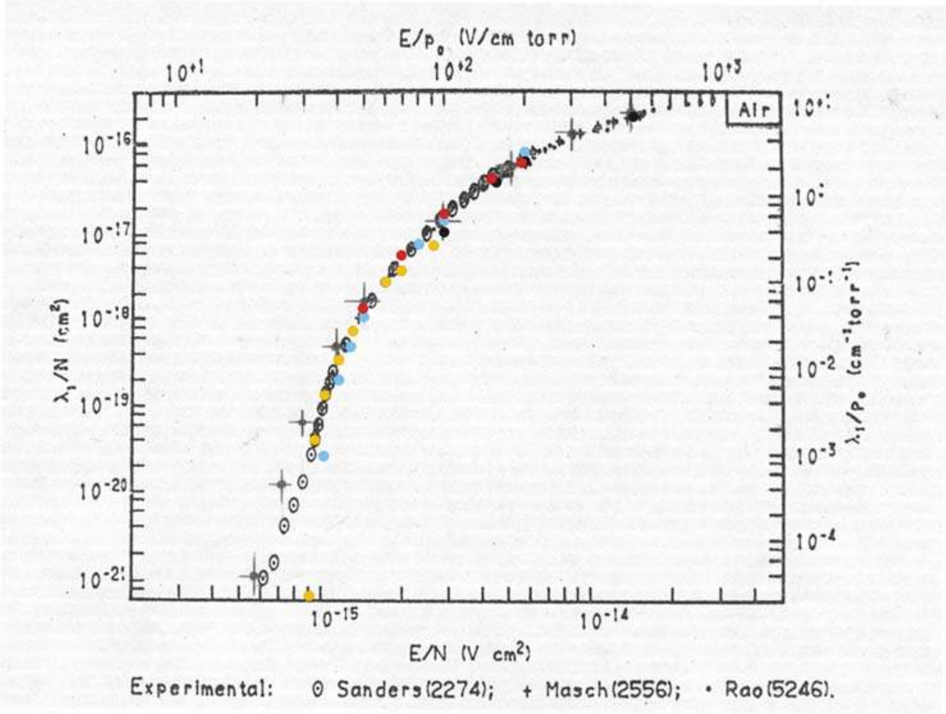

Figure 2. Comparison of experimental data (from "A Survey of Electron Swarm Data," J. Dutton [16]) with fit function predictions (large pluses with dot at center and color dots).

$$\alpha/p \approx 1.24/\,(\text{cm-T}) \text{ - fit} \approx 1.17/\,(\text{cm-T}) \text{ for } E/p \approx 130 \text{ V}/\,(\text{cm-T})$$

$$\alpha/p \approx 1.65/\,(\text{cm-T}) \text{ - fit} \approx 1.71/\,(\text{cm-T}) \text{ for } E/p \approx 163 \text{ V}/\,(\text{cm-T})$$

A second fit function [1], [2], [8] is

$$\alpha/p \approx A_1 e^{-B_1 p/E}\text{ , } 100 \text{ V}/\,(\text{cm-T}) \leq E/p \leq 800 \text{ V}/\,(\text{cm-T}) \tag{34}$$

$$A_1 = 15/\,(\text{cm-T}) \tag{35}$$

$$B_1 = 365 \text{ V}/\,(\text{cm-T}) \tag{36}$$

The intersection of the two formulas occurs at $E = E_s$

$$E_s/p = (B_1 - B)/\ln(A_1/A) \approx 180 \text{ V}/\,(\text{cm-T}) \tag{37}$$

Thus the first fit with A and B is used for (from a practical view, below the lower limit the value of α/p is negligible) 20 V/ (cm-T) $\leq E/p < E_s/p$. The second fit with A_1 and B_1 is used for $E_s/p \leq E/p \leq 800$ V/(cm-T). Figure 2, taken from [16], shows a comparison between swarm data [16] and the two fit functions (plus-dot symbols).

E/p	α'/p	η/p	$\alpha/p = (\alpha' - \eta)/p$
25.0	0.00120	0.00495	-0.00375
27.5	0.00205	0.00473	-0.00268
30.0	0.00340	0.00460	-0.00120
32.5	0.00560	0.00460	+0.00100
35.0	0.00880	0.00475	+0.00405
37.5	0.0130	0.00497	+0.0080
40.0	0.0190	0.00530	+0.0137
42.5	0.0260	0.00575	+0.0203
45.0	0.0340	0.00635	+0.0227
47.5	0.0460	0.00700	+0.0390
50.0	0.057	0.00780	+0.049
52.5	0.070	0.00870	+0.061
55.0	0.087	0.00967	+0.077
57.5	0.102	0.0108	+0.091
60.0	0.120	0.0119	+0.108
62.5	0.140		
65.0	0.170		

Table 1.Air ionization coefficients (from “High Voltage Engineering: Fundamentals,” E. Kuffel, et. al. [12]).

The agreement is reasonable and could obviously be improved by adding regions to the fit (particularly an additional fit in the $20 - 30$ V/ (cm-T) region). Many of the calculations in the report used this air ionization coefficient fit.

Alternative data in air [12] exhibits the oxygen attachment process at low values of E/p leading to negative values of the effective ionization coefficient $(\alpha' - \eta)$. Table 1 from [12] illustrates this effect.

A simple approximate fit to the tabular data is given by

$$\alpha/p \approx A_0 \left[e^{-B_0 (p/E - p/E_0)} - 1 \right] \tag{38}$$

$$A_0 = 0.005/\,(\text{cm-T}) \tag{39}$$

$$E_0/p = 31.25 \text{ V}/\,(\text{cm-T}) \tag{40}$$

$$B_0 = 200 \text{ V}/\,(\text{cm-T}) \tag{41}$$

This is shown as the yellow dots in Figure 2. This fit produces the value $-0.005/\,(\text{cm-T})$ at very low values of field (the attachment coefficient is relatively insensitive to the field in the table). This fit intersects the A_1, B_1 fit at the value

$$E_{s1}/p \approx 102 \text{ V}/\,(\text{cm-T}) \tag{42}$$

which is within its advertised range (of the A_1, B_1 fit). Thus the A_1, B_1 fit and the A_0, B_0 fit, together could be used to span the entire range of interest (switching at this intersection point). Because both of these dip below the data in Figure 2 near $E/p = 100$ V/ (cm-T), it is useful to discuss one further set.

If we use the A_0, B_0 fit for $E/p < 50$ V/ (cm-T) and the A_1, B_1 fit for $E/p > 200$ V/ (cm-T), we can match the two with the fit

$$\alpha/p \approx A_2 e^{-B_2 p/E}\ ,\ 50 \text{ V/ (cm-T)} < E/p < 200 \text{ V/ (cm-T)} \tag{43}$$

where

$$A_2 = 258.45 \text{ V/ (cm-T)} \tag{44}$$

$$B_2 = 8.805/ \text{ (cm-T)} \tag{45}$$

This fit is shown as the red dots in Figure 2.

Note that between the original A, B and A_1, B_1 fit and this final A_1, B_1, A_0, B_0, and A_2, B_2 fit we encompass all the referenced data variation. Because many of the calculations in the report used the first air ionization coefficient fit, these calculations should slightly underestimate breakdown voltages.

3.1.2 nitrogen

If we fit the function

$$\alpha/p \approx A e^{-Bp/E}$$

to two of the smallest experimental values [6]

$$\alpha/p \approx 8.7 \times 10^{-5}/ \text{ (cm-T) for } E/p = 20 \text{ V/ (cm-T)}$$

$$\alpha/p \approx 9.1 \times 10^{-4}/ \text{ (cm-T) for } E/p = 30 \text{ V/ (cm-T)}$$

we find this fit does not work well at $E/p = 50$ V/ (cm-T) [6]

$$\alpha/p \approx 3.3 \times 10^{-2}/ \text{ (cm-T) - fit} \approx 6 \times 10^{-3}/ \text{ (cm-T) for } E/p = 50 \text{ V/ (cm-T)}$$

An alternative set of fit formulas are [2]

$$\alpha/p \approx A_1 e^{-B_1 p/E}\text{, } 27 \text{ V/ (cm-T)} < E/p < 200 \text{ V/ (cm-T)} \tag{46}$$

$$A_1 = 8.8/ \text{ (cm-T)} \tag{47}$$

$$B_1 = 275 \text{ V/ (cm-T)} \tag{48}$$

$$\alpha/p \approx A_2 e^{-B_2 p/E}\text{, } 100 \text{ V/ (cm-T)} < E/p < 600 \text{ V/ (cm-T)} \tag{49}$$

$$A_2 = 12/\left(\text{cm-T}\right) \tag{50}$$

$$B_2 = 342\ \text{V}/\left(\text{cm-T}\right) \tag{51}$$

The first gives a value at $E/p = 30\ \text{V}/\left(\text{cm-T}\right)$

$$\alpha/p \approx 9.193 \times 10^{-4}/\left(\text{cm-T}\right)$$

that is close to the preceding data [6]. Thus we use these two functions in combination with a fit to the: $E/p = 20\ \text{V}/\left(\text{cm-T}\right)$ data and the $E/p = 30\ \text{V}/\left(\text{cm-T}\right)$ fit data. This approach yields

$$\alpha/p \approx Ae^{-Bp/E}\ ,\ 20\ \text{V}/\left(\text{cm-T}\right) < E/p < 30\ \text{V}/\left(\text{cm-T}\right) \tag{52}$$

$$A \approx 0.10264/\left(\text{cm-T}\right) \tag{53}$$

$$B \approx 141.46\ \text{V}/\left(\text{cm-T}\right) \tag{54}$$

This fit with A and B is used from $20\ \text{V}/\left(\text{cm-T}\right) < E/p < 30\ \text{V}/\left(\text{cm-T}\right)$. The form with A_1 and B_1 is used over the range $30\ \text{V}/\left(\text{cm-T}\right) < E/p < E_s/p$. Finally the form with A_2 and B_2 is used in the range $E_s/p < E/p < 600\ \text{V}/\left(\text{cm-T}\right)$. The intersection point is

$$E_s/p = \left(B_2 - B_1\right)/\ln\left(A_2/A_1\right) \approx 216\ \text{V}/\left(\text{cm-T}\right) \tag{55}$$

Figures 3 and 4, taken from [16], show a comparison between swarm data [16] and the three fit functions.

The agreement is reasonable.

3.1.3 krypton

Fit functions for the ionization coefficient of Krypton are [2]

$$\alpha/p \approx Ae^{-Bp/E}\ ,\ 100\ \text{V}/\left(\text{cm-T}\right) < E/p < 1000\ \text{V}/\left(\text{cm-T}\right) \tag{56}$$

$$A = 17/\left(\text{cm-T}\right) \tag{57}$$

$$B = 240\ \text{V}/\left(\text{cm-T}\right) \tag{58}$$

$$\alpha/p \approx Ce^{-D\sqrt{p/E}}\ ,\ E/p < 900\ \text{V}/\left(\text{cm-T}\right) \tag{59}$$

$$C = 35.7/\left(\text{cm-T}\right) \tag{60}$$

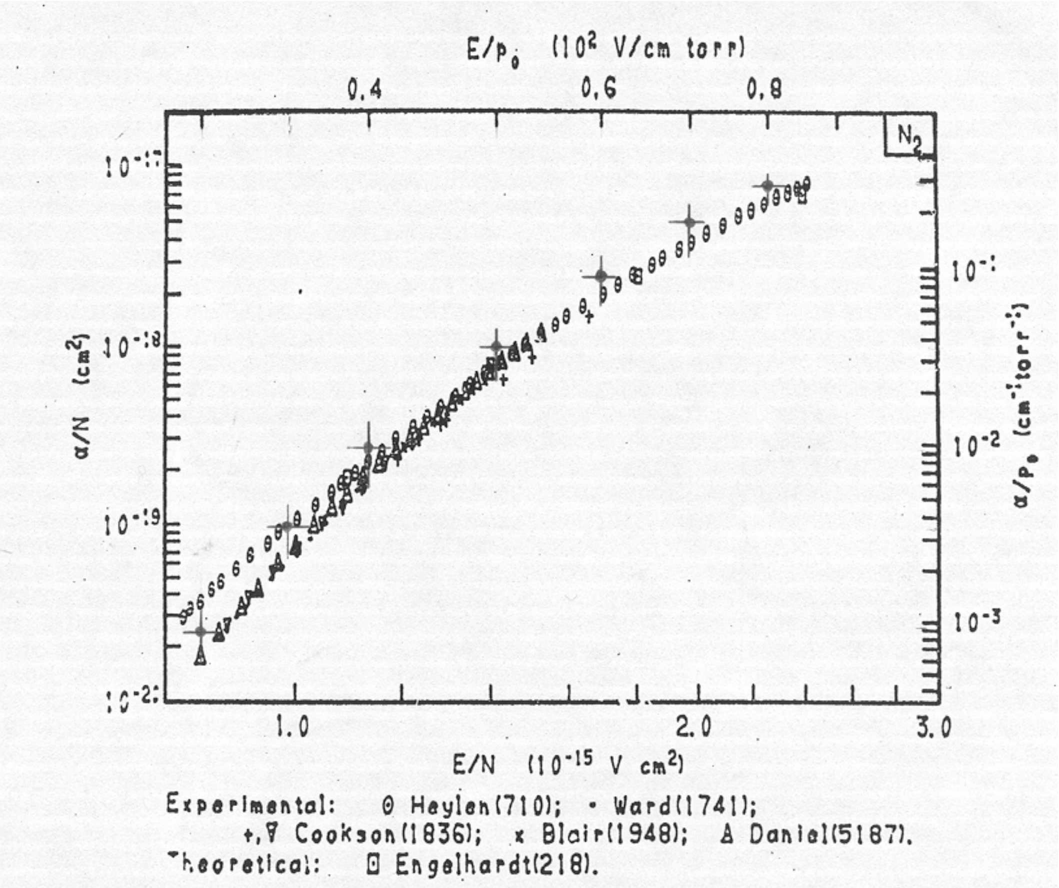

Figure 3. Comparison of experimental data (from "A Survey of Electron Swarm Data," J. Dutton [16]) with fit function predictions (large pluses with dot at center).

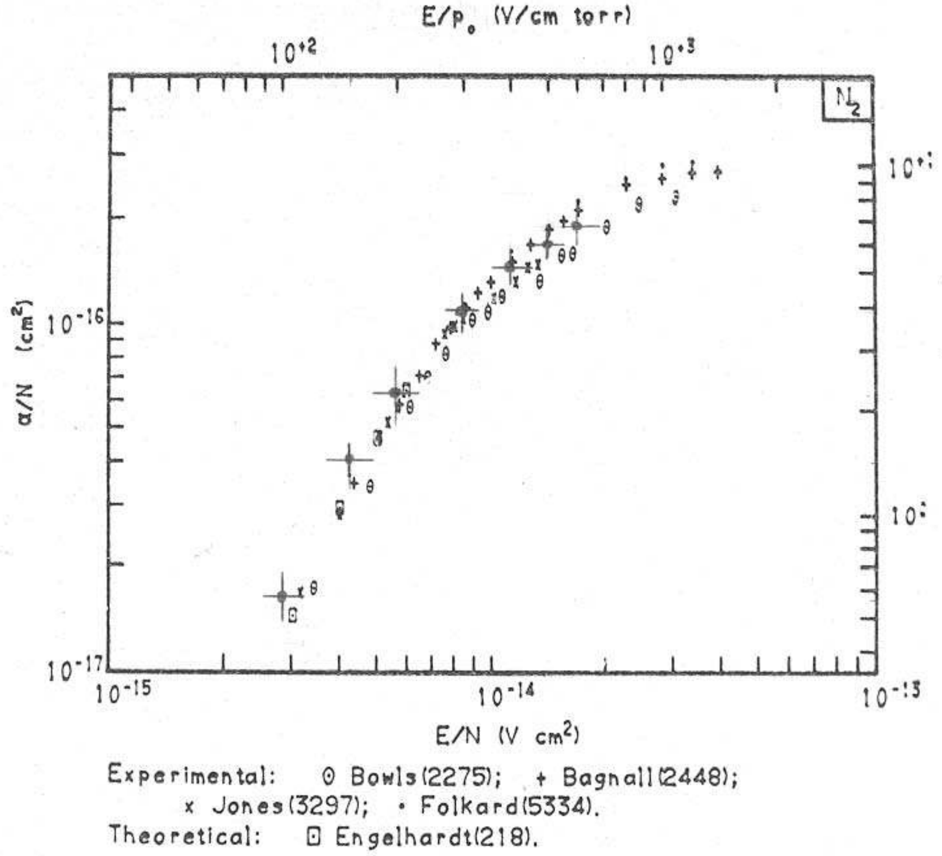

Figure 4. Comparison of experimental data (from "A Survey of Electron Swarm Data," J. Dutton [16]) with fit function predictions (large pluses with dot at center).

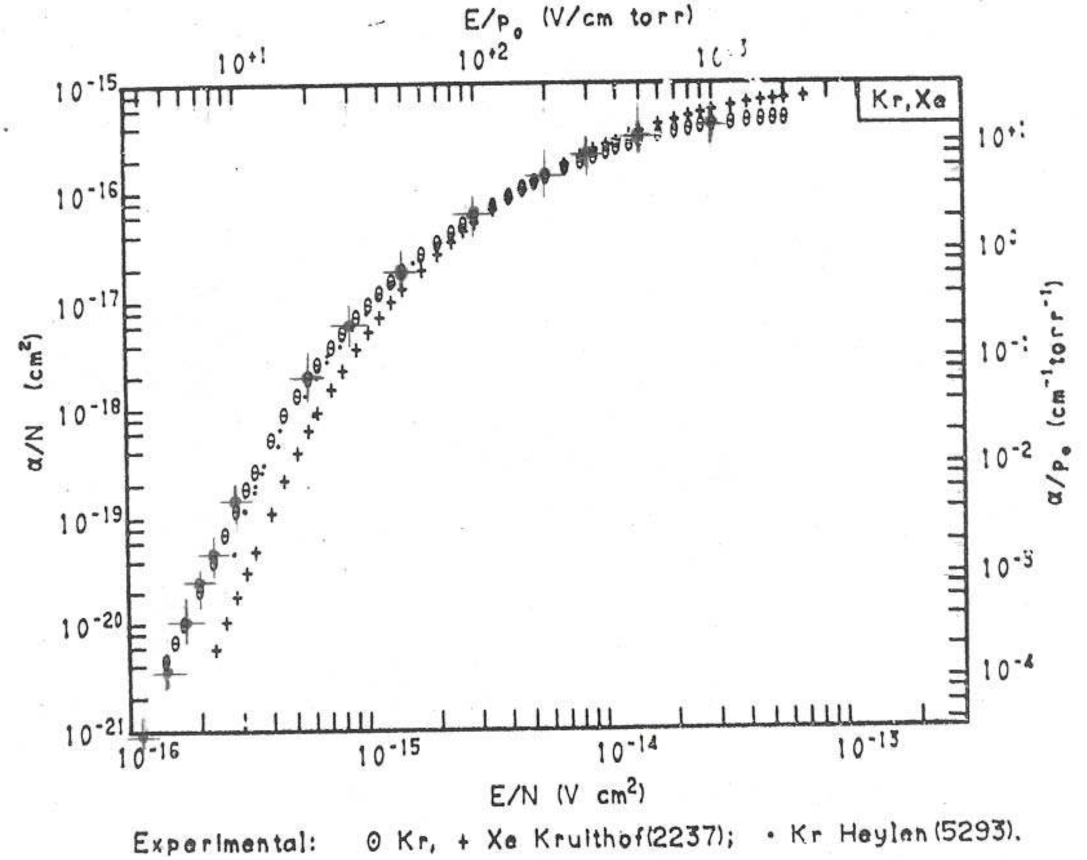

Figure 5. Comparison of experimental data (from "A Survey of Electron Swarm Data," J. Dutton [16]) with fit function predictions (large pluses with dot at center).

$$D = 28.2 \text{ V/ (cm-T)} \tag{61}$$

The intersection occurs at

$$E_s/p \approx 166V/ \text{(cm-T)} \tag{62}$$

Thus the second form with C and D is used for 0 V/ (cm-T) $< E/p < E_s/p$ and the first form with A and B for $E_s/p \leq E/p < 1000$ V/ (cm-T). Figure 5, taken from [16], shows a comparison between swarm data [16] and the two fit functions.

The agreement is reasonable.

3.2 Secondary Coefficient

The parameters in the right hand side of the breakdown condition are estimated in this section. We focus on photon impact emission and matching of this result to the streamer criterion. Breakdown data are used to estimate these parameters. In principle the parameter γ_p depends on details of the electrode

Element	φ (eV)	Element	φ (eV)	Element	φ (eV)
Cs	1.95	Al	4.28	C	4.7
K	2.30	Sn	4.28	Si	4.95
Na	2.36	Ta	4.30	Co	4.97
Ba	2.52	Ti	4.33	Ni	5.15
U	3.47	Cr	4.44	Au	5.10
Mn	4.08	Mo	4.49	Pd	5.40
Cd	4.22	Cu	4.51	Pt	5.63
Pb	4.25	W	4.55		
Ag	4.26	Fe	4.60		

Table 2.Work functions for various metals from [19].

(materials, roughness). However, because these details are often not specified in experimental breakdown data there is some justification in using the simplest possible model for the secondary emission that captures only dominant features of the secondary emission. It is also true that with γ_p appearing in a logarithm these variations are suppressed in the breakdown condition. Of course in cases where more detailed secondary emission data on the electrode are available they should be used.

We include first a short section on ion impact secondaries for inert gases where ion impact emission can play a dominant role.

3.2.1 ion impact secondaries in atomic gases

We first note that the emission is not strongly dependent on the ion kinetic energy (which is in often small compared to the ionization energy of these gases) [8]. A formula for the secondary ionization coefficient resulting from ion impact with the cathode in atomic gases is [2]

$$\gamma_i \approx (0.016/\mathrm{eV})\,(I - 2\varphi) \tag{63}$$

holds on clean surfaces to an accuracy of about 50%. The ionization energy is I and the work function is φ. A partial list of work functions is shown in Table 2 [19].

A partial list of ionization energies is shown in Table 3 [19].

An example is Krypton gas with Platinum electrodes

$$\gamma_i \approx 0.044$$

Iron electrodes give

$$\gamma_i \approx 0.077$$

Breakdown voltages in a uniform field with copper electrodes are given for atomic gases [7] and shown in Figure 6. A comparison with the breakdown condition using the preceding secondary emission is also given in the figure as the blue curves. Although there is some absolute error, the ordering of the curves is precisely as measured.

3.2.2 photon impact secondaries

The breakdown condition

Element	I (eV)
He	24.587
Ne	21.56
Ar	15.75
Kr	14.00
Xe	12.13

Table 3.Ionization energies for various inert gases from [19].

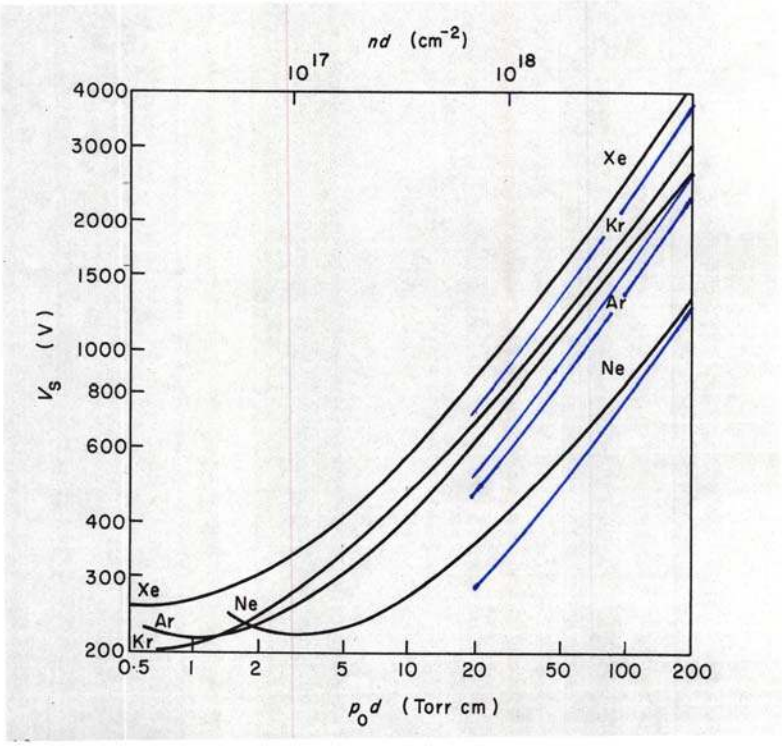

Figure 6. Comparison of breakdown predictions (analytical) in a uniform gap using only ion impact secondary emission (blue curves) with experiments (from "Electrical Breakdown of Gases," editors J. M. Meek and J. D. Craggs [7]). The cathode is copper. The gap is actually 1 cm in width and the pressure is being varied.

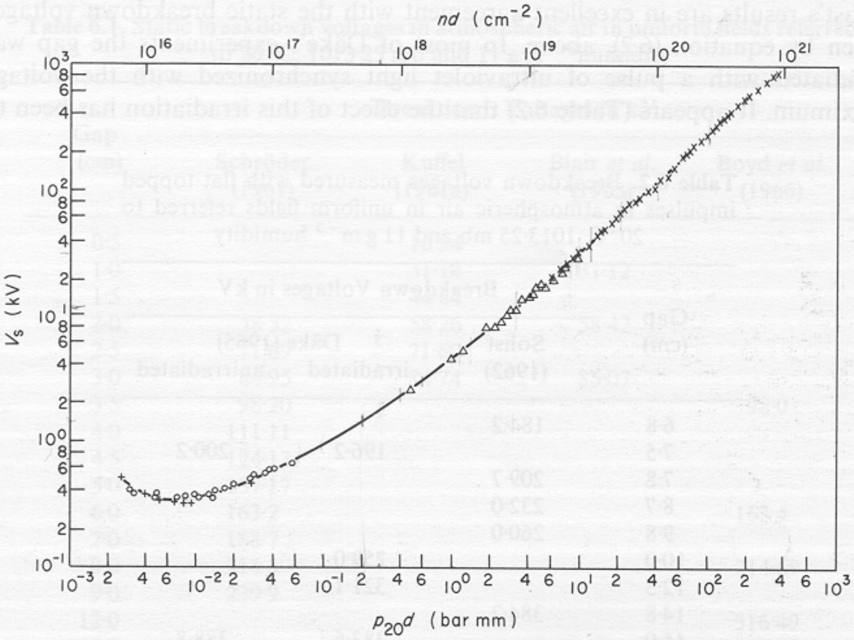

Figure 7. Experimental voltage breakdown of air (from "Electrical Breakdown of Gases," editors, J. M. Meek and J. D. Craggs [7]).

$$\alpha d = \ln\left(1/\gamma_p\right) + \mu d \tag{64}$$

is fit to uniform field breakdown data for air to determine the coefficients γ_p and μ, where photoionization is a candidate for cathode emission at pressures near atmospheric. Figure 7, taken from [7], shows an experimental voltage breakdown curve for air.

The preceding equation is fit to two values from this curve which lie in the region below streamer threshold but large enough that ion effects should be minimal. Reading the value off the curve for $d = 0.2$ cm as

$$V \approx 7.9 \text{ kV}$$

we find

$$E/p \approx 51.9 \text{ V}/\left(\text{cm-T}\right)$$

The fit function gives

$$\alpha/p \approx 0.0670/\left(\text{cm-T}\right)$$

Thus we have

$$0.0670/\left(\text{cm-T}\right)\ (760 \text{ T})\,(0.2 \text{ cm}) = \ln\left(1/\gamma_p\right) + \mu\,(0.2 \text{ cm})$$

Similarly for $d = 0.4$ cm we read the breakdown voltage as

$$V \approx 14.2 \text{ kV}$$

and find

$$E/p \approx 46.7 \text{ V}/\left(\text{cm-T}\right)$$

The fit function gives

$$\alpha/p \approx 0.0394/\left(\text{cm-T}\right)$$

Thus we have

$$0.0394/\left(\text{cm-T}\right)\ (760\text{ T})\,(0.4\text{ cm}) = \ln\left(1/\gamma_p\right) + \mu\,(0.4\text{ cm})$$

Subtracting the two equations gives

$$\mu \approx 9/\text{cm} \tag{65}$$

and thus

$$\ln\left(1/\gamma_p\right) \approx 8.4 \tag{66}$$

It must be noted here that the value of μ and of $\ln\left(1/\gamma_p\right)$ are highly variable. For example, they are dependent on errors in the α/p fit function as well as errors in breakdown voltages. Nevertheless, the value for $\ln\left(1/\gamma_p\right)$ is reasonable. This value corresponds to $\gamma_p \approx 2.2 \times 10^{-4}$ which is in the ballpark of what was expected [2]. Figure 8, taken from [8], shows values of the secondary emission for various electrode surfaces. Noting that the work functions of the heavier metals are in the $4 - 6$ eV range [8], (and presuming that photons having energies just above this range would be impacting the cathode) the value obtained for γ_p seems reasonable.

The absorption coefficient is expected to be proportional to pressure so that

$$\frac{\mu}{p} \approx 0.012/\left(\text{cm-T}\right)$$

Thus we can write the breakdown condition as

$$\frac{\alpha}{p}\left(\frac{E}{p}\right)pd = \frac{\alpha}{p}\left(\frac{V}{pd}\right)pd = \ln\left(1 + 1/\gamma\right) \approx \ln\left(1/\gamma_p\right) + \frac{\mu}{p}\,pd$$

3.2.3 streamer matching distance

Equating the streamer threshold condition and the Townsend condition for air at 760 T gives

$$\ln\left(1/\gamma_p\right) + \mu d_c \approx 17.7 + \ln\left(d_c/1\text{ cm}\right) \tag{67}$$

Starting with $d_c = 1$ cm, iteration yields

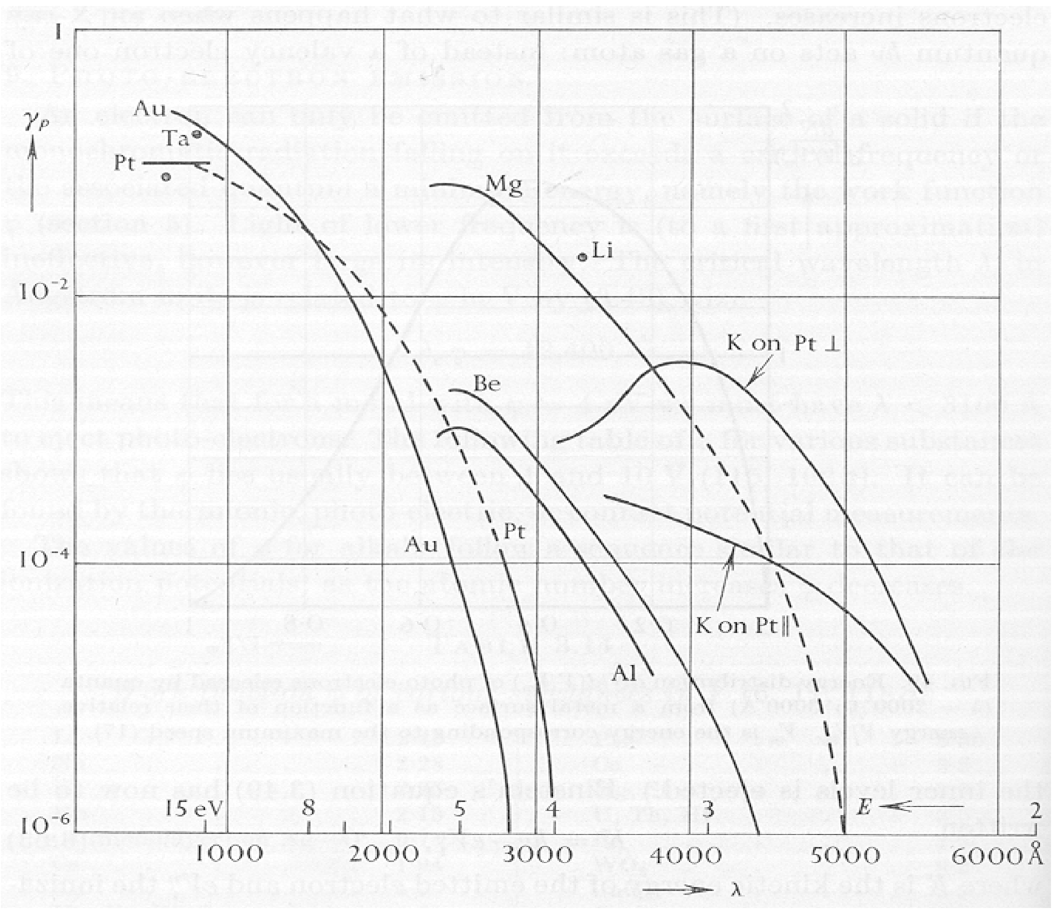

Figure 8. Photoemission coefficient for various surface materials (from "Ionized Gases," A. von Engel [8]).

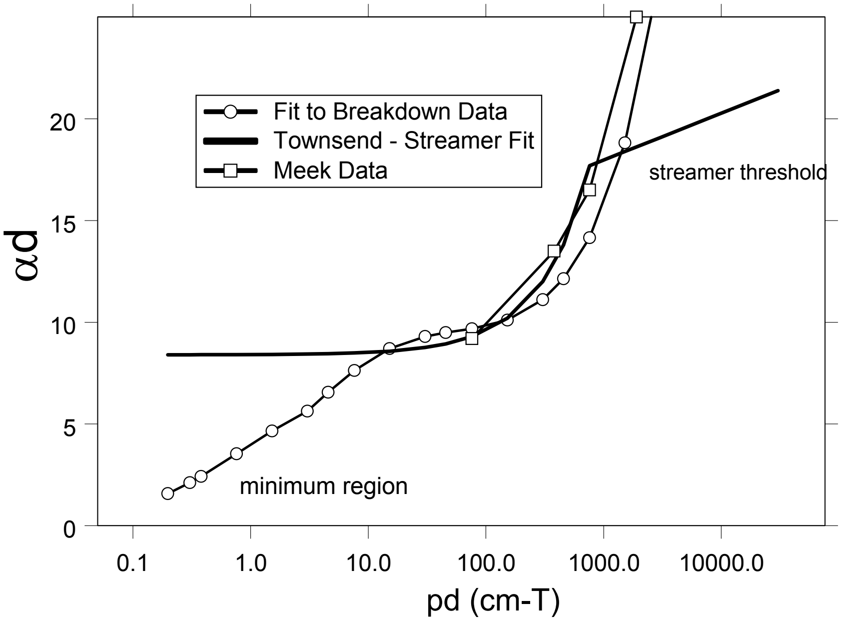

Figure 9. Comparison of breakdown condition left hand side values from breakdown voltage data with Townsend - streamer threshold fit.

$$d_c \approx 1.0374 \text{ cm} \tag{68}$$

Figure 9 shows a comparison of the value of the breakdown condition determined from a fit to experimental breakdown data [12]

$$V \approx 6.72 \text{ kV}\sqrt{pd/\left(760 \text{ cm-T}\right)} + 24.36 \text{ kV } pd/\left(760 \text{ cm-T}\right) \tag{69}$$

and the α/p fit (using A, B and A_1, B_1) for air. Note that the voltage breakdown fit (69) is actually consistent with a parabolic formula [2] for the ionization coefficient

$$\alpha/p \approx C_2 \left(E/p - D_2\right)^2 \ , \ 44 \text{ V}/\left(\text{cm-T}\right) \leq E/p \leq 176 \text{ V}/\left(\text{cm-T}\right) \tag{70}$$

$$C_2 = 1.17 \times 10^{-4} \left(\text{cm-T}\right)/\text{V}^2$$

$$D_2 = 32.2 \text{ V}/\left(\text{cm-T}\right)$$

This description of the ionization coefficient is also frequently used in the midrange and is shown as the blue dots in Figure 2; it agrees reasonably well with the exponential fits discussed previously.

Also shown is data from Meek [6], and the preceding Townsend - streamer threshold fit to the right hand side of the breakdown condition.

Part of the reason for the discrepancy on the left end of the plot is that the values of the experimental data fit (69) near the minimum of the Paschen breakdown curve are not accurate [12]. The Townsend - streamer fit seems to have captured a transition in the curve near 100 cm-T. The streamer threshold condition appears to underestimate the data, however, there is some question about the accuracy of the α/p fit in this area. Furthermore, other data on α in this region [12] is smaller than those used here [16] as discussed above.

We have not discussed nitrogen in this subsection. As a rough approximation we can use the air secondary coefficient.

4 CANONICAL PROBLEMS

This section gives the analytic solutions to several canonical problems used for verification. These problems were chosen so that: 1) analytical solutions existed, 2) to exercise various features of the numerical code of interest in stronglink switch geometries, and 3) to coincide with problems for which experimental validation data exists.

4.1 Plane - Plane Problem

The uniform field problem is simple. A voltage V between the two planes separated by d generates a field

$$E = V/d \tag{71}$$

Thus the uniform field breakdown conditions determine α/p, E/p, and V.

4.1.1 ionization

The breakdown condition in this case is the simple uniform one

$$\frac{\alpha}{p}\left(\frac{E}{p}\right) pd = F \tag{72}$$

$$F = \ln\left(1 + 1/\gamma\right) \approx \ln\left(1/\gamma_p\right) + \frac{\mu}{p} pd\,,\; d \le d_c$$

$$= 17.7 + \ln d\,,\; d > d_c \tag{73}$$

from which V is found.

4.2 Coaxial Problem

The field in this case is simple but nonuniform. Given a voltage V between the center conductor of radius a and the outer conductor of radius b, we have

$$E = \frac{V}{\rho \ln\left(b/a\right)} \tag{74}$$

where ρ is the radial distance. The gap d is

$$d = b - a \tag{75}$$

4.2.1 ionization integration

Taking

$$\alpha/p = Ae^{-Bp/E}$$

we have

$$\int_C \alpha ds = pA \int_{\rho_1}^{\rho_2} e^{-\rho \ln(b/a)Bp/V} d\rho = \frac{pA}{\ln(b/a)\,Bp/V}\left[e^{-\rho_1 \ln(b/a)Bp/V} - e^{-\rho_2 \ln(b/a)Bp/V}\right] \tag{76}$$

where this formula can be applied in several intervals with different coefficients if necessary. Note that the fit formula for Krypton (59) can also be integrated analytically.

4.2.2 minimum field criterion

Suppose we take the minimum field at $\rho = b$ to be

$$E_{\min} = 4.7 \text{ kV/cm}$$

Then the proposed sparking voltage is

$$V = E_{\min} b \ln(b/a)$$

4.3 Right Corner - Plane Problem

The problem is shown in Figure 22. The gap is w and the complex variable is $z = x + iy$. The conformal mapping solution is found as [17]

$$\frac{dz}{dz_1} = C_1 z_1^{\frac{3\pi/2}{\pi}-1}(z-1)^{\frac{0}{\pi}-1} = C_1\sqrt{z_1}/(z_1-1)$$

Integration gives (letting $\sqrt{z_1} = u$)

$$z = C_1 \int \sqrt{z_1}\frac{dz_1}{z_1-1} = C_1 \int \frac{2u^2du}{u^2-1} = C_1 \int \left(2 + \frac{1}{u-1} - \frac{1}{u+1}\right) du$$

$$= C_1\left[2u + \ln(u-1) - \ln(u+1)\right] + C_2 = C_1\left[2u + \ln\left(\frac{u-1}{u+1}\right)\right] + C_2$$

$$= C_1\left[2\sqrt{z_1} + \ln\left(\frac{\sqrt{z_1}-1}{\sqrt{z_1}+1}\right)\right] + C_2$$

Now setting $z = iw$ and $z_1 = 0$ gives

$$iw = C_1\left(i\pi\right) + C_2$$

From the original differential form, near $z_1 = 1$

$$dz \sim C_1 dz_1 / \left(z_1 - 1\right)$$

Thus letting $z_1 = 1 + \varepsilon e^{i\varphi}$ gives

$$-iw = C_1 i \; d\varphi|_{\pi}^{0} = -iC_1\pi$$

or

$$C_1 = w/\pi$$

and

$$C_2 = 0$$

Thus the conformal transformation is

$$z = \frac{w}{\pi}\left[2\sqrt{z_1} + \ln\left(\frac{\sqrt{z_1} - 1}{\sqrt{z_1} + 1}\right)\right] \tag{77}$$

If we take the upper conductor to have potential V and the plane conductor to have potential 0 we can write

$$\phi = \mathrm{Im}\left(W\right) \tag{78}$$

where the complex potential is

$$W = \frac{V}{\pi}\ln\left(z_1 - 1\right) \tag{79}$$

The electric field is found as

$$\underline{E} = -\nabla\phi \tag{80}$$

or

$$E_x = -\,\mathrm{Im}\left(\frac{dW}{dz}\right) = -\,\mathrm{Im}\left(\frac{dW}{dz_1}\frac{dz_1}{dz}\right) \tag{81}$$

$$E_y = -\,\mathrm{Re}\left(\frac{dW}{dz}\right) = -\,\mathrm{Re}\left(\frac{dW}{dz_1}\frac{dz_1}{dz}\right) \tag{82}$$

$$\frac{dW}{dz_1} = \frac{V/\pi}{z_1 - 1} \tag{83}$$

$$\frac{dz_1}{dz} = 1/\frac{dz}{dz_1} = \frac{\pi\left(z_1 - 1\right)}{w\sqrt{z_1}} \tag{84}$$

$$\frac{dW}{dz} = \frac{V/w}{\sqrt{z_1}} \tag{85}$$

The magnitude is thus

$$E = \sqrt{E_x^2 + E_y^2} = \frac{V}{w\sqrt{|z_1|}} \tag{86}$$

4.3.1 ionization integration

Field lines follow the semi-circular paths about unity or $z_1 = 1 + R_1 e^{i\varphi}$, $0 < \varphi < \pi$. Thus we write

$$\int_C \alpha\left(E\right) ds = \int_C \alpha\left(E\right)|dz| = \int_C \alpha\left(E\right)\left|\frac{dz}{dz_1}\right||dz_1| = \int_C \alpha\left(\frac{V}{w\sqrt{|z_1|}}\right)\frac{w\sqrt{|z_1|}}{\pi\left|z_1 - 1\right|}R_1\left|d\varphi\right|$$

$$= \int_0^{\pi} \alpha\left(\frac{V}{w\sqrt{|z_1|}}\right)\frac{w\sqrt{|z_1|}}{\pi}d\varphi \tag{87}$$

Using

$$|z_1| = \sqrt{\left(1 + R_1\cos\varphi\right)^2 + R_1^2\sin^2\varphi} = \sqrt{1 + R_1^2 + 2R_1\cos\varphi} \tag{88}$$

gives

$$\int_C \alpha\left(E\right) ds = \frac{w}{\pi}\int_0^{\pi} \alpha\left[\frac{V/w}{\left(1 + R_1^2 + 2R_1\cos\varphi\right)^{1/4}}\right]\left(1 + R_1^2 + 2R_1\cos\varphi\right)^{1/4} d\varphi \tag{89}$$

The position x from the corner in z space on the top surface is

$$x = \frac{w}{\pi}\left[2\sqrt{1 - R_1} + \ln\left(\frac{1 - \sqrt{1 - R_1}}{1 + \sqrt{1 - R_1}}\right)\right] \tag{90}$$

The two cases of interest are integration along a field line from the corner $x = 0$ with $R_1 = 1$

$$\int_{C_c} \alpha\left(E\right) ds = 2\frac{w}{\pi}\int_0^{\pi/2} \alpha\left[\frac{V/w}{\sqrt{2\cos\varphi}}\right]\sqrt{2\cos\varphi}d\varphi \tag{91}$$

and integration over the parallel plate region $x \to -\infty$ with $R_1 \to 0$

$$\int_{C_p} \alpha\left(E\right) ds = w\alpha\left(V/w\right) \tag{92}$$

Using the interpolation function

$$\alpha/p \approx Ae^{-Bp/E}$$

we have

$$\int_{C_c} \alpha\left(E\right) ds = 2\frac{w}{\pi}pA\int_0^{\pi/2} \exp\left[-\frac{wp}{V}\sqrt{2\cos\varphi}\right]\sqrt{2\cos\varphi}d\varphi \tag{93}$$

Letting

$$u = \sqrt{\cos\varphi}$$

$$udu = -\frac{1}{2}\sin\varphi d\varphi = -\frac{1}{2}\sqrt{1-u^4}d\varphi$$

or

$$\int_{C_c} \alpha\left(E\right) ds = 2^{5/2}\frac{w}{\pi}pA\int_0^{1} \exp\left[-\frac{wp}{V}u\sqrt{2}\right]\frac{u^2du}{\sqrt{1-u^4}} \tag{94}$$

Using the α/p fit functions for air we find that

$$\int_{C_c} \alpha\left(E\right) ds = \int_{C_p} \alpha\left(E\right) ds \tag{95}$$

when

$$V/\left(wp\right) \approx 78.68 \text{ V}/\left(\text{cm-T}\right) \tag{96}$$

$$\frac{1}{w}\int_{C} \alpha\left(E\right) ds \approx 257/\text{cm}$$

Below this field value (96) the corner integral is larger than the plane field integral. Above this value the plane field integral is larger.

4.4 Arbitrary Angle Corner - Plane Problem

The case where the external opening angle is $2\varphi_0$ (instead of $3\pi/2$) has conformal mapping transformation [17]

$$\frac{dz}{dz_1} = C_1 z_1^{\frac{2\varphi_0}{\pi}-1}\left(z-1\right)^{\frac{0}{\pi}-1} = C_1 z_1^{2\varphi_0/\pi-1}/\left(z_1-1\right)$$

$$= C_1 z_1^{2\varphi_0/\pi-1}/\left(z_1-1\right)$$

$$z = C_1\int\frac{z_1^{2\varphi_0/\pi-1}}{z_1-1}dz_1 + C_2$$

Approximating near unity again gives

$$C_1 = w/\pi$$

$$z = \frac{w}{\pi} \int_0^{z_1} \frac{z_1^{2\varphi_0/\pi - 1}}{z_1 - 1} dz_1 \tag{97}$$

The solution is the same as the preceding section with

$$\frac{dW}{dz_1} = \frac{V/\pi}{z_1 - 1}$$

$$\frac{dz_1}{dz} = 1 \Big/ \frac{dz}{dz_1} = \frac{\pi \left(z_1 - 1\right)}{w z_1^{2\varphi_0/\pi - 1}} \tag{98}$$

$$\frac{dW}{dz} = \frac{V/w}{z_1^{2\varphi_0/\pi - 1}} \tag{99}$$

The magnitude is thus

$$E = \sqrt{E_x^2 + E_y^2} = \frac{V}{w \left|z_1\right|^{2\varphi_0/\pi - 1}} \tag{100}$$

4.4.1 ionization integration

Field lines follow the semi-circular paths about unity or $z_1 = 1 + R_1 e^{i\varphi}$, $0 < \varphi < \pi$. Thus we write

$$\int_C \alpha\left(E\right) ds = \int_C \alpha\left(E\right) \left|dz\right| = \int_C \alpha\left(E\right) \left|\frac{dz}{dz_1}\right| \left|dz_1\right| = \int_C \alpha \left(\frac{V}{w \left|z_1\right|^{2\varphi_0/\pi - 1}}\right) \frac{w \left|z_1\right|^{2\varphi_0/\pi - 1}}{\pi \left|z_1 - 1\right|} R_1 \left|d\varphi\right|$$

$$= \int_0^{\pi} \alpha \left(\frac{V}{w \left|z_1\right|^{2\varphi_0/\pi - 1}}\right) \frac{w \left|z_1\right|^{2\varphi_0/\pi - 1}}{\pi} d\varphi \tag{101}$$

Using

$$\left|z_1\right| = \sqrt{\left(1 + R_1 \cos\varphi\right)^2 + R_1^2 \sin^2\varphi} = \sqrt{1 + R_1^2 + 2R_1 \cos\varphi}$$

gives

$$\int_C \alpha\left(E\right) ds = \frac{w}{\pi} \int_0^{\pi} \alpha \left[\frac{V/w}{\left(1 + R_1^2 + 2R_1 \cos\varphi\right)^{\varphi_0/\pi - 1/2}}\right] \left(1 + R_1^2 + 2R_1 \cos\varphi\right)^{\varphi_0/\pi - 1/2} d\varphi \tag{102}$$

The position x from the corner in z space on the top surface is

$$x = \frac{w}{\pi} \int_0^{1 - R_1} \frac{z_1^{2\varphi_0/\pi - 1}}{z_1 - 1} dz_1 \tag{103}$$

The two cases of interest are integration along a field line from the corner $x = 0$ with $R_1 = 1$

$$\int_{C_c} \alpha(E)\, ds = 2\frac{w}{\pi}\int_0^{\pi/2} \alpha\left[\frac{V/w}{(2\cos\varphi)^{2\varphi_0/\pi-1}}\right](2\cos\varphi)^{2\varphi_0/\pi-1}\, d\varphi \tag{104}$$

and integration over the parallel plate region $x \to -\infty$ with $R_1 \to 0$

$$\int_{C_p} \alpha(E)\, ds = w\alpha(V/w) \tag{105}$$

Using the interpolation function

$$\alpha/p \approx Ae^{-Bp/E}$$

we have

$$\int_{C_c} \alpha(E)\, ds = 2\frac{w}{\pi}pA\int_0^{\pi/2} \exp\left[-\frac{wp}{V}(2\cos\varphi)^{2\varphi_0/\pi-1}\right](2\cos\varphi)^{2\varphi_0/\pi-1}\, d\varphi \tag{106}$$

4.5 Wire - Wire Problem

The two cylinders are separated by a distance (center-to-center separation) $2h$ and each have radius a. The potential is [17]

$$\phi = -\frac{q}{2\pi\varepsilon_0}\ln\sqrt{\frac{x^2+(y-h_e)^2}{x^2+(y+h_e)^2}} \tag{107}$$

where the effective height is

$$h_e = \sqrt{h^2-a^2} \tag{108}$$

The charge per unit length on the cylinders $\pm q$ is evaluated in terms of the voltage by setting $\phi = V/2$ and $x = 0$, $y = h - a$

$$V/2 = \frac{q}{2\pi\varepsilon_0}\ln\left(\frac{\sqrt{h+a}+\sqrt{h-a}}{\sqrt{h+a}-\sqrt{h-a}}\right) = \frac{q}{2\pi\varepsilon_0}\ln\left(\frac{h+\sqrt{h^2-a^2}}{a}\right) \tag{109}$$

or

$$c = q/V = \frac{\pi\varepsilon_0}{\ln\left[(h+h_e)/a\right]} \tag{110}$$

The y directed electric field is

$$E_y = -\frac{\partial\phi}{\partial y} = \frac{q}{2\pi\varepsilon_0}\left[\frac{y-h_e}{x^2+(y-h_e)^2} - \frac{y+h_e}{x^2+(y+h_e)^2}\right] \tag{111}$$

It is useful to determine the maximum, average, and minimum fields in the problem (the experimental data is often reported in terms of maximum field). The electric field on $x = 0$ is

$$E_y\left(0,y\right) = -\frac{qh_e}{\pi\varepsilon_0\left(h_e^2-y^2\right)} = -\frac{Vh_e/\ln\left[\left(h+h_e\right)/a\right]}{\left(h_e^2-y^2\right)} \tag{112}$$

The maximum field is related to the voltage by

$$E_{\max} = \frac{Vh_e/\ln\left[\left(h+h_e\right)/a\right]}{2\left(h-a\right)a} \tag{113}$$

or

$$\left(a/h_e\right)\ln\left[\left(h+h_e\right)/a\right]E_{\max} = \frac{V}{2\left(h-a\right)} = \langle E\rangle \tag{114}$$

where $\langle E\rangle$ is the average field level. For large spacing $h_e \to h$

$$\frac{2a}{(2h)}\ln\left(2h/a\right)E_{\max} \sim \frac{V}{2\left(h-a\right)} = \langle E\rangle$$

The ratio of maximum to minimum field is

$$E_{\max}/E_{\min} = \frac{h+a}{2a} \tag{115}$$

For large h

$$E_{\max}/E_{\min} \sim \frac{(2h)}{4a} \tag{116}$$

4.5.1 minimum field

The mimimum field is

$$E_{\min} = \frac{q}{\pi\varepsilon_0 h_e} = \frac{V}{h_e\ln\left[\left(h+h_e\right)/a\right]} = \frac{V}{\sqrt{h^2-a^2}\ln\left[\left(h+\sqrt{h^2-a^2}\right)/a\right]} \tag{117}$$

Letting $2g = 2h-2a$ we can write

$$V = \sqrt{h^2-a^2}\ln\left[\left(h+\sqrt{h^2-a^2}\right)/a\right]E_{\min} = \sqrt{\left(g+2a\right)g}\ln\left[\left(g+a+\sqrt{\left(g+2a\right)g}\right)/a\right]E_{\min}$$

$$\sim h\ln\left(2h/a\right)E_{\min}\,,\; h >> a \tag{118}$$

4.5.2 ionization integration

We find the integral of the ionization coefficient

$$\int_{y_1}^{y_2}\alpha dy = p\int_{y_1}^{y_2}A\exp\left[-\frac{Bp\left(h_e^2-y^2\right)}{Vh_e/\ln\left[\left(h+h_e\right)/a\right]}\right]dy = pA\exp\left[-\frac{Bph_e^2}{Vh_e/\ln\left[\left(h+h_e\right)/a\right]}\right]$$

$$\left(\int_0^{y_2} - \int_0^{y_1}\right) \exp\left[\frac{Bpy^2}{Vh_e/\ln\left[(h+h_e)/a\right]}\right] dy$$

$$= pAe^{-\kappa^2 h_e^2}\left[\mathrm{erf}\left(\kappa y_2\right) - \mathrm{erf}\left(\kappa y_1\right)\right]/\kappa \tag{119}$$

where

$$\kappa = \sqrt{\frac{Bp\ln\left[(h+h_e)/a\right]}{Vh_e}} \tag{120}$$

4.6 Sphere - Sphere Problem

The spheres have center-to-center spacing $2h$ and each have radius a. The potential is found by a series of images. To establish a voltage between the spheres we place charges $\pm Q_0$ at $z = \pm h$ where

$$V/2 = \frac{Q_0}{4\pi\varepsilon_0 a}$$

Image charges $\pm Q_n$ are then placed at $\pm h_n$ to make the potential induced on each sphere from the charges on the other sphere vanish. We take [17]

$$h_n = h - d_n \tag{121}$$

$$d_n = a^2/\left(2h - d_{n-1}\right) \tag{122}$$

$$Q_n = Q_{n-1}d_n/a = Q_{n-1}a/\left(2h - d_{n-1}\right) \tag{123}$$

$$Q_0 = 2\pi\varepsilon_0 aV \tag{124}$$

$$h_0 = h \tag{125}$$

$$d_0 = 0 \tag{126}$$

The potential is

$$\phi = \sum_{n=0}^{\infty}\frac{Q_n}{4\pi\varepsilon_0}\left[\frac{1}{\sqrt{\rho^2 + \left(z-h_n\right)^2}} - \frac{1}{\sqrt{\rho^2 + \left(z+h_n\right)^2}}\right] \tag{127}$$

The z directed electric field is

$$E_z = -\frac{\partial\phi}{\partial z} = \sum_{n=0}^{\infty} \frac{Q_n}{4\pi\varepsilon_0} \left[\frac{z - h_n}{\left\{\rho^2 + (z - h_n)^2\right\}^{3/2}} - \frac{z + h_n}{\left\{\rho^2 + (z + h_n)^2\right\}^{3/2}} \right] \tag{128}$$

The total charge on the sphere is

$$Q = \sum_{n=0}^{\infty} Q_n \tag{129}$$

The capacitance between the two spheres is given by

$$C = Q/V = 2\pi\varepsilon_0 \pi a \sinh(\alpha/2) \sum_{n=1}^{\infty} \left[\operatorname{csch}(n - 1/2)\,\alpha + \operatorname{csch}(n\alpha)\right] \tag{130}$$

$$\cosh\alpha = \frac{2h^2 - a^2}{a^2} \tag{131}$$

4.6.1 ionization integration

On the line $\rho = 0$ we have

$$E_z(0, z) = -\sum_{n=0}^{\infty} \frac{Q_n}{4\pi\varepsilon_0} \left[\frac{1}{(h_n - z)^2} + \frac{1}{(h_n + z)^2} \right], \ |z| \le h - a \tag{132}$$

This is used to determine the ionization coefficient along the path between spheres.

4.6.2 minimum field

The minimum field is

$$E_{\min} = \sum_{n=0}^{\infty} \frac{Q_n}{2\pi\varepsilon_0 h_n^2} \tag{133}$$

4.7 Rod-Plane Problem

The rod is treated as a cylinder with line charge density $q(z)$. The potential is then

$$\phi(\rho, z) = \frac{1}{4\pi\varepsilon_0} \int_h^R \left[\frac{1}{\sqrt{\rho^2 + (z - z')^2}} - \frac{1}{\sqrt{\rho^2 + (z + z')^2}} \right] q(z')\,dz' \tag{134}$$

Enforcing the equipotential boundary condition gives

$$V = \frac{1}{4\pi\varepsilon_0} \int_h^R \left[\frac{1}{\sqrt{a^2 + (z - z')^2}} - \frac{1}{\sqrt{a^2 + (z + z')^2}} \right] q(z')\,dz'$$

Following the usual iteration technique

$$\int_h^R \left[\frac{1}{\sqrt{a^2 + (z - z')^2}} - \frac{1}{\sqrt{a^2 + (z + z')^2}} \right] dz' = \int_{h-z}^{R-z} \frac{du}{\sqrt{a^2 + u^2}} - \int_{h+z}^{R+z} \frac{du}{\sqrt{a^2 + u^2}}$$

$$= \mathrm{Arcsinh}\left\{(R - z)/a\right\} - \mathrm{Arcsinh}\left\{(h - z)/a\right\}$$

$$-\mathrm{Arcsinh}\left\{(R + z)/a\right\} + \mathrm{Arcsinh}\left\{(h + z)/a\right\}$$

$$= \ln\left[\left\{(R - z)/a\right\} + \sqrt{1 + \left\{(R - z)/a\right\}^2}\right] - \ln\left[\left\{(h - z)/a\right\} + \sqrt{1 + \left\{(h - z)/a\right\}^2}\right]$$

$$- \ln\left[\left\{(R + z)/a\right\} + \sqrt{1 + \left\{(R + z)/a\right\}^2}\right] + \ln\left[\left\{(h + z)/a\right\} + \sqrt{1 + \left\{(h + z)/a\right\}^2}\right]$$

$$\sim \ln\left\{(R - z)/(R + z)\right\} + \ln\left\{(h + z)/(h - z)\right\} \ , \ h > z$$

$$\ln\left\{(R - z)/(R + z)\right\} + \ln\left\{(z + h)(z - h)/h^2\right\} + 2\ln(2h/a) \ , \ h < z$$

Thus we write

$$V \sim \frac{1}{4\pi\varepsilon_0} \int_h^R \left[\frac{1}{|z - z'|} - \frac{1}{z + z'} \right] \left\{q(z') - q(z)\right\} dz'$$

$$+\frac{q(z)}{4\pi\varepsilon_0} \left[\ln\left\{(R - z)/(R + z)\right\} + \ln\left\{(z + h)(z - h)/h^2\right\} + \Omega\right]$$

$$\sim \frac{\Omega}{4\pi\varepsilon_0} q(z)$$

where

$$\Omega = 2\ln(2h/a) \tag{135}$$

Thus the zero order solution for the charge per unit length is

$$q(z) \sim q_0 = \frac{4\pi\varepsilon_0}{\Omega} V \tag{136}$$

4.7.1 minimum field

Near the ground plane (near the axis of the rod) we have

$$\phi(\rho,z)\sim\frac{q_0}{4\pi\varepsilon_0}\int_h^R\left[\frac{1}{\sqrt{\rho^2+(z-z')^2}}-\frac{1}{\sqrt{\rho^2+(z+z')^2}}\right]dz'$$

$$\sim\frac{q_0}{4\pi\varepsilon_0}\left[\ln\left\{(R-z)/(R+z)\right\}+\ln\left\{(h+z)/(h-z)\right\}\right]$$

The electric field is thus

$$E_z(\rho,z)\sim\frac{q_0}{4\pi\varepsilon_0}\left[\frac{1}{R-z}+\frac{1}{R+z}-\frac{1}{h+z}-\frac{1}{h-z}\right]$$

$$\sim-\frac{q_0}{4\pi\varepsilon_0}\left[\frac{1}{h+z}+\frac{1}{h-z}\right]$$

On the plane therefore

$$E_z(\rho,0)\sim-\frac{q_0}{2\pi\varepsilon_0 h}=-\frac{2}{\Omega}V/h$$

or

$$E_{\min}\sim\frac{2}{\Omega}V/h=\frac{V/h}{\ln(2h/a)}$$

Noting that $h=d+a$ gives

$$E_{\min}\sim\frac{V/(d+a)}{\ln(2(d+a)/a)} \tag{137}$$

4.7.2 ionization integration

To determine an approximation to the field which is valid from the tip down to the ground plane we must include the charge concentrations near the end of the rod. A simple assumption would be

$$q(z')=q_0+Q_0\delta(h-z') \tag{138}$$

The potential is

$$4\pi\varepsilon_0\phi(\rho,z)=\int_h^R\left[\frac{1}{\sqrt{\rho^2+(z-z')^2}}-\frac{1}{\sqrt{\rho^2+(z+z')^2}}\right]q(z')\,dz'$$

$$=q_0\ln\left[\left\{(R-z)/\rho\right\}+\sqrt{1+\left\{(R-z)/\rho\right\}^2}\right]-q_0\ln\left[\left\{(h-z)/\rho\right\}+\sqrt{1+\left\{(h-z)/\rho\right\}^2}\right]$$

$$-q_0\ln\left[\left\{(R+z)/\rho\right\}+\sqrt{1+\left\{(R+z)/\rho\right\}^2}\right]+q_0\ln\left[\left\{(h+z)/\rho\right\}+\sqrt{1+\left\{(h+z)/\rho\right\}^2}\right]$$

$$+Q_0\left[\frac{1}{\sqrt{\rho^2+(h-z)^2}}-\frac{1}{\sqrt{\rho^2+(h+z)^2}}\right] \tag{139}$$

If we retain all terms but let $R \to \infty$ and let $\rho \to 0$ in the image terms

$$4\pi\varepsilon_0\phi(\rho,z)\sim$$

$$=q_0\left[\ln\{2(h+z)\}-\ln\left\{(h-z)+\sqrt{\rho^2+(h-z)^2}\right\}\right]$$

$$+Q_0\left[\frac{1}{\sqrt{\rho^2+(h-z)^2}}-\frac{1}{h+z}\right] \tag{140}$$

The match point equation on the cylinder we take to be an average over the cylinder out to distance R_0

$$4\pi\varepsilon_0V\sim q_0\frac{1}{ph}\int_h^{h+R_0}\left[\ln\{2(h+z)\}-2\ln a+\ln\left\{(z-h)+\sqrt{a^2+(z-h)^2}\right\}\right]dz$$

$$+Q_0\frac{1}{R_0}\int_h^{h+R_0}\left[\frac{1}{\sqrt{a^2+(z-h)^2}}-\frac{1}{h+z}\right]dz$$

$$\sim q_0\frac{1}{R_0}\int_0^{R_0}\left[\ln\{2(2h+u)\}-2\ln a+\ln\left(u+\sqrt{a^2+u^2}\right)\right]du+Q_0\frac{1}{R_0}\int_0^{R_0}\left(\frac{1}{\sqrt{a^2+u^2}}-\frac{1}{2h+u}\right)du$$

$$\sim q_0\frac{1}{R_0}\int_0^{R_0}[\ln(2h+u)-2\ln(a/2)+\ln u]\,du+Q_0\frac{1}{R_0}\int_0^{R_0}\left(\frac{1}{\sqrt{a^2+u^2}}-\frac{1}{2h+u}\right)du$$

$$\sim q_0[(2h/R_0+1)\ln(2h+R_0)-(2h/R_0)\ln(2h)-2-2\ln(a/2)+\ln R_0]$$

$$+Q_0\frac{1}{R_0}[\text{Arcsinh}(R_0/a)-\ln(2h+R_0)+\ln(2h)]$$

$$\sim q_0[(2h/R_0+1)\ln(2h+R_0)-(2h/R_0)\ln(2h)-2-2\ln(a/2)+\ln R_0]$$

$$+Q_0\frac{1}{R_0}[\ln(2R_0/a)-\ln(2h+R_0)+\ln(2h)]$$

$$\sim q_0[2\ln(2h/a)+(2/p+1)\ln(1+p/2)-2+\ln(2p)]$$

$$+Q_0 \frac{1}{ph} \left[\ln \left(2h/a \right) + \ln \left(2p \right) - \ln \left(2 + p \right) \right]$$

or

$$4\pi\varepsilon_0 V \sim q_0 \left[\Omega + \left(2/p + 1 \right) \ln \left(1 + p/2 \right) - 2 + \ln \left(2p \right) \right]$$

$$+Q_0 \frac{1}{ph} \left[\Omega/2 + \ln \left(2p \right) - \ln \left(2 + p \right) \right] \tag{141}$$

where we have set $R_0 = ph$. Because we want a long rod we take, say $p \approx 10$ (other choices of this order do not lead to significantly different results). It is to be noted that the actual behavior of the linear charge density for a semi-infinite rod is inversely logarithmic with the axial distance from the gap [21]. The reason for this dependence on the stopping distance R_0 results from the approximation of constant linear charge density.

The second match condition is taken at the tip of the hemisphere

$$4\pi\varepsilon_0 V \sim q_0 \left(\Omega/2 - \frac{a}{2h} \right) + Q_0 \frac{1}{a} \left(1 - \frac{a}{2h} \right) \tag{142}$$

The field on axis at general z is then

$$-E_z = E \sim \frac{q_0}{4\pi\varepsilon_0} \left(\frac{1}{h+z} + \frac{1}{h-z} \right) + \frac{Q_0}{4\pi\varepsilon_0} \left[\frac{1}{\left(h - z \right)^2} + \frac{1}{\left(h + z \right)^2} \right] \tag{143}$$

This is used to define the ionization coefficient and carry out the ionization integration.

4.7.3 integral equation

Because of the fundamental nature of the rod-to-plane gap we have also solved the problem with an integral equation method. For numerical purposes it is convenient to replace the thin wire Green's function by the exact elliptic kernel form

$$\frac{1}{\sqrt{(z-z')^2 + \rho^2}} \Rightarrow \frac{1}{2\pi} \int_0^{2\pi} \frac{d\varphi'}{\sqrt{(z-z')^2 + (\rho \sin\varphi - \rho' \sin\varphi')^2 + (\rho\cos\varphi - \rho'\cos\varphi')^2}}$$

$$= \frac{2/\pi}{\sqrt{(z-z')^2 + \left(\rho + \rho' \right)^2}} \int_0^{\pi/2} \frac{dt}{\sqrt{(1 - \xi^2 \sin^2 t}}$$

$$= \frac{\xi}{\pi\sqrt{\rho\rho'}} K\left(\xi \right) \tag{144}$$

where the complete elliptic integral of the first kind is

$$K(\xi) = \int_0^{\pi/2} \frac{dt}{\sqrt{1 - \xi^2 \sin^2 t}} \tag{145}$$

and

$$\xi = \sqrt{\frac{4\rho\rho'}{(z-z')^2 + \left(\rho+\rho'\right)^2}} \tag{146}$$

Inserting the images and the integration over the hemisphere gives the integral equation

$$4\pi\varepsilon_0 V = \int_h^R q_c\left(z'\right)\left[\frac{\xi}{\pi\sqrt{\rho a}}K\left(\xi\right) - \frac{\xi^*}{\pi\sqrt{\rho a}}K\left(\xi^*\right)\right]dz'$$

$$+\int_0^{\pi a/2} q_s\left(s'\right)\left[\frac{\xi}{\pi\sqrt{\rho\rho'}}K\left(\xi\right) - \frac{\xi^*}{\pi\sqrt{\rho\rho'}}K\left(\xi^*\right)\right]ds' \tag{147}$$

where

$$\xi^* = \sqrt{\frac{4\rho\rho'}{(z+z')^2 + \left(\rho+\rho'\right)^2}} \tag{148}$$

Note that in the first integral

$$\rho' = a$$

and in the second integral

$$a\varphi' = s' - \pi a/2$$

$$\rho' = a\cos\varphi' = a\sin\left(s'/a\right)$$

$$z' = h + a\sin\varphi' = h - a\cos\left(s'/a\right)$$

The cylindrical surface has

$$\rho = a$$

and the hemispherical surface has

$$a\varphi = s - \pi a/2$$

$$\rho = a\sin\left(s/a\right)$$

$$z = h - a\cos\left(s/a\right)$$

We think of $s' = a\varphi'$. Now the solution is found as the basis expansions

$$q_c\left(z'\right) = \sum_{n=1}^{N_c} q_n p_n\left(z'\right)$$

$$q_s\left(s'\right) = \sum_{n=1}^{N_s} q_n p_n\left(s'\right)$$

$$p_n\left(z'\right) = 1\ ,\ z'_{n-1} < z' < z'_n$$

$$= 0\ ,\ \text{otherwise}$$

$$z'_0 = h$$

$$z'_{N_c} = R$$

$$s'_0 = 0$$

$$s'_{N_s} = \pi a/2$$

$$z_n = \left(z'_n + z'_{n-1}\right)/2\ ,\ n = 1, ..., N_c$$

$$s_n = \left(s'_n + s'_{n-1}\right)/2\ ,\ n = 1, ..., N_s$$

We will take the basis function distributed according to

$$s'_n = \left(\pi a/2\right) n/N_s$$

$$z'_n = h + \Delta \sum_{m=0}^{n-1} \nu^m = h + \Delta \frac{\nu^n - 1}{\nu - 1}$$

$$\left(R - h\right) \frac{\nu - 1}{\nu^{N_s} - 1} = \Delta$$

A comparison of the axial electric field on axis is shown in Figure 10 for $d = 1$ cm and in 11 for $d = 4$ cm with $a = 0.2$ cm.

5 COMPUTATIONAL AND ANALYTICAL RESULTS

In this section we compare breakdown calculated by the code EIGER_S to breakdown calculated analytically and further to breakdown obtained experimentally for various geometries. In many cases, the choice of breakdown geometry was influenced by the current device of interest with respect to breakdown calculations – a stronglink switch. In other cases, the choice of breakdown geometry was influenced by the availability of an analytical field solution or the availability of experimental data. In all of the cases examined, the gas through which breakdown occurs, is air at near one atmosphere (760 Torr). The results

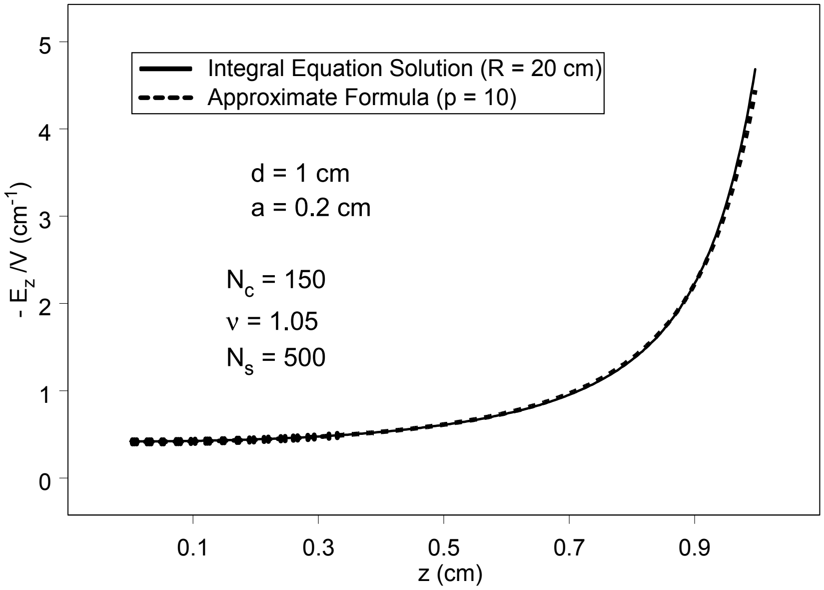

Figure 10. Comparison of axial field in a rod plane geometry. The numerical solution of the integral equation and the approximate formula are compared.

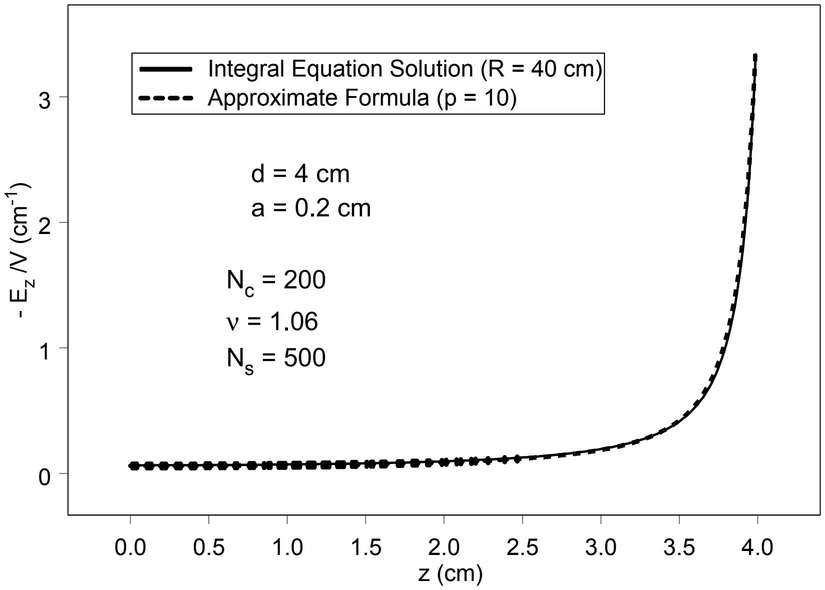

Figure 11. Comparison of axial field in a rod plane geometry. The numerical solution of the integral equation and the approximate formula are compared.

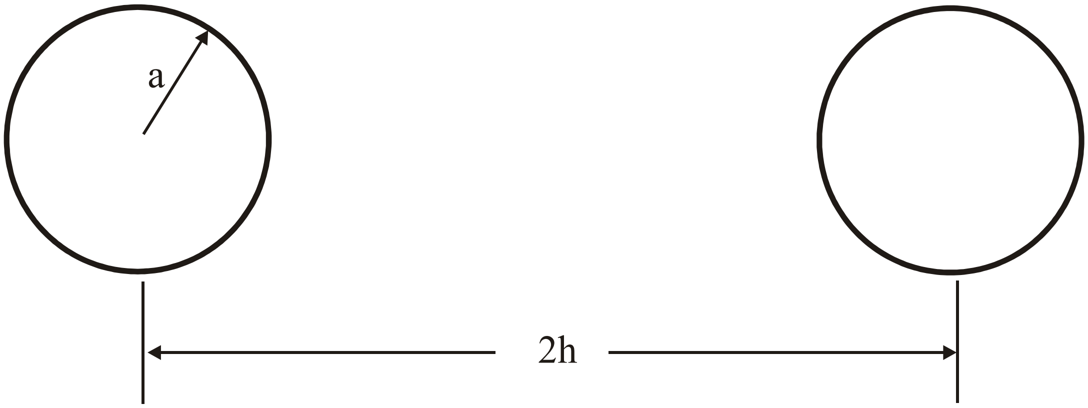

Figure 12. Two-sphere geometry.

are listed chronologically in the order in which they were obtained during the course of this project.

5.1 Breakdown Between Two Spheres

The geometry for breakdown between two spheres is shown in Figure 12. We chose this geometry to begin our study because experimental results were available [18], calculation of the electric field could be done analytically (Section 4.6) to check the numerical solution, the two electrodes were symmetrical and by studying spheres with large radius and small spacing, the nonuniformity of the fields could be controlled.

5.1.1 field convergence study

We first checked the convergence of the field calculated numerically as a function of number of unknowns by examining the two sphere problem with $a = 1.25$ cm and $2h = 4.5$ cm (a 2.0 cm gap between the spheres). Each unknown represents a constant electrical charge density over the support of the surface element. The capacitance between the two spheres, calculated analytically, is 0.972 pF. The electric field normal to the surface of the sphere, calculated analytically, is 80.03 V/m if the voltage difference between the spheres is 1 volt.

Table 4 shows the number of unknowns needed to discretize the spheres in column two, the capacitance calculated numerically in column four, the relative error between the numerical and analytical capacitance in column five, the electric field normal to the surface of the sphere calculated numerically in column six and the relative error between the numerical and analytical normal E field in column seven.

5.1.2 breakdown comparison

We use the following procedure to numerically calculate the breakdown voltage between the two spheres. We first use EIGER_S to solve for the charge density on the two spheres, assuming a 1 volt potential difference between them. We then begin in the center of an element located on the cathode sphere, calculate the electric field and find the first ionization coefficient (α) using the formulas derived previously that relate α/p to E/p in air at 760 Torr. Following the E field path we progress from cathode towards the anode integrating αds. We stop the integration when one of two events happens: the integration exceeds a threshold value (αd) or we hit the anode. If we exceed the threshold value, we scale down the charge density on the spheres to effectively decrease the potential difference between them, and repeat the path integration. Conversely, if we hit the anode we scale up the charge density on the spheres to effectively increase the potential difference between them, and repeat the path integration. We continue

Grid Title	Number of Unknowns	Element Size	C (pF)	R.E (%)	E (V/m)	R.E. (%)
Grid1	720	3.75 mm, uniform	0.951	2.16	78.9	1.4
Grid2	1120	1.06 mm	0.955	1.75	81.1	1.3
Grid3	1520	0.84 mm	0.957	1.54	80.8	0.96
Grid4	3040	0.67 mm	0.960	1.23	80.4	0.46
Grid5	6240	0.90 mm, uniform	0.969	0.31	80.1	0.087

Table 4.Convergence study of capacitance between two spheres and surface field.

to adjust the potential difference until we attain the threshold at the same point that we hit the anode. The threshold value (αd) is dependent on the gap ($d = 2h - 2a$) and is given by F defined in (17).

Table 5 shows a comparison of breakdown voltage as a function of gap distance (column one) between measured data in column two [18], a numerical calculation in column four, using Grid5, which is shown in Figure 13 and referenced in the last row of the Table 4, and an analytical calculation in column six. The relative error between measured and numerical results is given in column five and the relative error between measured and analytical results is given in column seven. The threshold value is given in column three. The sphere radius is fixed at $a = 1.25$ cm.

5.2 Breakdown Between Two Wires

The next breakdown problem we decided to look at was the two wire geometry shown in Figure 14. This geometry was chosen because experimental data exists [13], an analytical formulation of the electric field exists and the two electrodes are symmetrical. The experimental data is for dimensions that cause the field to be highly non-uniform, which is why we wanted to examine this problem

Table 6 shows a comparison of electric field at the surface of the wire as a function of wire radius (column one) and wire spacing (column two). The measured data shown in column three is found in [13] and is reproduced in Figure 15 for convenience. The threshold value is given in column four. The numerical results are shown in column five with the relative error between numerical solution and measured solution shown in column six. The numerical results shown in row one and three were obtained using 162 unknowns to discretize the two wires, while the row two result was obtained using 300 unknowns. The analytical solution is shown in column seven with relative error between it and the measured results shown in column eight. In row one, the ratio between maximum and minimum electric field is 6.3. In row two, the ratio is 5.75 and in row three the ratio is 19.7. So our goal of examining highly non-uniform fields is realized.

Note that the radius and spacing of rows one and two are such that they fall in the region labeled "spark before corona" in Figure 15. In this region, as voltage between the two wires is increased, a spark is the first breakdown phenomena to occur and we are able to predict the breakdown voltage levels to within 15%. The radius and spacing of row three, on the other hand, falls into the region labeled "corona before spark" and our prediction of the breakdown voltage level is completely off. The reason for this discrepancy is that the calculation is, in this case, predicting the level at which corona breakdown occurs, not the level at which spark breakdown occurs, which is a much higher voltage level. We mentioned above that the minimum field could be used to give some indication whether spark or corona is likely. Using the formula (116), the mimimum steamer sustaining field level (29), and the nominal breakdown level for air of 30 kV/cm (which is near the maximum field level for small wire spacings in Figure 15), we write

$$2h/a \sim 4E_{\max}/E_{\min} \approx 4\,(30 \text{ kV/cm})\,/\,(4.7 \text{ kV/cm}) = 25.5$$

It is noted in Figure 15 that the spacing (approximately $2h$) to radius ratio for the corona - spark boundary

d (cm)	V_b^{meas}(kV)	αd	V_b^{num}(kV)	R.E. (%)	V_b^{an}(kV)	R. E. (%)
0.27	10	10.8	10.3	3.0	10.1	1.3
2.0	50	18.1	52	4.0	51.8	3.7
4.05	70	19.1	74	5.8	74.0	5.8

Table 5.Comparison of experimental (from Handbook of Chemistry and Physics," editor R. C. Weast [18]), numerical, and analytic breakdown voltages between spheres.

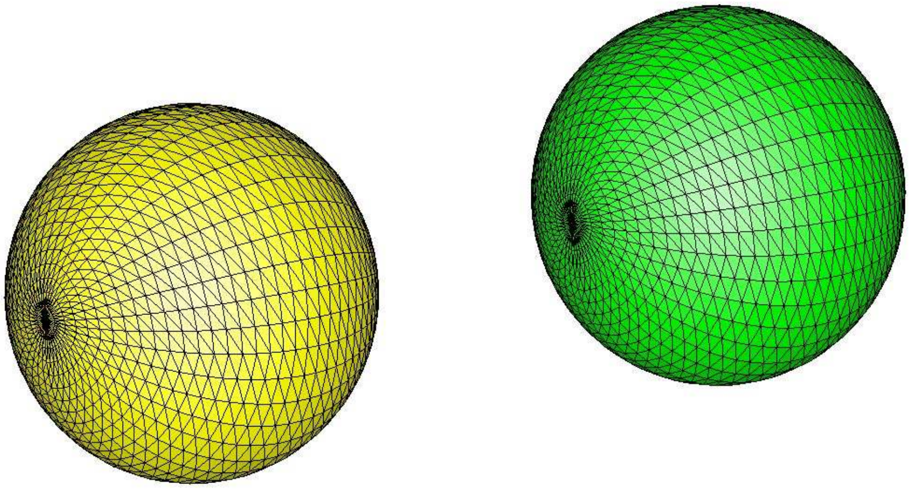

Figure 13. Grid5 of two-sphere geometry.

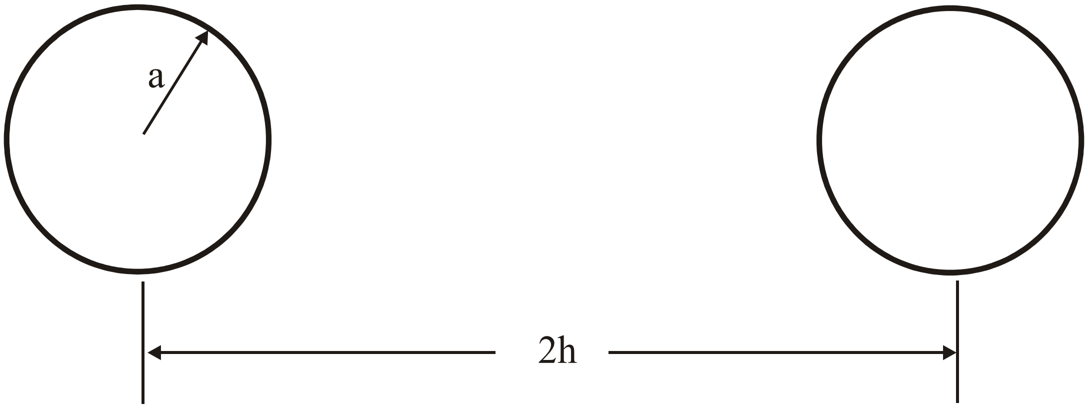

Figure 14. Two-wire geometry.

a (cm)	2h (cm)	$E_{\max}^{meas}$ (kV/cm)	αd	$\mathrm{E}_{\max}^{num}$ (kV/cm)	R.E. (%)	$\mathrm{E}_{\max}^{an}$ (kV/cm)	R.E. (%)
0.129	3	50	18.7	57	14	57.7	15.4
0.476	10	40	19.9	43.8	9.5	44.3	10.7
0.129	10	95	19.9	57.8	39	58.9	38

Table 6.Comparison of experimental, numerical, and analytic breakdown voltages between parallel wires [13].

is approximately 30, which is not too different from this estimate. More comparisons using this minimum field criterion will be performed below on other canonical problems with gaps limited to several centimeters (which is the upper limit of the range of interest in these applications).

5.3 Coaxial Breakdown

The next breakdown problem we decided to look at was the coaxial geometry shown in Figure 16. This geometry was chosen because experimental data exists [6] – including data on voltage levels for corona, an analytical formulation of the electric field exists and the two electrodes are asymmetrical. Asymmetrical electrode geometries occur often in practice and it is known that breakdown sometimes occurs easier for one polarity than another depending on the gas pressure and other factors.

Table 7 shows a comparison of breakdown voltage as a function of inner conductor radius (column one). The measured data listed in column two is found in [6] and is as the black curves in Figure 17. The threshold value is given in column three. The numerical results are shown in column four with the relative error between numerical solution and measured solution shown in column five. The numerical results shown in row one were obtained using 79 unknowns to discretize the outer conductor and 63 unknowns to discretize the inner conductor. In rows two and three, the results were obtained using 79 unknowns to discretize the outer conductor and 25 unknowns to discretize the inner conductor. The outer conductor was taken as the anode and its radius was fixed at $b = 5$ cm.

In row one, spark occurs before corona and the model predicts the breakdown voltage to within 1%. In rows two and three, the geometry is such that corona occurs before spark. Experimental results show both the voltage required for spark breakdown (row 2) and the voltage required for corona breakdown (row 3). Our model predicts the corona breakdown within about 8%. The relative errors here are taken versus the average breakdown voltage with respect to polarity from the experiment.

The blue and red solid and dashed curves (solid to the right of the dashed branch) in Figure 17 represent the breakdown calculations (blue is from simulations, red is the analytical caluculations).

5.3.1 minimum field criterion

The spark voltages are shown as the solid curves in the figure which branch away from the breakdown criterion dashed corona curves. Again the blue represents simulations and the red represents analytical calculations. The proposed minimum sustaining field criterion of Section 2.3 appears to be useful in differentiating between corona and spark.

5.4 Rod to Plane Geometry

A three dimensional geometry of great practical interest is the rod-to-plane. Here we have a cylindrical rod of radius $a = 0.2$ cm with hemispherical end cap. The distance from tip to ground plane is d. The grid is shown in Figure 18. The breakdown condition was implemented in the simulation (no experimental

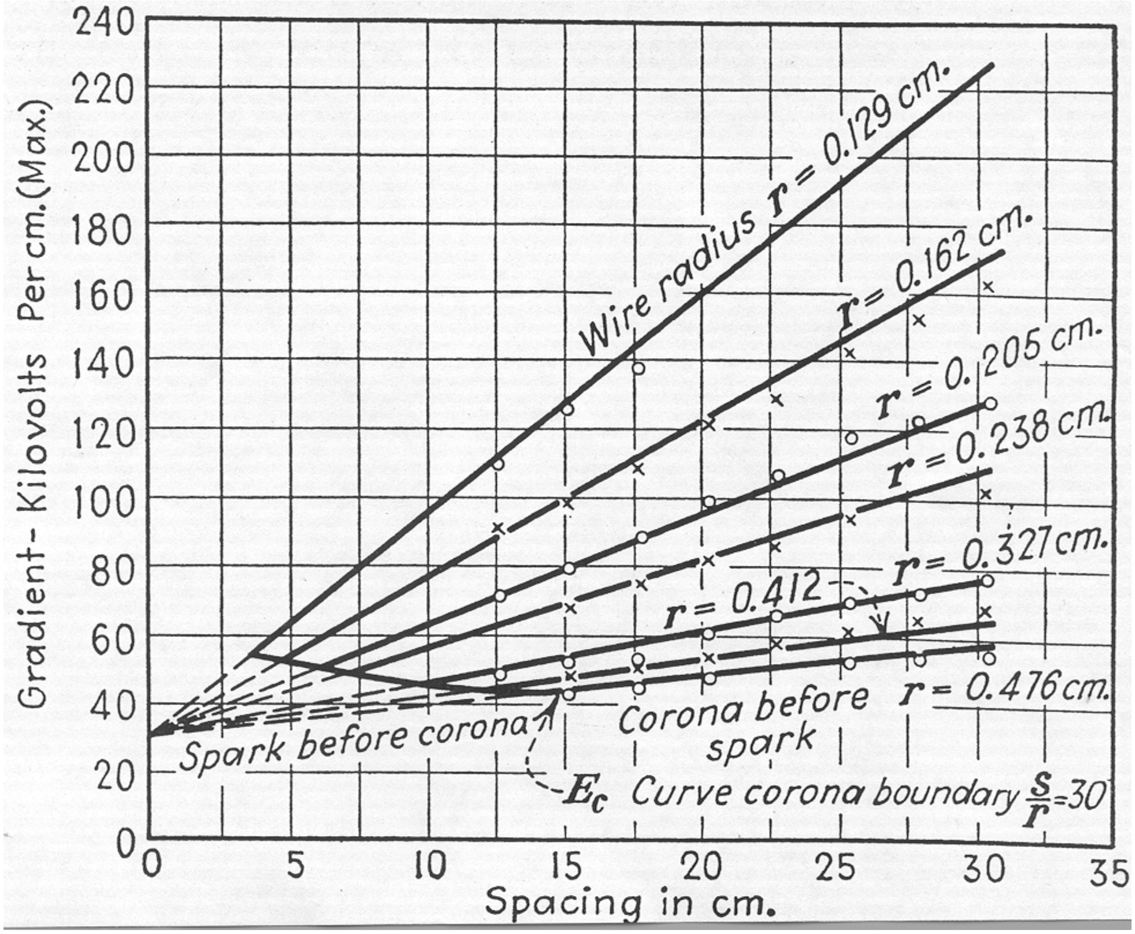

Figure 15. Experimental data for wire-wire breakdown (from "Gaseous Conductors," J. D. Cobine [13]).

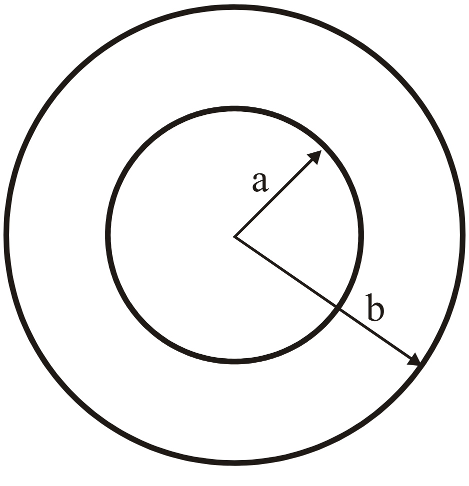

Figure 16. Coaxial geometry.

a (cm)	V_b^{meas} (kV)	αd	V_b^{num} (kV)	R.E. (%)	V_b^{an} (kV)	R.E. (%)
2.0	69.5(-)/71(+)	18.8	70	0.4	70	0.4
0.4	64(-)/59(+)	19.2	53	14	52.9	14
0.4	48(-)/50(+) (corona)	19.2	53	8	52.9	8

Table 7.Comparison of experimental, numerical, and analytic breakdown voltages in a coaxial geometry [6].

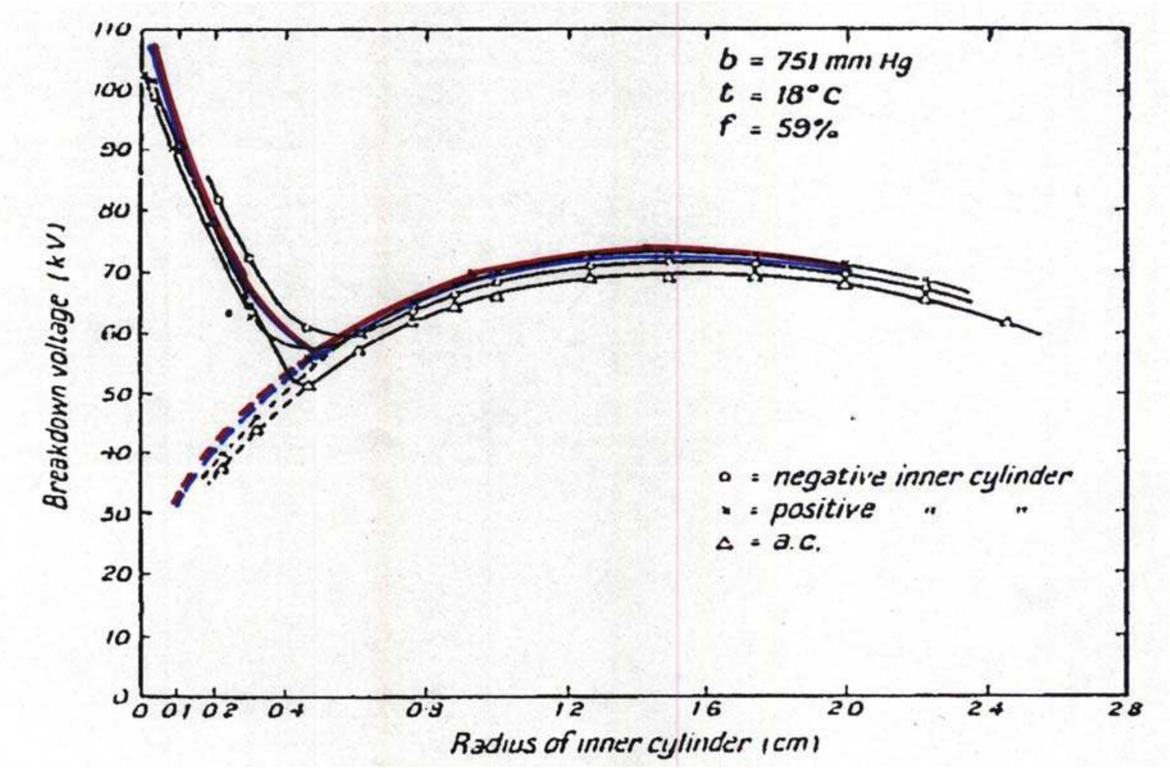

Figure 17. Comparison between spark (solid curves) and corona (dashed curves) predictions and experimental data for a coax of outer radius $b = 5$ cm (from "Electrical Breakdown of Gases, J. M. Meek and J. D. Craggs [6]). The red curves represent analytic calculations and the blue curves represent numerical calculations.

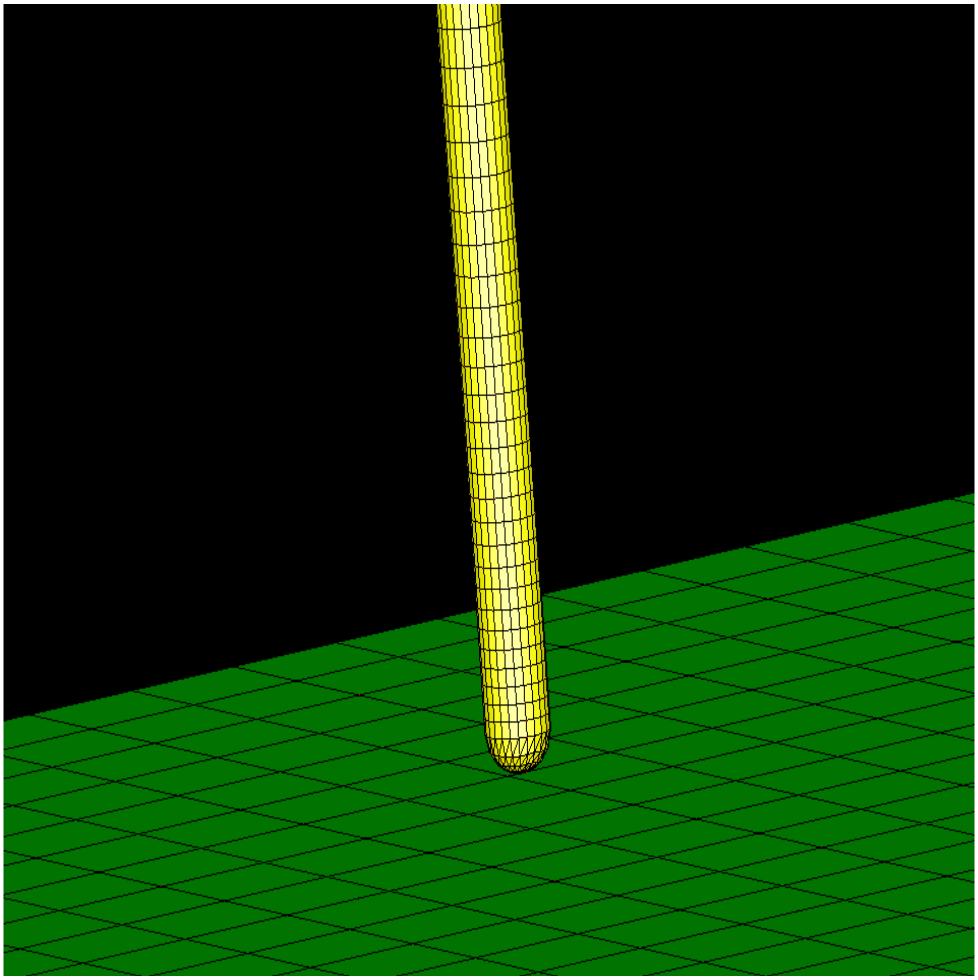

Figure 18. Grid used in modeling rod-to-plane field geometry.

results were available for the breakdown condition) and shown in the figure as the dashed blue curve. The approximate analytical breakdown condition is shown as the dashed red curve. The minimum field criterion was applied as the solid red (analytical) and blue (numerical) curves. Again it seems to be giving useful information as to when the spark and corona voltage levels diverge. The eventual divergence of the experimental curves from these predictions is thought to result from leader (and possible space charge) phenomena when the polarity dependence sets in.

5.5 Parallel Plate Geometry

The next breakdown problem is shown in Figure 20. This geometry was chosen because experimental data exists [7], an analytical solution exists and we wanted to apply the code to a geometry that had a uniform field but a very small gap (0.2 mm) that was encountered in certain stronglinks to see the errors that might manifest themselves due to calculation of α and setting the threshold αd. For a 0.2 mm gap, setting $\alpha d = 8.58$ we found that $V_b^{num} = 1.43$ kV compared to $V_b^{meas} = 1.53$ kV [7], leading to a relative error of less than 7%.

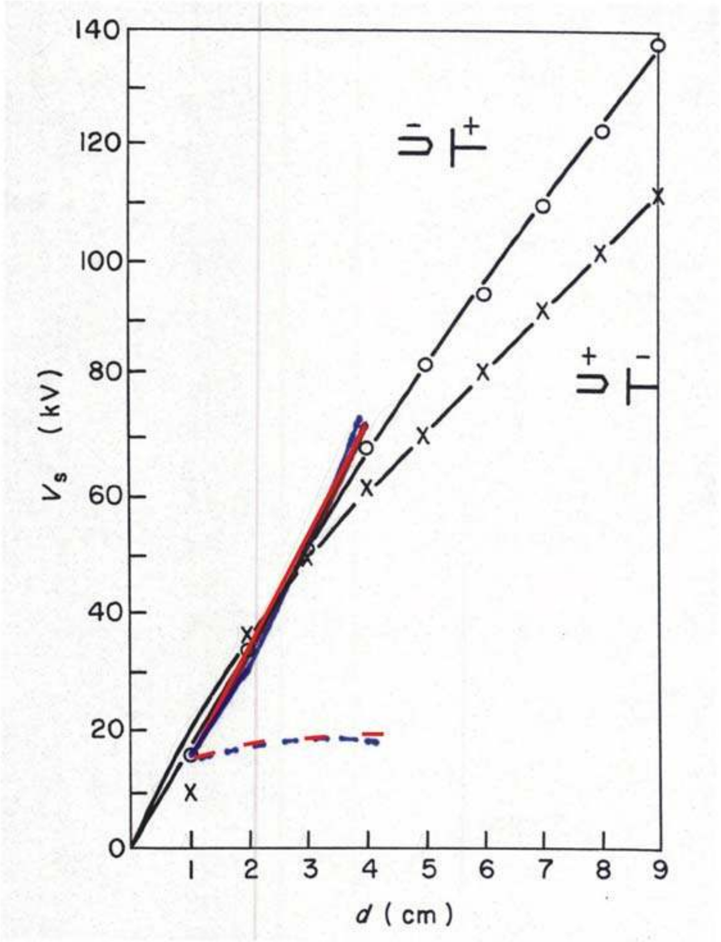

Figure 19. Comparison of spark predictions analytical approximation (red curve) and numerical simulations (blue curves) with experimental data (from "Electrical Breakdown of Gases," editors J. M. Meek and J. D. Craggs [7]) in a rod - plane geometry. The radius and hemispherical cap have radius $a = 0.2$ cm. The gap is d. Also shown is the corona prediction (dashed curve) from numerical simulation and analytical model.

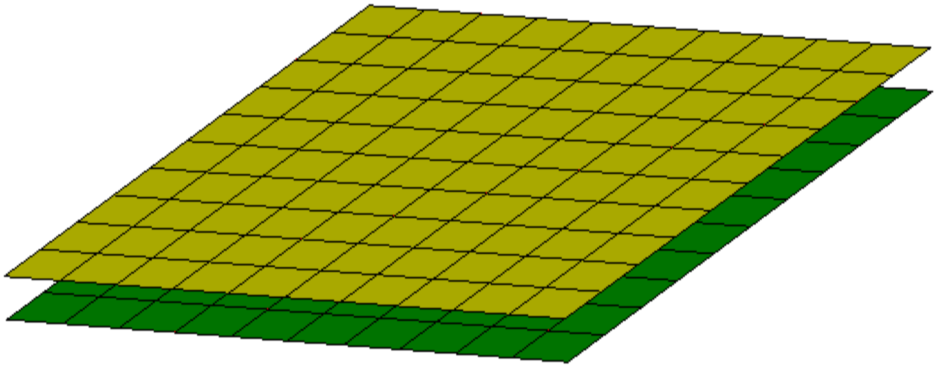

Figure 20. Grid of parallel plane geometry.

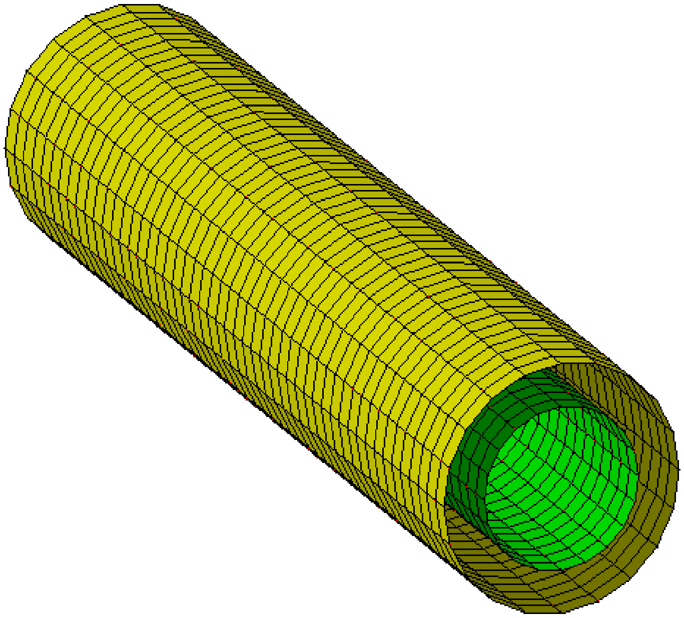

Figure 21. Coaxial geometry with 0.2 mm gap.

5.6 3D Coaxial Geometry

The next breakdown problem is shown in Figure 21, which again is motivated by geometries found in the stronglink. Here the outer radius is 0.58 mm while the inner radius is 0.38 mm. We found that breakdown occurred across the 0.2 mm gap at 1.42 kV – slightly below that of the parallel plane geometry. This reinforces our intuition that non-uniform fields will breakdown easier than uniform fields.

5.7 Breakdown From a Corner to a Plane

The last breakdown problem, shown in Figure 22, is again motivated by geometry found in the stronglink and is included to demonstrate how the technique to find the breakdown voltage must be modified when the geometry includes a corner. In this case the two-dimensional corner is located 0.2 mm away from a ground plane ($w = 0.2$ mm). Since the radial electric field near a corner is singular, the numerical solution is unreliable near a corner. We, therefore, used a two-dimensional analytic solution of the field near the corner and integrated α along a straight path from the corner to a point r_0 away from the corner. The potential is taken as

$$\phi \sim A_0 \rho^{\pi/(2\varphi_0)} \cos\left(\frac{\pi\varphi}{2\varphi_0}\right) \text{ , } -\varphi_0 < \varphi < \varphi_0$$

with field

$$E_\rho \sim -\frac{\pi A_0}{2\varphi_0} \rho^{\pi/(2\varphi_0)-1} \cos\left(\frac{\pi\varphi}{2\varphi_0}\right) \tag{149}$$

Along the bisector $\varphi = 0$

$$E_\rho \sim -\frac{\pi A_0}{2\varphi_0} \rho^{\pi/(2\varphi_0)-1} \tag{150}$$

Using

$$\alpha/p = Ae^{-Bp/E}$$

we have

$$\int_0^{\rho_0} \alpha ds \sim pA \int_0^{\rho_0} e^{-\rho^{1-\pi/(2\varphi_0)} Bp2\varphi_0/(\pi A_0)} d\rho \tag{151}$$

For the right angle corner $2\varphi_0 = 3\pi/2$ and

$$\int_0^{\rho_0} \alpha ds \sim 3pA \int_0^{\sqrt[3]{\rho_0}} e^{-uB_0} u^2 du$$

$$= 3pA\left[2 - e^{-B_0\sqrt[3]{\rho_0}}\left(B_0^2 \rho_0^{2/3} + 2\rho_0^{1/3} B_0 + 2\right)\right]/B_0^3 \tag{152}$$

where

$$B_0 = Bp3/\left(2A_0\right) \tag{153}$$

The straight path makes an angle of φ_0 with the corner walls as shown in the solid line in Figure 22. At ρ_0, the analytic solution for E_ρ is matched to the numerical solution to determine the coefficient A_0. The preceding contribution (there may need to be several forms of the ionization coefficient used) is taken as an initial value of the integration and the numerical integration of α continues along a field line or along a user defined path.

If we follow the field line in the parallel plate region of the problem, 0.275 mm from the corner, we find that $V_b^{num} = 1.43$ kV, the same as the parallel plate problem solved in Section 5.5. Setting $\rho_0 = 0.0707$ mm and following the field line, we find that $V_b^{num} = 1.51$ kV (versus the analytic result $V_b^{anal} = 1.46$ kV) – breakdown at the edge predicted by this model requires a higher voltage than breakdown in the parallel plate region, which is surprising. If we do not follow a field line, but follow a direct path from corner to ground plane, $V_b^{num} = 1.38$ kV.

If we increase the spacing between the corner and ground plane to ($w = 0.5$ mm) we find that breakdown in the parallel plate region, 0.275 mm from the corner, is $V_b^{num} = 2.67$ kV, which compares to $V_b^{meas} = 2.7$ kV found in [7]. Now if we follow the field line from the corner, we find that $V_b^{num} = 2.67$ kV, which corresponds to what was found analytically: These results indicate that when $w > 0.35$ mm

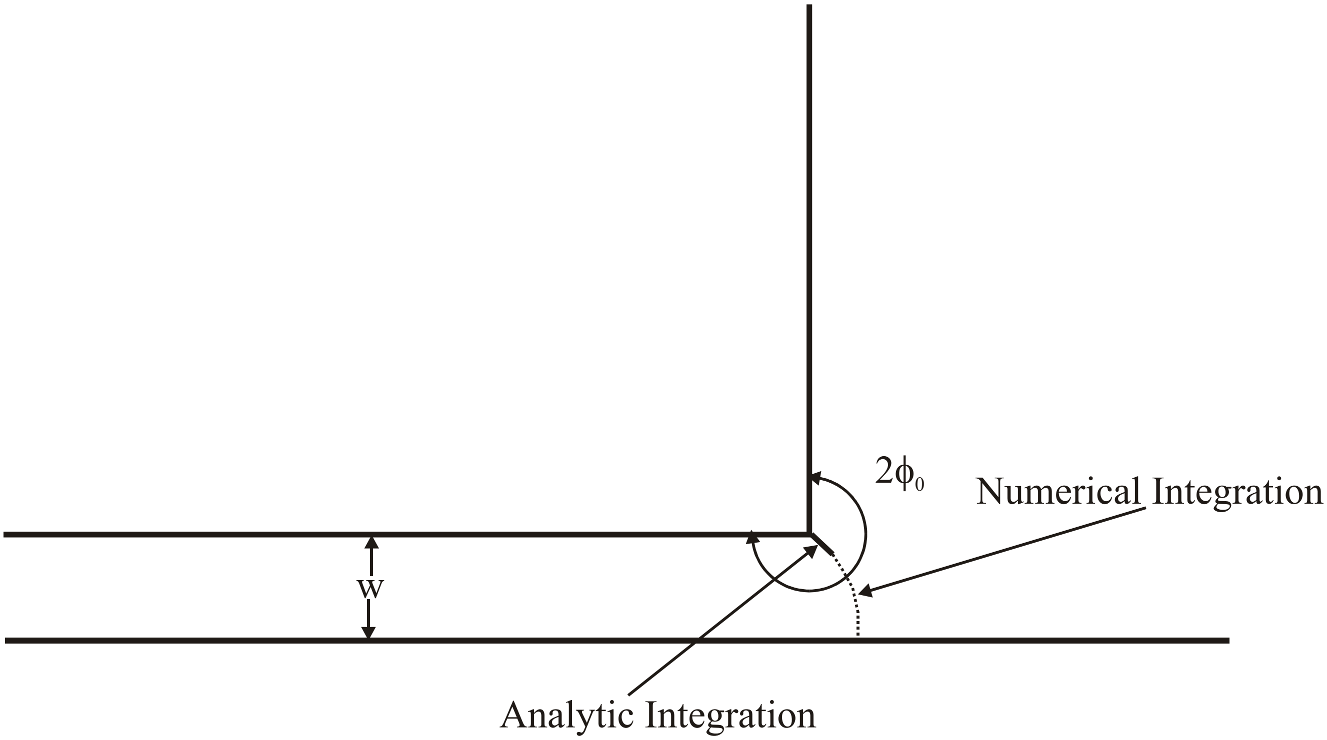

Figure 22. Two-dimensional corner problem.

predicted breakdown, using (96), occurs preferentially at the corner, while if $w < 0.35$ predicted breakdown occurs preferentially in the parallel plate region.

6 UNCHARGED DIELECTRIC SURFACE

This section considers the development of an electron avalanche near an uncharged dielectric surface. The microscopic processes taking place at the surface and in the gas are incorporated into a Monte Carlo code which simulates the avalanche. The avalanche is begun by suddenly injecting a cloud of electrons in an imposed uniform field and tracking the subsequent development of the avalanche to see the impact of the surface. The effective primary ionization coefficient is examined to ascertain impact of the surface processes.

6.1 Growth of an Electron Avalanche Near the Surface

In this subsection we use the Monte Carlo code BREAKDOWN to study the growth of an electron avalanche as it crosses a dielectric surface. We will incorporate the results into BREAKDOWN_ALPHA, the code that we have been using to predict numerical breakdown voltages in this report, so that we can calculate breakdown across dielectric surfaces in realistic electrode geometries.

Although the geometries that we are actually concerned with involve breakdown across complex surfaces with complex electrodes that lead to highly non-uniform fields, we will obtain Monte Carlo results from a simplified geometry: an infinite, dielectric, half-space with no electrodes as shown in Figure 23. A uniform electric field, $\overline{E}_{inc} = -\widehat{z}E_{inc}$ is applied parallel to the surface of the dielectric, which fills the

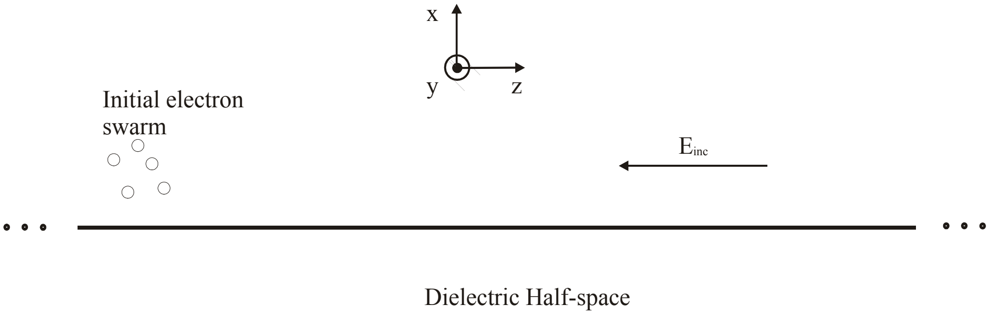

Figure 23. Monte carlo dielectric surface geometry.

region $x \leq 0$. At time $t = 0$, a small number of initial electrons ($n_0 = 10 - 1000$) uniformly distributed in a small sphere about the origin (radius $\sim 1\mu$m), are allowed to move in the electric field. We track the progress of each individual electron as it is accelerated by the electric field and undergoes collisions with the background neutral gas molecules and with the dielectric surface. Included phenomena that affect the growth of electrons are: ionization due to electron collision with a neutral, ionization due to photoionization, photoemission from the dielectric surface and secondary electron emission from the dielectric surface. We can thus observe the behavior of the electron swarm as the breakdown develops. At the field levels studied here, the secondary electron emission phenomenon acts as a sink to the electrons in the avalanche – retarding the electron growth. More details on the code BREAKDOWN can be found in [22], [23].

Our strategy is to run BREAKDOWN to model the early-time stages of an avalanche that occurs in N_2 at 760 Torr for various values of electric field near breakdown threshold, which occurs at around 3 MV/m. The number of electrons in the electron swarm grows exponentially in time and space as it moves across the surface.

$$n(z) = n_0 e^{\alpha z} \tag{154}$$

where $n(z)$ is the number of electrons in the swarm as a function of z, n_0 is the number of starting electrons and α is the effective growth rate. α is due to several processes

$$\alpha = \alpha_{coll} + \alpha_{pi} + \alpha_{pe} - \alpha_{see} \tag{155}$$

where α_{coll} represents growth due to collisional ionization, α_{pi} is due to photoionization, α_{pe} is due to photoemission, and α_{see} is due to secondary electron emission. The photoionization process is illustrated in Figure 24. The photoelectrons liberated act as seeds to start new avalanche processes.

The photoemission process is illustrated in Figure 25. Lower energy photons (compared to ionization energies in the gas) are capable of liberating electrons to act as seeds for avalanches. Figures 26 and 27 show electron yields with an incident photon of a given energy for polyethylene and for Teflon. The formula 156 summarizes the data with parameters in the Table 8. It is clear from these two examples that energies well below the ionization threshold of the gas can liberate electrons from the dielectric surfaces. Table 9 shows some of the excitation photon energy levels emitted in nitrogen (that are available for impacting the surface).

$$Q = \begin{cases} 0 & \text{if } E_p < E_l \\ \left[s\left(E_p - E_l\right)\right]^3 & \text{if } E_l < E_p < E_b \\ Q_s & \text{if } E_b < E_p \end{cases} \tag{156}$$

Figure 28 shows the electron impact and secondary electron emission process. Figure 29 shows a canonical secondary electron emission curve used for various materials. Table 10 gives parameters to be used in the canonical curve for three dielectric materials. Figure 30 shows the normalized curves for Teflon

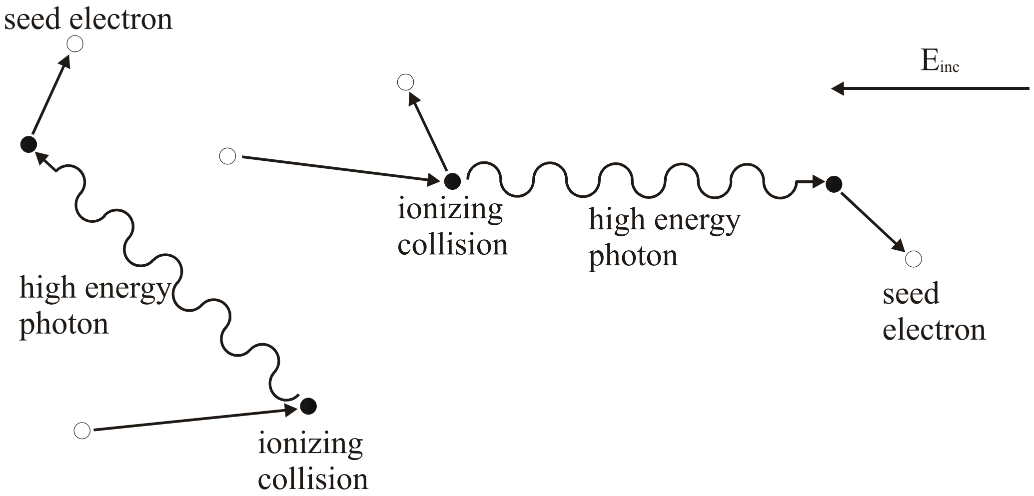

Figure 24. Illustration of photoionization process where high energy photons arising from collisions result in new seed electrons for avalanches.

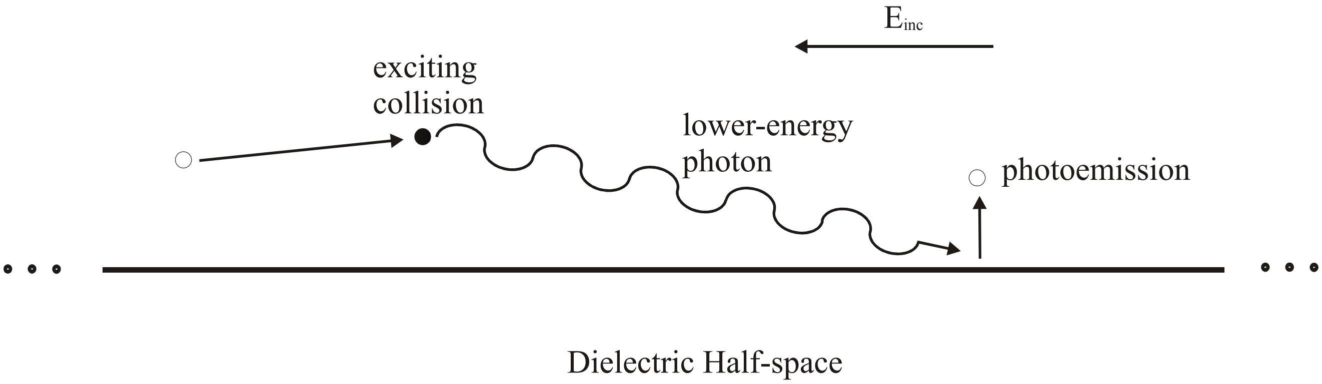

Figure 25. Illustration of photoemission process where lower energy photons result in new seed electrons from the surface that start new avalanches.

Material	E_l (ev)	$s\left(\text{ev}^{-1}\right)$	E_b (ev)	Q_s
Teflon	5.85	1.825×10^{-2}	37.85	0.199
Polyethylene	7.84	9.592×10^{-2}	13.67	0.176

Table 8.Polymer photoemission parameters [23].

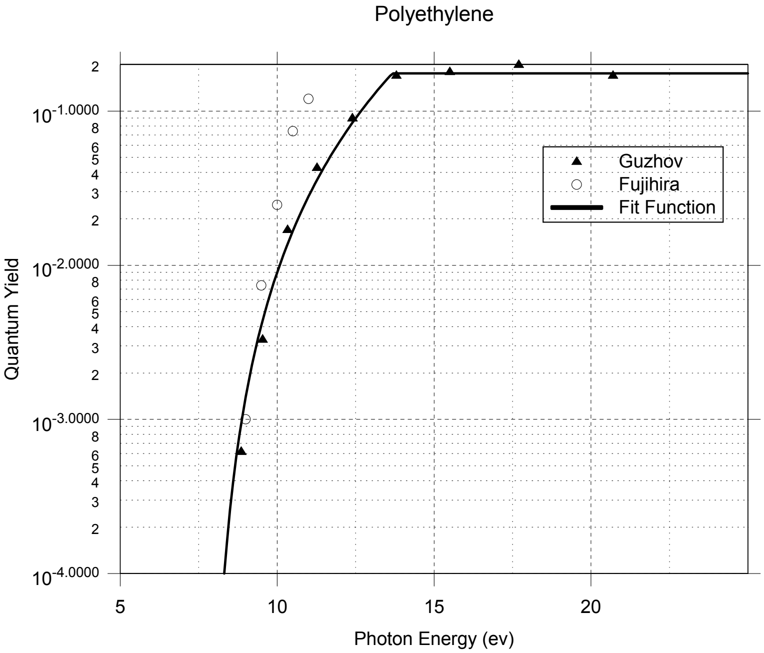

Figure 26. Electron emission yield as a function of energy for polyethelene [23].

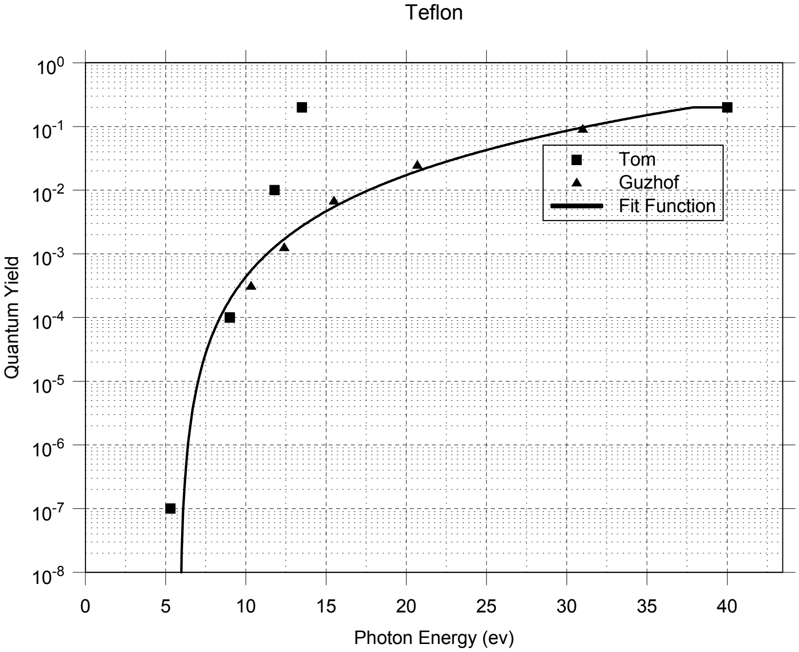

Figure 27. Electron emission yield as a function of photon energy for Teflon [23].

Energy Level Label	Threshold Energy (ev)	Spectral Band	Photon Energy Range (ev)
A$^3\Sigma_u^+$	6.17	Vegard-Kaplan	2.33 - 9.92
B$^3\Pi_g$	7.35	First Positive	0.49 - 2.59
		Vegard-Kaplan	2.33 - 9.92
W$^3\Delta_u$ (not shown)	7.36	Saum-Benesch	8.24 - 8.61
B'$^3\Sigma_u^-$	8.16	Ogawa-Tanaka-Wilkinson	5.54 - 11.07
a'$^1\Sigma_u^-$	8.40	Wilkinson-Mulliken	6.20 - 11.48
a$^1\Pi_g$	8.55	Lyman-Birge-Hopfield	4.77 - 12.40
w$^1\Delta_u$	8.89	McFarlane Infrared	0.15 - 0.41
		Lyman-Birge-Hopfield	4.77 - 12.40
C$^3\Pi_u$	11.03	Second Positive	2.27 - 4.63
		First Positive	0.49 - 2.59
		Vergard-Kaplan	2.33 - 9.92
E$^3\Sigma_g^+$	11.88	Herman-Kaplan	4.53 - 5.82
		Vergard-Kaplan	2.33 - 9.92
a"$^1\Sigma_g^+$	12.25	Dressler-Lutz	12.27
Singlet Systems	13.0	Gaydon-Herman	3.38 - 5.59
		Lyman-Birge-Hopfield	4.77 - 12.40
Singlet - Ground	13.0	Various names	9.54 - 15.50

Table 9.Excitation energy levels and spectral bands [23].

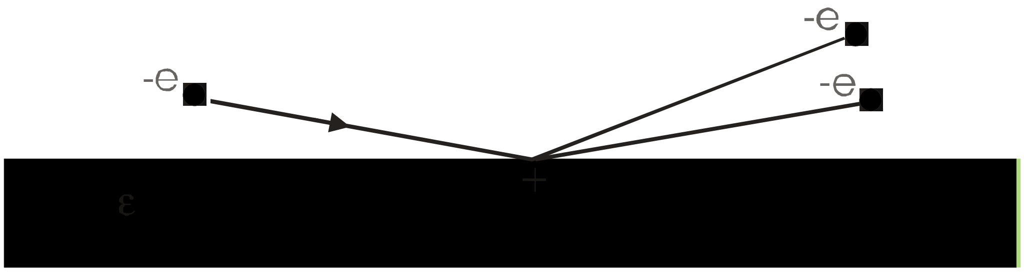

Figure 28. Illustration of secondary electron emission from a surface due to electron impact. If impact energies are low the incident electron is likely to attach to the surface.

and polyethylene. It is clear from these curves that typical electron energies in the breakdown of gases at atmospheric pressure lead to electron attachment (yields below unity). The purpose of the simulations below is to assess whether the surface acts as a net source or sink of electrons.

A typical growth curve with respect to time is shown in Figure 31 for a Teflon surface when $E/p = 52.63$ V/cm-Torr. The secondary electron emission causes the number of electrons to decrease from 1000 at $t = 0$ to 40 at $t = 1$ ns before exhibiting exponential growth. The position of the electron swarm's center of mass with respect to time is shown in Figure 32. From the center of mass, we can obtain a drift velocity of the swarm v and obtain an expression for α.

$$\alpha = \frac{1}{v\left(t_2 - t_1\right)} \ln\left(\frac{n\left(t_2\right)}{n\left(t_1\right)}\right) \tag{157}$$

The times t_1 and t_2 are chosen to bracket an interval where the number of electrons is growing exponentially (after 10 ns in Figure 31).

Figure 33, shows the number of electrons added to the swarm due to the processes of collision, photoionization and photoemission. Figure 34 shows the number of electrons taken from the swarm (and added to the dielectric surface) due to secondary electron emission. Note that in Figure 33 the collision process adds more electrons than the photoionization process, which, in turn adds more than the photoemission process.

It is desirable to calculate the α due to each of these processes. To calculate α_{coll}, for example, we know that at a particular time t_k

$$\alpha_{coll} = \frac{1}{n}\frac{dn_{coll}}{dz} \tag{158}$$

During the Monte Carlo simulation, we track the number of electrons added to the swarm due to each process over a short time period about t_k. This gives us dn_{coll}. Further, we know dz over this time period from Figure 32 and n at t_k from Figure 31. The quantities α_{pi}, α_{pe} and α_{see} are calculated in a similar fashion. Unfortunately, the data are extremely noisy and the resulting α needs to be averaged over many values of t_k and over regions of time where the added charge is varying relatively smoothly. Figure 35 show the results of Equation 158 when applied to the total α (calculated previously by Equation 157). Note that the results are widely scattered between $\alpha = 1000$ to 5000 m^{-1}. The line passing through the center of the plot is a linear fit of the data, which varies between $\alpha = 3170$ m^{-1} at 20ns to $\alpha = 3000$ m^{-1} at 30ns. Equation 157 yields $\alpha = 3010$ m^{-1}.

6.2 Results of Avalanche Growth

We first calculate the values of α/p in N_2 for various values of E/p (where p is pressure in Torr)

Material	δ_m	ε_m	ϵ_r
Polyethylene	2.71	250	2.25
Teflon	2.12	400	2.1
Nylon	2.42	250	3.88

Table 10.Polymer secondary electron emission parameters [27].

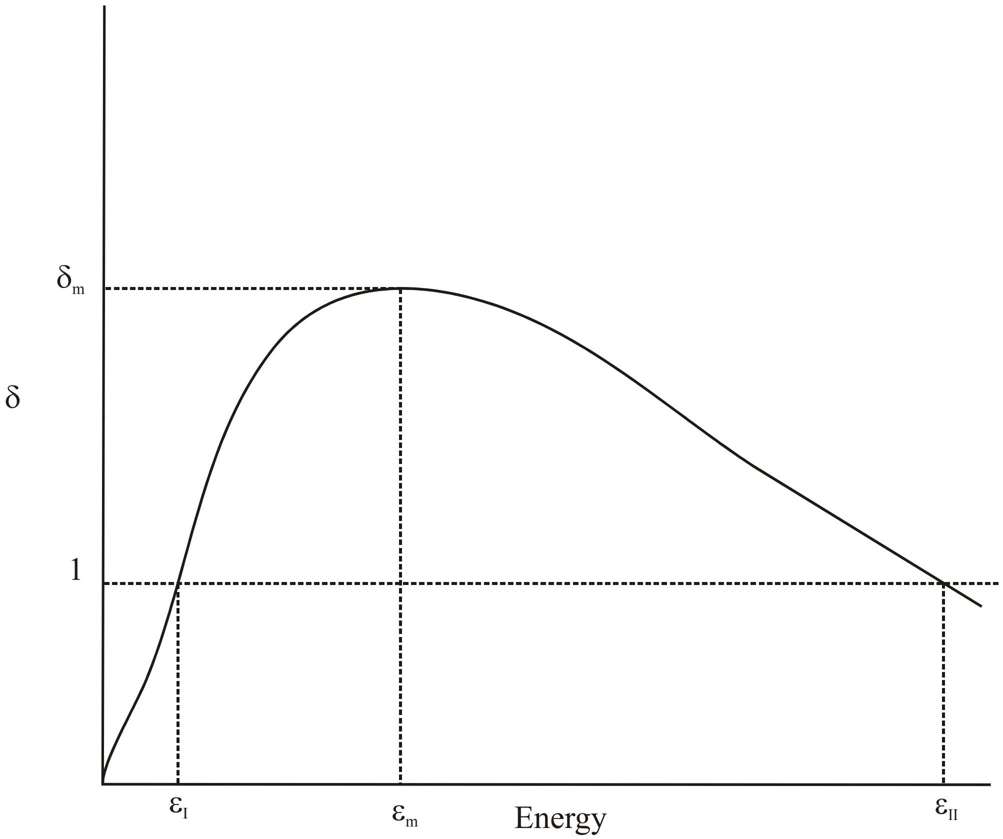

Figure 29. Canonical curve for secondary electron emission from a surface. Regions below unity represent likely electron attachment [23].

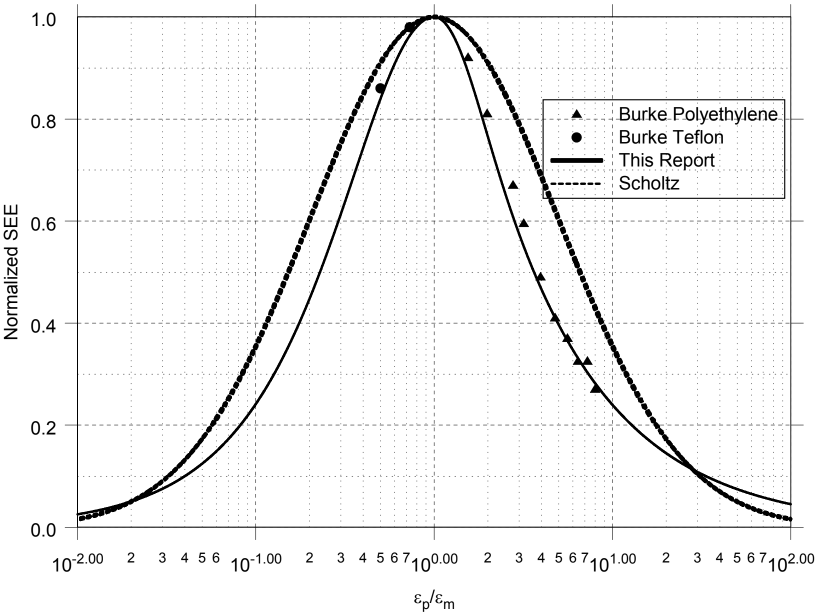

Figure 30. Secondary electron emission curves for polyethylene and for Teflon [23].

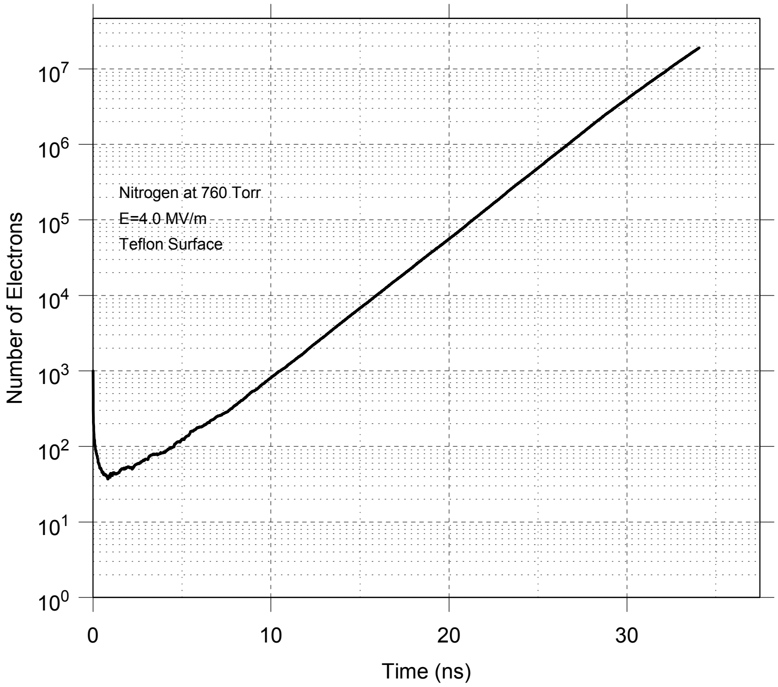

Figure 31. Number of Electrons vs. Time

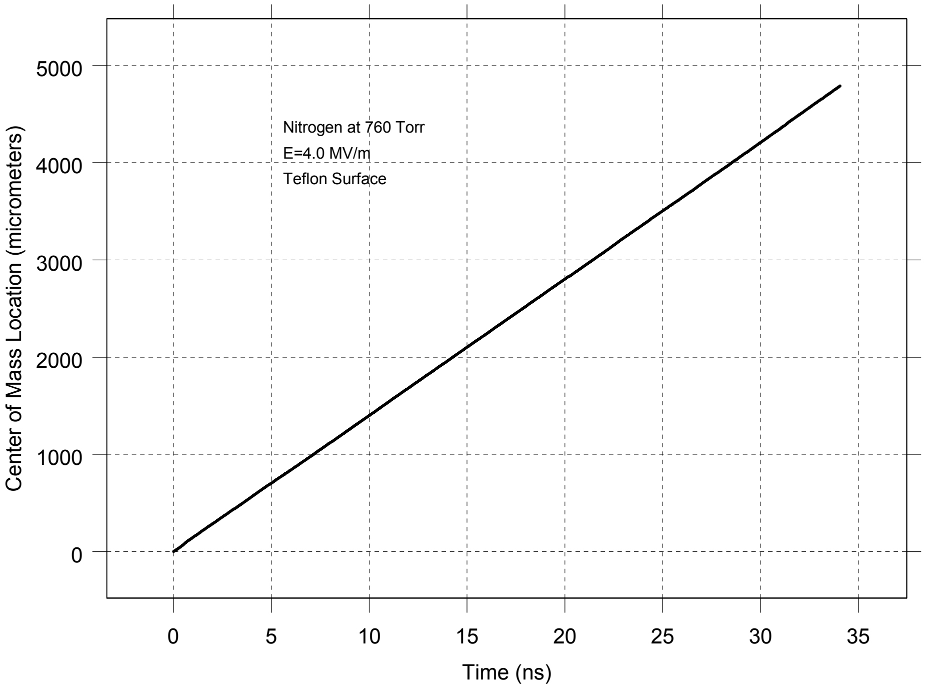

Figure 32. Electron swarm center of mass vs. time.

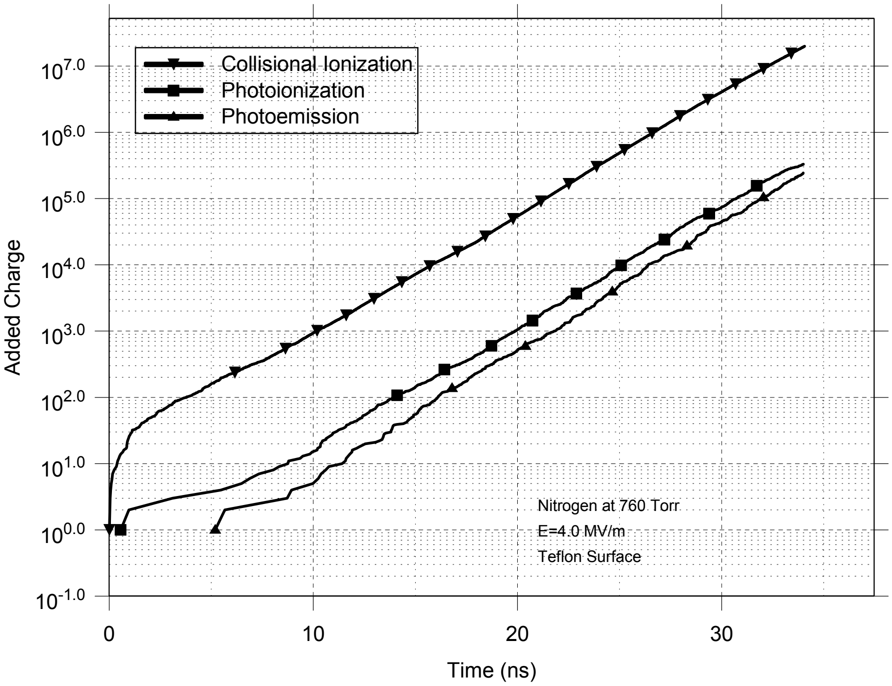

Figure 33. Added charge due to three processes vs. time.

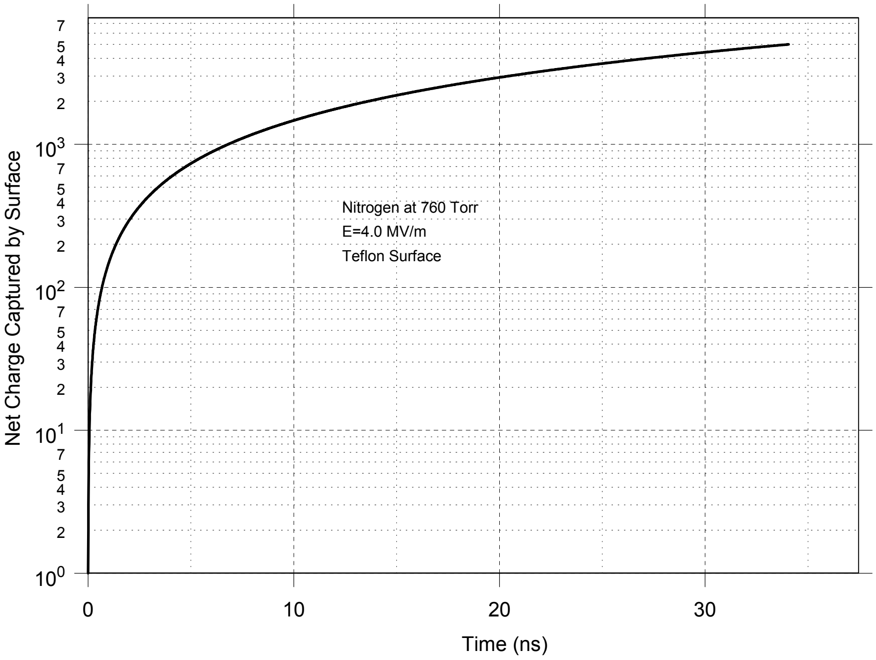

Figure 34. SEE charge captured vs. time.

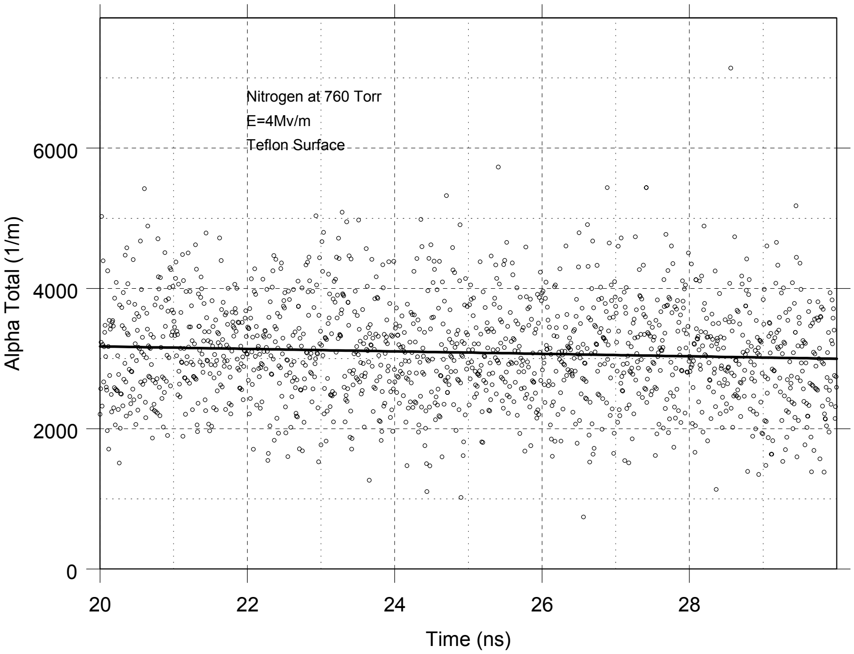

Figure 35. Ionization coefficient α vs. time.

E/p	α_{mc}/p	α_{raiz}/p
V-(cm-Torr)$^{-1}$	(cm-Torr)$^{-1}$	(cm-Torr)$^{-1}$
52.63 (4 MV/m at 760 T)	4.25×10^{-2}	4.73×10^{-2}
46.05 (3.5 MV/m at 760 T)	2.12×10^{-2}	2.24×10^{-2}
39.47 (3 MV/m at 760 T)	8.8×10^{-3}	8.3×10^{-3}
32.89 (2.5 MV/m at 760 T)	2.5×10^{-3}	2.1×10^{-3}

Table 11.Ionization coefficient α for N_2 without surface.

without a surface present. The results are shown in Table 11. Column 1 is E/p, column 2 is the result from BREAKDOWN and column 3 is the result of the fit function

$$\frac{a}{p} = Ae^{-(Bp/E)} \tag{159}$$

where for N_2, and for the range of E/p being examined here, $A = 8.8$ (cm-Torr)$^{-1}$ and $B = 275$ V-(cm-Torr)$^{-1}$ [2].

In order to match the Monte Carlo results to that of [2], we had to scale the N_2 cross-sections, which we obtained originally from Phelps [24]. We first replaced the momentum transfer cross section, which is more appropriate for use with a code based on the Boltzmann transport equation, with the total microscopic elastic collision scattering cross section, which is more appropriate for use with a Monte Carlo code. Using the original cross section scaling, the predicted value of α was too low (0.25 of the α given by [2] at $E/p = 52.63$ V-(cm-Torr)$^{-1}$). Our goal was reduce the probability of an inelastic collision and increase the probability of an elastic collision, which would cause the electron swarm to maintain a higher average energy and increase α. We also wanted to enhance the probability of an inelastic collision if it led to photon production because these photons could interact with the surface via photoemission. We, therefore, reduced all the vibrational cross sections (threshold energies between 0.29 eV and 2.35 eV) by changing the scaling parameter from 1.5 to 0.5. We enhanced the excitational cross sections (threshold energies between 6.17 eV and 13 eV) by changing the scaling parameter from 0.67 to 0.75 except for the cross sections that were originally scaled to 1.0 (A state vibrations 10 and above and $C^3\Pi$ state). We scaled the ionization cross-section by 1.37 to match the data from [25].

We add a surface made either of Teflon or of polyethylene and re-calculate the values of α/p for various values of E/p. Table 12 shows the results for Teflon and Table 13 for Polyethylene. Data in column 6 of both tables were calculated using Equation 157. The remaining columns were filled using Equation 158. The scatter of the values of α and the resulting variation with time of the linear fit function discussed in the previous section was accounted for by re-calculating the α of column 6 using Equation 158, finding the time where α matches the Equation 157 calculation and using the fit at that particular time for all the component $\alpha's$. Note that the α/p values for all field levels in Tables 13 and 12 are less than or equal to the values in Table 11 indicating a net loss of electrons as a result of the surface.

Assuming that all α fit the functional form of Equation 159, we determine new values of A and B. Let α_n be defined as the value of α when the field is set to E_n at a given pressure p. Then

$$B = -\frac{1}{p}\left[\frac{E_1E_2}{E_2 - E_1}\right]\ln\left(\frac{\alpha_1}{\alpha_2}\right)$$

$$A = \frac{\alpha_1}{p}e^{Bp/E_1}$$

Table 14 gives the values of A and B for a Teflon surface and Table 15 does the same thing for polyethylene.

E/p	α_{coll}/p	α_{pi}/p	α_{pe}/p	α_{see}/p	α/p
V-(cm-Torr)$^{-1}$	(cm-Torr)$^{-1}$	(cm-Torr)$^{-1}$	(cm-Torr)$^{-1}$	(cm-Torr)$^{-1}$	(cm-Torr)$^{-1}$
52.63	4.04×10^{-2}	7.63×10^{-4}	3.82×10^{-4}	1.95×10^{-3}	3.96×10^{-2}
46.05	2.06×10^{-2}	4.21×10^{-4}	3.42×10^{-4}	1.34×10^{-3}	2.00×10^{-2}
39.47	8.47×10^{-3}	1.71×10^{-4}	2.50×10^{-4}	6.18×10^{-3}	8.29×10^{-3}
32.89	2.62×10^{-3}	5.26×10^{-5}	1.84×10^{-4}	3.68×10^{-4}	2.50×10^{-3}

Table 12.Ionization coefficient α for N_2 with Teflon surface.

E/p	α_{coll}/p	α_{pi}/p	α_{pe}/p	α_{see}/p	α/p
V-(cm-Torr)$^{-1}$	(cm-Torr)$^{-1}$	(cm-Torr)$^{-1}$	(cm-Torr)$^{-1}$	(cm-Torr)$^{-1}$	(cm-Torr)$^{-1}$
52.63	4.28×10^{-2}	6.71×10^{-4}	9.45×10^{-3}	1.29×10^{-2}	4.00×10^{-2}
46.05	2.19×10^{-2}	5.00×10^{-4}	7.71×10^{-3}	9.96×10^{-3}	2.01×10^{-2}
39.47	9.18×10^{-3}	1.31×10^{-4}	5.86×10^{-3}	6.76×10^{-3}	8.42×10^{-3}
32.89	2.75×10^{-3}	3.95×10^{-5}	3.54×10^{-3}	3.79×10^{-3}	2.50×10^{-3}

Table 13.Ionization coefficient α for N_2 with polyethylene surface.

	A (cm-Torr)$^{-1}$	B V-(cm-Torr)$^{-1}$
α_{coll}/p	3.86	240
α_{pi}/p	6.63×10^{-2}	235
α_{pe}/p	1.29×10^{-3}	64
α_{see}/p	3.12×10^{-2}	146
α/p	3.93	242

Table 14.Ionization coeffient A and B parameters for Teflon surface.

	A (cm-Torr)$^{-1}$	B V-(cm-Torr)$^{-1}$
α_{coll}/p	4.17	241
α_{pi}/p	7.61×10^{-2}	249
α_{pe}/p	4.84×10^{-2}	86
α_{see}/p	1.00×10^{-1}	108
α/p	4.05	243

Table 15.Ionization coefficient A and B parameters for polyethylene surface.

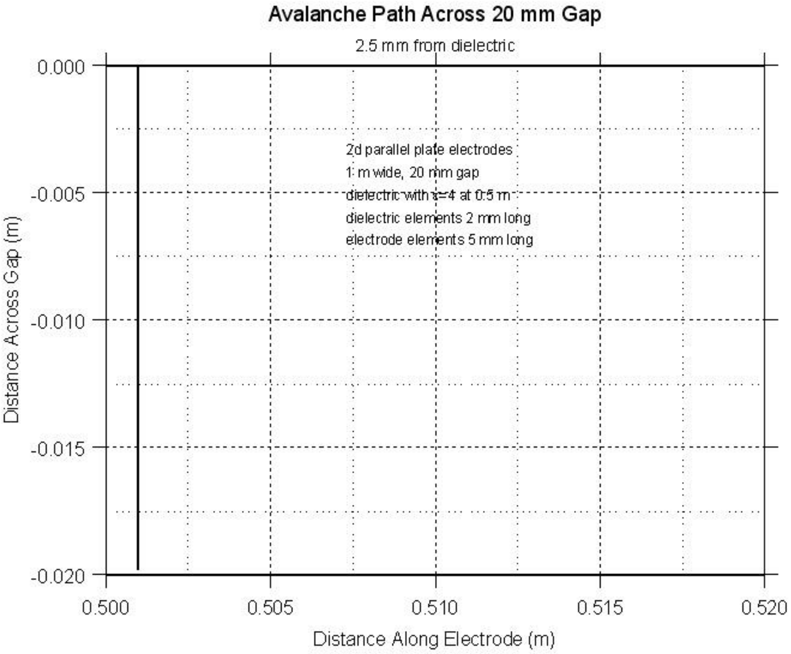

Figure 36. Avalanche path along dielectric surface.

6.3 Numerical Behavior of Field Next to Dielectric Surface

Knowing that α depends exponentially on the electric field value (see Equation 159) we must determine if all components of the electric field being calculated numerically by EIGER_S are well behaved next to a discretized dielectric surface or if there are some unanticipated singularities. To study this we solved for the field for two parallel-plate electrodes, infinite along $\widehat{y}$ and 1 meter along $\widehat{x}$. The electrodes are spaced 20 mm apart and half of the gap, between $x = 0$ to 0.5 m is filled by a dielectric with $\varepsilon_r = 4.0$. Figure 36 shows the path that the avalanche takes starting from the cathode, 2.5 mm from the dielectric surface and crossing the 20 mm gap.

Figure 37 shows the relative magnitude between two components of electric field 2.5 mm from the dielectric surface. The dielectric surface was discretized with 2 mm elements so there are no singularities or discontinuities due to basis function discretization.

7 CHARGED DIELECTRIC SURFACE

Monte Carlo investigations in the previous section did not find enhancements in avalanche growth on a dielectric surface when the process is initiated by a cloud of electrons as might be imagined in short pulse breakdown. However, if a continuous stream of electrons flow from the cathode region, as might be imagined from the cathode triple point (meeting of insulator, conductor, and gas) with static voltage excitation, there is a question about charges on the surface accumulating to such a degree that the global field in the gap is affected, perhaps enhancing avalanche growth and lowering breakdown thresholds. This section will investigate this case with Monte Carlo simulations. A reference will also be made to some

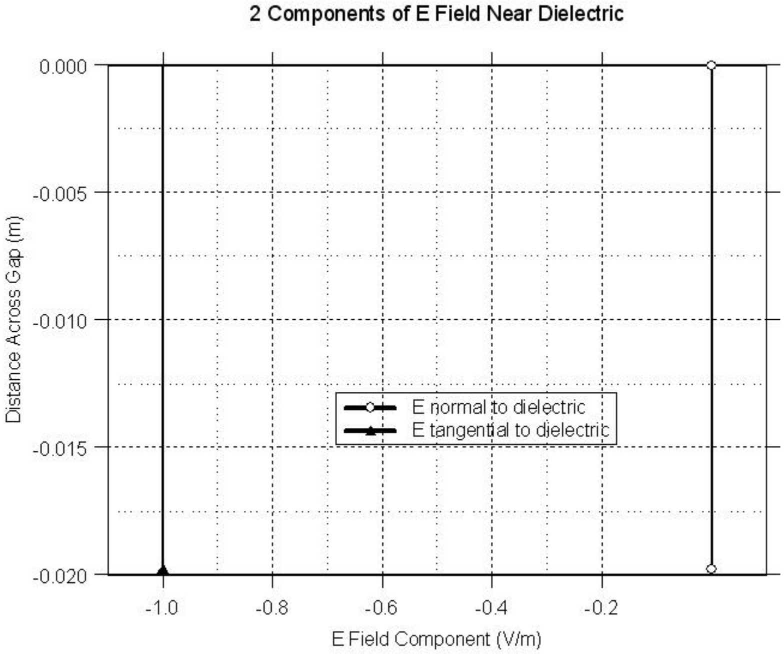

Figure 37. Electric field components near dielectric surface.

existing experimental data.

7.1 Simulations of Continuous Insulator Charging

In order to study the effect of a continuous stream of electrons from the cathode, we continuously added new electrons to the electron cloud throughout the simulation run-time. The electrons were added at locations uniformly distributed over a small half-sphere centered at the origin i.e., no electrons were added in the part of space filled by the dielectric. The electrons were released at uniform time intervals to simulate a specified current: 1 nA, 10 nA, 100 nA, and so forth.

If the imposed field is set to be significantly above the breakdown threshold (set, for example, at 4 MV/m at 760 Torr), the electrons sticking to the insulator in the vicinity of the origin do not have time to accumulate and significantly modify the field before the number of electrons in the volume begins to grow due to the avalanche process. Thus, at high fields the electrons due to the continuous source merely serve as seed electrons for the avalanche. The surface still captures the electrons due to secondary electron emission, but eventually, since there is a continuous source of electrons, one electron avoids sticking to the surface and begins the avalanche. We can, therefore, start these simulations using 10 electrons and 10 ions rather than the 1000 electrons and 1000 ions needed for simulations of short pulsed breakdown.

If the imposed field is set to be at, or slightly below threshold (set, for example, at 2.5 MV/m at 760 Torr), the electrons have enough time to accumulate on the surface and significantly modify the field in the vicinity of the origin (the triple-point location) before the number of electrons in the charge cloud grows due to the avalanche process. Figures 38 through 41 show results typical for either Teflon or polyethelene surfaces, with either 10 nA or 100 nA of continuous current, and either 2.5 MV/m or 3.0 MV/m imposed fields.

Secondary electron emission causes the electrons striking the surface to stick as in the short pulsed case, but the new electrons entering the simulation at the origin due to the continuous current source causes a large accumulation of negative charge near the origin. This is shown in Figure 38, which plots the positions of the wall electrons on a Teflon surface after 10 nA of continuous current has been applied in a 2.5 MV/m field for 116 ns. The continuous current is released within a hemisphere of radius 1.0 μm.

Figure 39 shows E_z at the location of every wall electron within z =20 μm of the origin. Within 1 μm, the total $\widehat{z}$ directed field decreases from the imposed 2.5 MV/m field to between 0.5 MV/m and 2 MV/m. Between 1 μm and 5 μm the $\widehat{z}$ directed field is enhanced.

Figure 40 shows E_x at the location of every wall electron. Within 1 μm of the triple-point, the field perpendicular to the surface has a similar magnitude to the imposed field and the direction is such that electrons are pushed away from the surface. The electrons in the volume, shown looking across the surface in Figure 41, demonstrate this tendency to be pushed off the surface. Charging the insulator due to continuous current tends to shield the triple point from the imposed field (at least for the component of the field along the surface) and limit further emission by the triple point. Further charging of the surface is limited by the tendency of the electrons to be pushed away from the surface.

7.1.1 Cathode Effects

In this section we examine the effect of a cathode on the electron cloud. The cathode was added by simply imaging the original charged particle in the cathode surface and imaging the dielectric image in the cathode surface. We did not allow any charged particles to be formed behind the cathode (due to photoionization or photoemission processes, for example) by eliminating any charged particle located in the region $z < 0$. We are also not including photoemission or ionic impact emission from the cathode (thus the

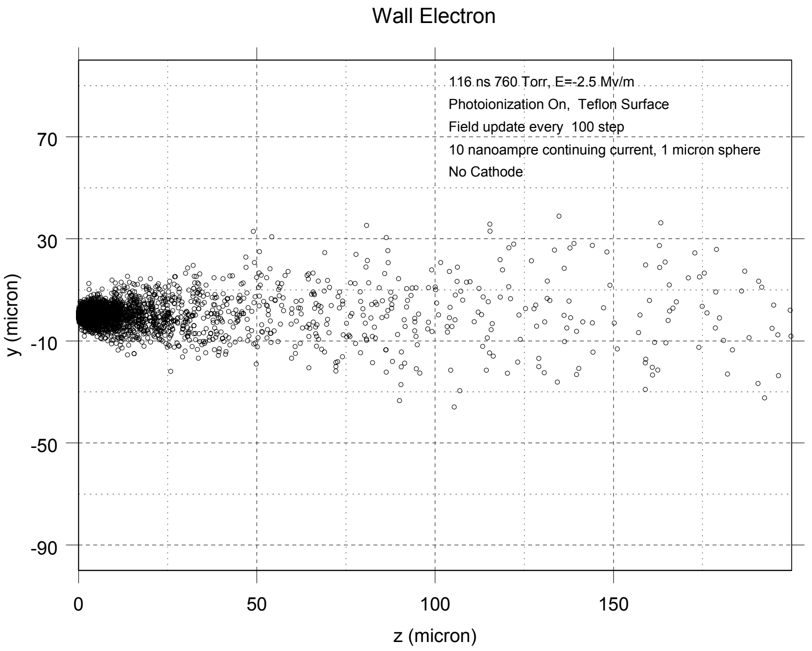

Figure 38. Distribution of wall electrons on Teflon surface.

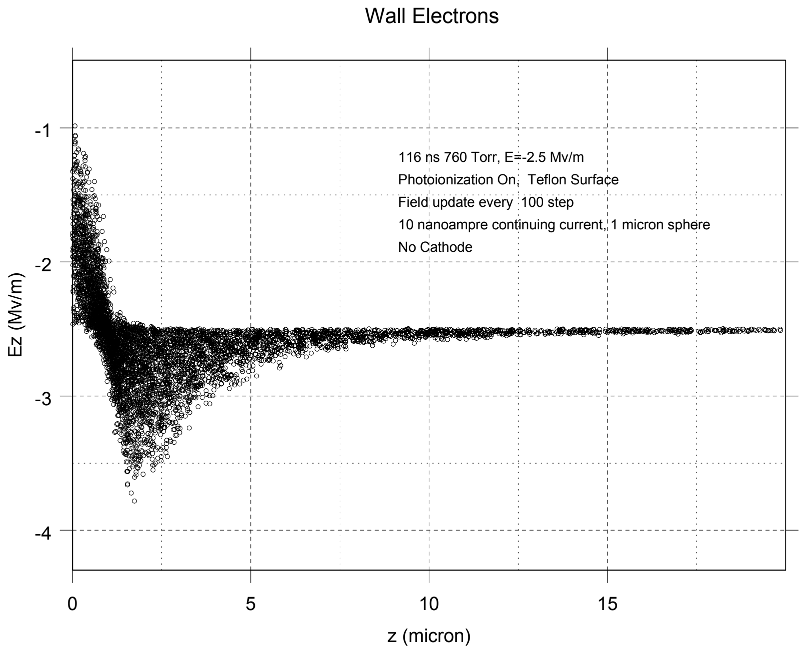

Figure 39. Total electric field parallel to Teflon surface.

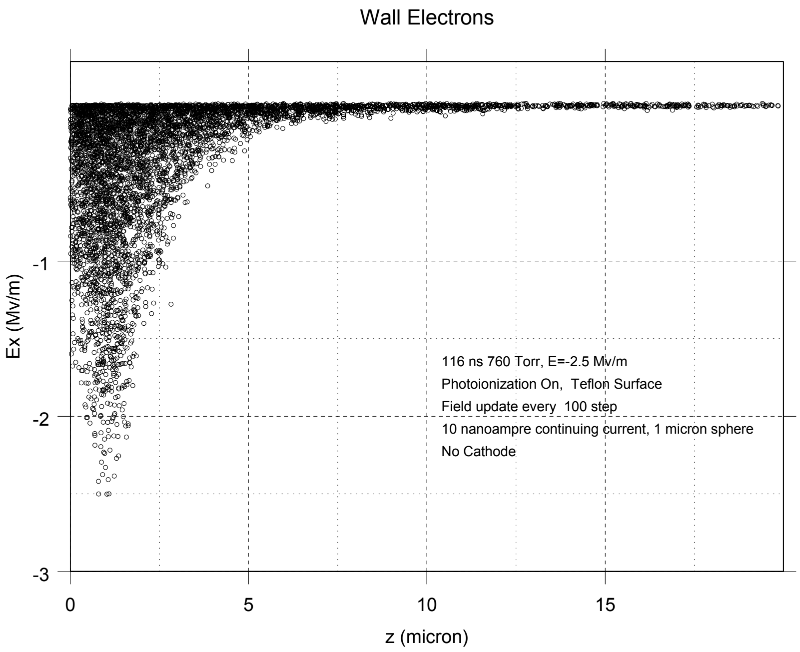

Figure 40. Total electric field perpendicular to Teflon surface.

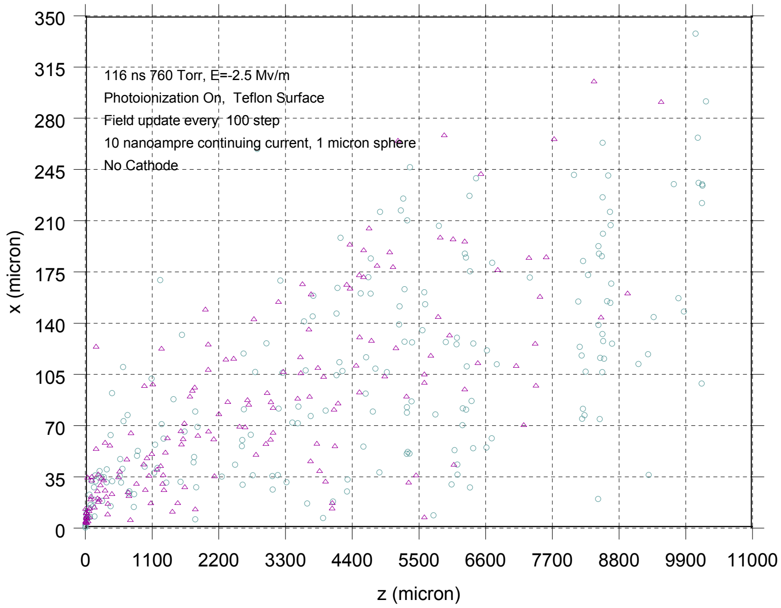

Figure 41. Side view of electron and ion cloud above the dielectric surface.

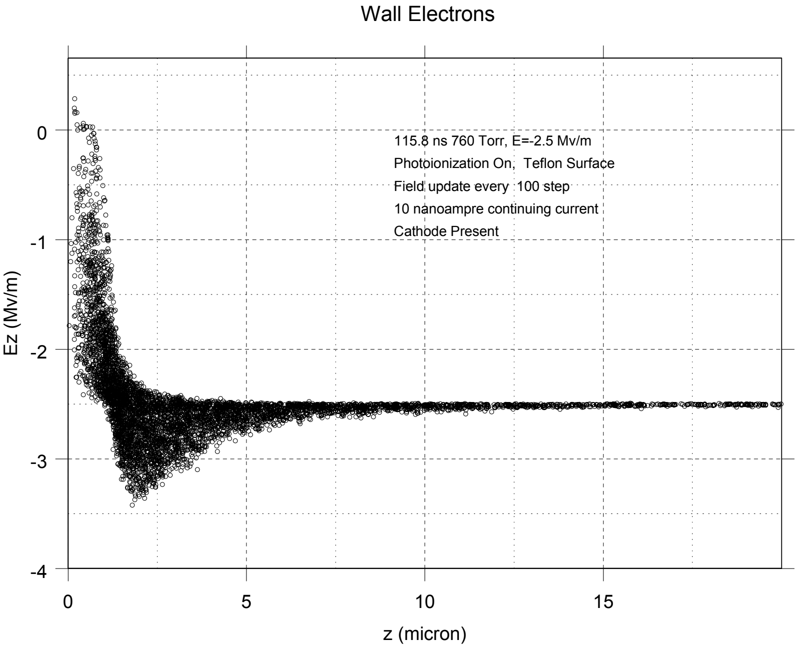

Figure 42. Total electric field parallel to Teflon surface.

continuous emission current must be thought of as an effective emission current).

The results, shown in Figures 42 through 44 show the same characteristics as the no cathode results except that E_x, the field tangential to the metal cathode goes to zero as it approaches the conductor.

The region where the accumulated electrons affected the field was quite thin in the previous cases (1 μm), which might be dwarfed by the physical size of the triple point. To check what determined the thickness of this region, we released the continuous current of electrons in a larger radius hemisphere (5 μm). The results are shown in Figures 45 and 46. The region where the z directed field is reduced and x directed field is present has increased to 5 μm. The continuous current was set at 100 nA. The field levels are not as high as previous results because we are looking at an earlier time (68 ns vs. 116 ns). We have focused on emission points near the cathode in these simulations. Emission points down toward the anode side have not been studied.

7.2 Low Frequency Breakdown of Insulator Gaps

Some existing data can be found on the breakdown of insulators in air. Figure 47 shows the low frequency breakdown voltages of a uniform field gap with and without a cylindrical insulator. The ideal insulator does not perturb the field and yet we see a dramatic drop in voltage with it present. The effect is attributed to surface charging, and surface contamination (layers of gas, moisture, dust).

In fact the original reference [26] attributes much of the reduction to humidity. Figure 48 shows this pronounced effect of humidity on insulator surface breakdown at atmospheric pressure.

Some recent measurements on Lexan and alumina insulators have tended to confirm that humidity is a

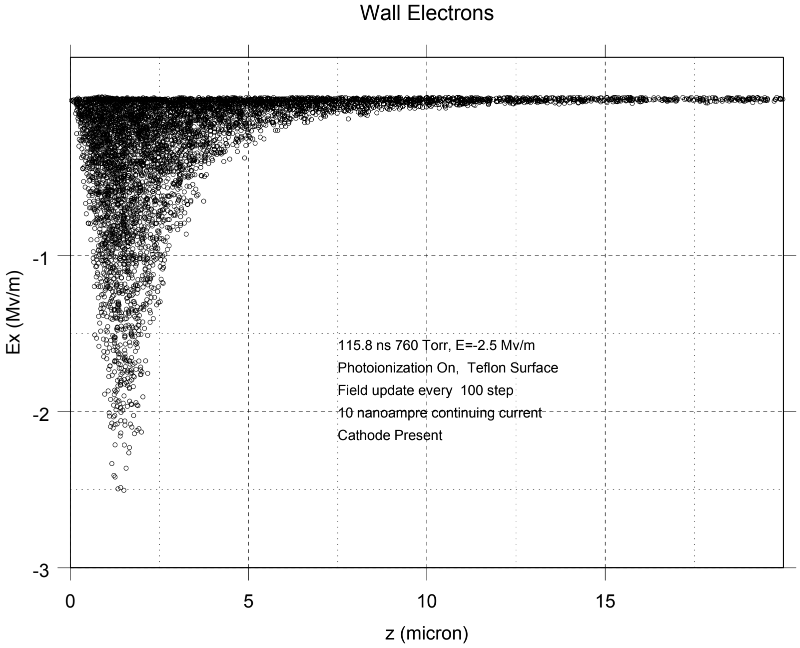

Figure 43. Total electric field perpendicular to Teflon surface.

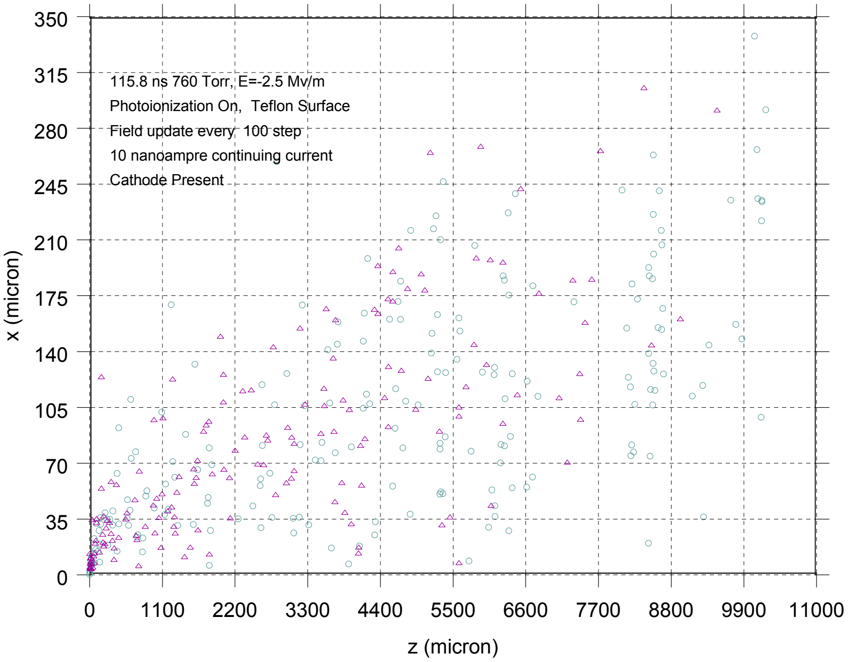

Figure 44. Side view of electron and ion cloud above the dielectric surface.

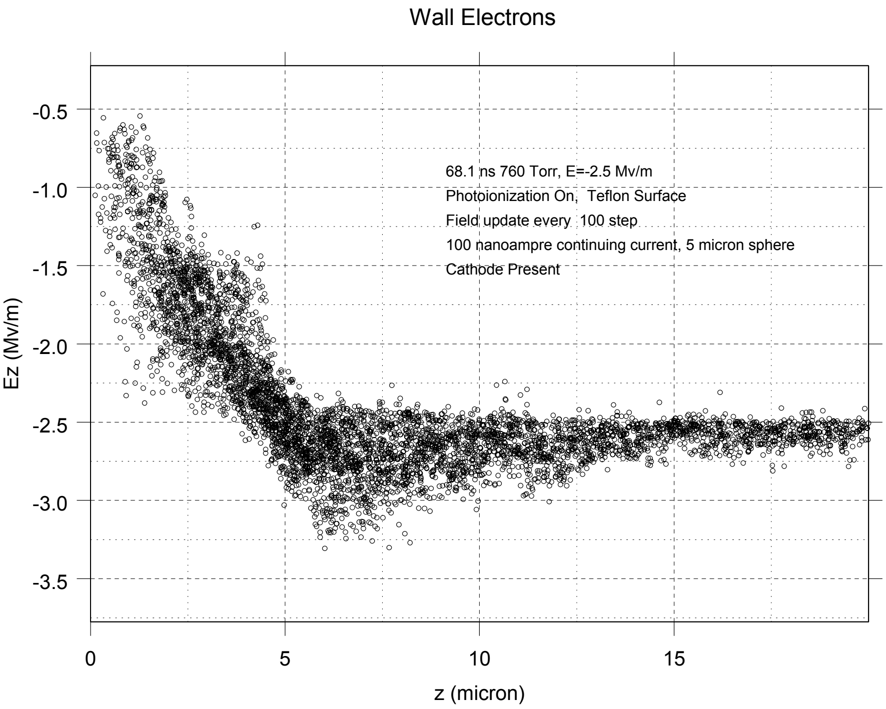

Figure 45. Total electric field parallel to Teflon surface.

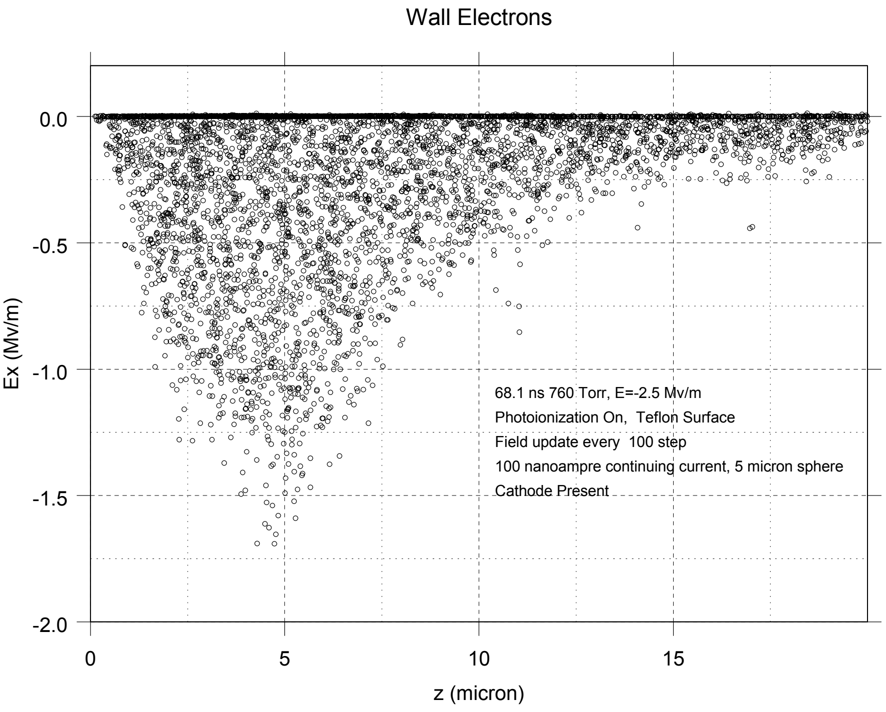

Figure 46. Total electric field perpendicular to Teflon Surface.

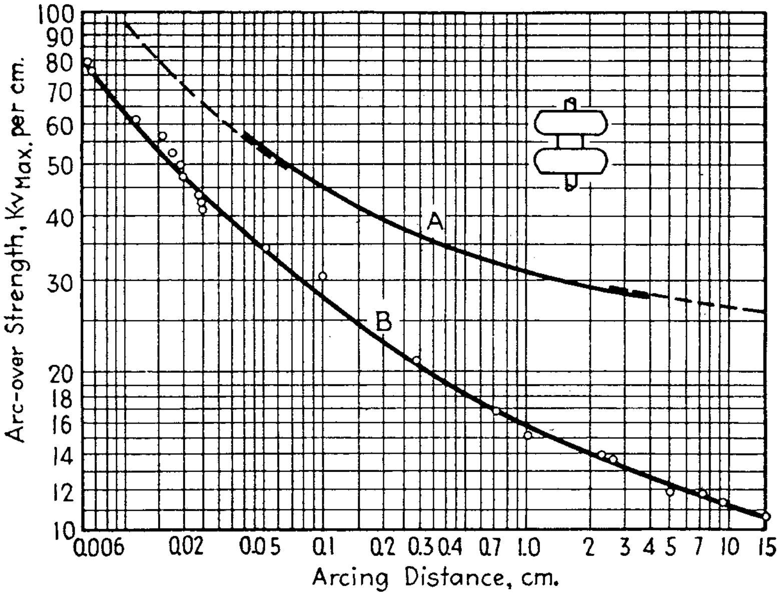

FIG. 7.9.—Effect of insulation on breakdown strength of air for parallel plates. (*A*) Air; (*B*) Right cylinder of glass, Pyrex, or porcelain placed as shown in insert (20°C, 760 mm. Hg, 60 cycles).

Figure 47. Low frequency breakdown of an insulating surface in air (from "Gaseous Conductors, J. D. Cobine [13]).

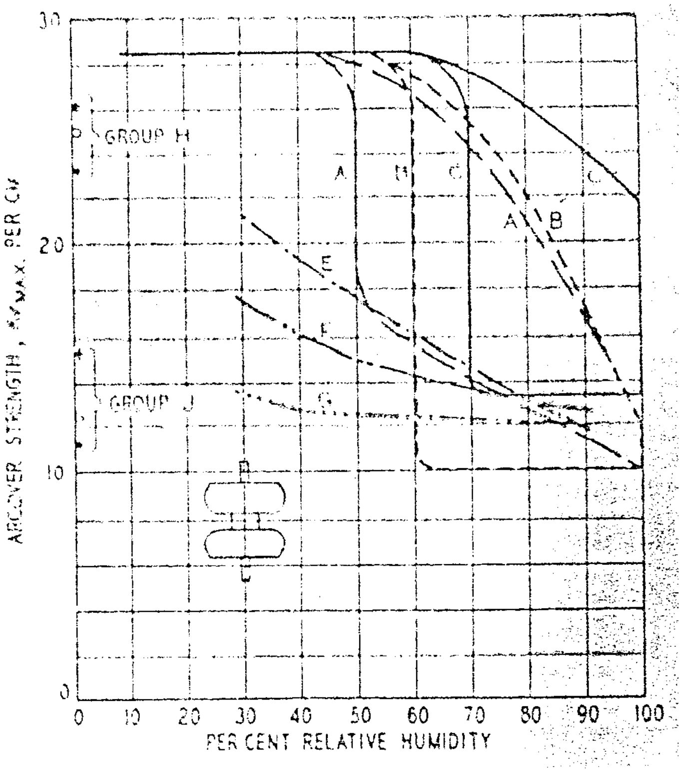

Fig. 2. Effect of relative humidity on arcover strength

Curve A. Paraffine right cylinder, Rogowski[2] electrodes, sparking distance 3.0 cm 50 cycles, series resistance 400,000 ohms, 45 to 20 deg C, 76 cm, absolute humidity constant at 1.8 cm mercury; from Ritz.[3] The uppermost horizontal line of curves A, B, and C corresponds to the strength of the air gap alone

Curve B. Glass right cylinder, conditions as for A; from Ritz

Curve C. Bakelite right cylinder, conditions as for A; from Ritz

Curve E. Paraffine right cylinder, flat electrodes with rounded edges; sparking distance 3.0 cm, 50 cycles, 20 deg C, 76 cm; from Schwaiger[5]

Curve F. Glass and unglazed porcelain right cylinders, conditions as for E; from Schwaiger

Curve G. Shellac right cylinder, conditions as for E; from Schwaiger

Points, Group H. Paraffine right cylinder, flat electrodes with curved edges of 20 cm radius; sparking distance 3.0 cm, 20 deg C, 76 cm. Upper point, surge voltage (wave form not given); middle point continuous; lower point 50 cycles; from Inge and Walther[11]

Points, Group J. Glass right cylinder, conditions as for H; from Inge and Walther

Figure 48. Effects of humidity on insulator surface breakdown in air (from "Insulator Arcover in Air," F. W. Maxstadt [26]).

major player in reduced surface breakdown.

8 CONCLUSIONS

An ionization coefficient approach has been used in conjunction with an existing electrostatic code to determine the voltage threshold of electrical breakdown between conductors. The electrostatic code is a boundary element code capable of modeling complex geometries including the presence of dielectric materials. The ionization coefficient approach has focused on volumetric breakdown in the gas.

The breakdown condition in a nonuniform field was setup. The left hand side is the integral of the primary ionization coefficient over the gap between electrodes. Fits of the ionization coefficient versus electric field magnitude were assembled for air and two other gases of interest in stronglinks. An adaptive field tracking algorithm was implemented in the post processor of the electrostatic code to perform the integral of the ionization coefficient along an electric field line (as well as other user defined paths). Diffusion of the electron swarm across field lines (thus defining a new effective path of integration) is not treated in this report.

The right hand side of the breakdown condition quantifies secondary electron emission and the resulting avalanche growth. Both the Townsend regime (cathode emission) and the streamer regime (gas emission) were addressed. Both ion and photon impact were discussed in the Townsend regime. The fit function was motivated by the case of photon impact, which is thought to be dominant at high pressures (except in inert gases where a formula for ion impact emission was used). Use of uniform field air breakdown data allowed us to estimate parameters associated with photon emission efficiencies and absorption coefficients. The Raether streamer criterion (right hand side at streamer threshold) was matched to the Townsend criterion to determine a distance for which the right hand side definition switches between the two regimes. The impact of surface conditions (oxidation, roughness, etc.) on the secondary coefficient was not addressed, and is in fact seldom found specified in breakdown data.

The resulting breakdown condition was applied to several nonuniform field geometries for purposes of verification and validation. Sphere - sphere electrodes were examined first. This is a symmetrical geometry for which an analytic solution is available for verification. Convergence studies established the fact that errors in field quantities (such as the surface electric field) could be reduced to negligible amounts (less than one percent). Experimental data for this geometry also allowed some validation comparisons. These data were available for somewhat nonuniform geometries (aspect ratios of spacing to radius less than four). Errors from one to five percent were observed in the comparisons.

Cylinder - cylinder (wire - wire) electrodes were examined second. Again this is a symmetrical geometry for which an analytic solution is available for verification. EIGER_S can model two or three dimensional geometries and the two dimensional capability was used in this case. Errors in breakdown voltages predicted in the simulations and analytic calculations were reduced to about one percent. Experimental data were again available for validation purposes. These data were available for large aspect ratios (ratios of spacing to radius of more than two hundred were available). Aspect ratios for which spark breakdown occurs before corona (less than thirty) resulted in errors of ten to fifteen percent. Larger aspect ratios resulted in errors forty percent and up. The reason for these rapidly growing errors is that the breakdown condition alone does not discriminate between spark or corona, whereas, the experimental data was for spark breakdown only.

A coaxial geometry was examined next. This is an asymmetrical geometry for which a simple analytical solution is available. Errors in the breakdown predicted by the simulations and analytic calculations differed by less than one percent. Experimental data were also available over fairly broad aspect ratios. The case of small aspect ratio (one point five) resulted in less than one percent error. The higher aspect ratio (eleven point five) resulted in a fourteen percent error and some small experimental polarity differences (which are not modeled by the present breakdown condition). Experimental data was available in this last case for corona inception voltage as well as spark breakdown. The error with respect to corona inception voltage was reduced to eight percent (the polarity dependence was also reduced).

Next an asymmetrical corner geometry was examined to see the effect of edges, which are frequently encountered in stronglink switches. A right angle corner was examined in some detail although analytic solutions were setup for arbitrary angles. Experimental data was not available. Because of the field singularity which occurs at an edge, combined with the sensitivity of the primary ionization coefficient with field magnitude, errors between the simulations and analytic solutions could not be reduced to negligible levels without exceedingly fine gridding of the edge region. This problem was solved by including a sub-cell approach in the integration: very near the edge an analytic integration is performed with the field normalized by the numerical simulation at a small but reasonable distance from the edge (for which the simulation field is accurate). The integration was then continued in the numerical simulation away from the edge. One result of interest was found. The ionization integral at the edge exceeds the value away from the edge (in the parallel plate, uniform field, region) only for gaps exceeding a certain distance (one third of a millimeter at atmospheric pressure). For fixed secondary emission (which is not really the case), this implies that edges are the likely breakdown point only for gaps exceeding this minimum value.

Finally an asymmetrical three dimensional rod-to-plane geometry was examined. Rod geometries are frequently found in switches. An analytical approximation was constructed for verification purposes. Comparisons between simulation and analytical breakdown results were quite close but differed from experimental data except at the smallest gap spacings. Here again the experimental data was for spark breakdown.

Thus, to summarize: 1) an ionization coefficient approach to predicting gas breakdown was implemented in an existing, general purpose, electrostatic code; 2) several canonical examples of nonuniform field breakdown (that included features encountered in stronglink geometries) were simulated and compared to analytical calculations and experimental data, with reasonable agreement for limited aspect ratios (gap to electrode radius); 3) a sub-cell algorithm was implemented to treat edges; 4) several deficiencies were also noted.

The transition between corona (localized breakdown) and spark (global breakdown) is important because in the former case the current is limited to quite small levels, whereas in the latter case the current is typically limited only by the external circuit parameters. The problem is quite complex, in general, with space charge effects and leader phenomena (in long gaps) playing a role. In nonuniform fields the breakdown condition is dominated by the field enhanced region about a small radius of curvature electrode. We therefore proposed a simple additional criterion based on the minimum field in the gap to give some estimate of whether a streamer will penetrate the low field region and transition to spark. We made use of the minimum streamer sustaining field in the criterion. This method was used in the two-dimensional coaxial and three dimensional rod-to-plane geometries and appeared to predict sparking thresholds in air with reasonable accuracies compared to the experimental data. Transient considerations involved in deciding whether the streamer can expend energy and make it through relatively thin low field regions, as well as space-charge effects and leader processes were out of scope and not treated. Very small gaps where the Townsend process replaces the streamer process were also not treated.

The microscopic processes of secondary electron emission and photoemission from a dielectric surface that were incorporated into a Monte Carlo code in a previous LDRD project were used to examine the impact of an uncharged dielectric surface on avalanche growth. Secondary electron emission from electron impact is a major player in vacuum breakdown across insulators. Photoemission was thought to be a possible player at higher pressures and lower fields because lower energy photons (incapable of direct ionization of the gas but capable of liberating electrons from the insulator) vastly out-number high energy photons. Near atmospheric pressure electron energies are in a range where secondary electron emission from electron impact leads to incident electron attachment and eventual surface charging. The simulations that were run indicated that this capture led to a slight reduction of avalanche growth near the surface and thus no apparent lowering of pulsed breakdown voltage.

Finally the case where a continuous stream of electrons is injected, to charge the dielectric surface, is simulated. This case mimics the situation where a continuous cathode emission takes place, say, at the cathode triple junction, with static voltage excitation. A conducting boundary was introduced into the simulation by an image to represent the cathode. The simulations were carried out with field levels slightly below uniform field gas breakdown levels. It was found that electron attachment to the insulator occurs first near the cathode. The levels of local charge accumulation are sufficient to significantly reduce the field in the neighborhood of the cathode. It appears that this reduction is substantial enough to reduce emission from typical cathode triple junctions, thus terminating the charging process before global charging causes significant changes in the gap field structure. Low frequency experiments reported in the literature indicate that for clean dry surfaces, breakdown voltages are similar to levels in the gas alone. These results thus appear to be consistent with the view emerging from the simulations. New experiments on Lexan and alumina surfaces with gaps of less than one centimeter indicate similar behavior.

The purpose of the dielectric surface simulations was to provide some theoretical underpinning for the treatment of insulator surfaces in the ionization breakdown code. So far the indication is that we can treat the avalanche growth in the same way as if it takes place in the gas.

9 REFERENCES

[1] E. Nasser, *Fundamentals of Gaseous Ionization and Plasma Electronics*, New York: Wiley-Interscience, 1971.

[2] Y. P. Raizer, *Gas Discharge Physics*, New York: Springer-Verlag, 1997.

[3] E. M. Bazelyan and Y. P. Raizer, *Spark Discharge*, New York: CRC Press, 1998.

[4] E. E. Kunhardt and L. H. Luessen (editors), *Electrical Breakdown and Discharges in Gases*, Parts A and B, New York: Plenum Press, 1983.

[5] A. N. Lagarkov and I. M. Rutkevich, *Ionization Waves in Electrical Breakdown of Gases*, New York: Springer-Verlag, 1994.

[6] J. M. Meek and J. D. Craggs, *Electrical Breakdown of Gases*, Oxford: Clarendon Press, 1953.

[7] J. M. Meek and J. D. Craggs (editors), *Electrical Breakdown of Gases*, New York: John Wiley & Sons, 1978.

[8] A. von Engel, *Ionized Gases*, Oxford: Clarendon Press, 1965.

[9] F. Llewellyn-Jones, *Ionization and Breakdown in Gases*, London: Methuen & Co. LTD, 1957.

[10] F. Llewellyn-Jones, *Ionization Avalanches and Breakdown*, London: Methuen & Co. LTD, 1967.

[11] G. Francis, *Ionization Phenomena in Gases*, London: Butterworths Scientific Pub., 1960.

[12] E. Kuffel, W. S. Zaengl, and J. Kuffel, *High Voltage Engineering: Fundamentals*, Boston: Newnes, 2000.

[13] J. D. Cobine, *Gaseous Conductors*, Dover, New York, 1958, p. 166.

[14] L. L. Alston, *High Voltage Technology*, Oxford University Press, 1968.

[15] F. W. Peek, *Dielectric phenomena in High Voltage Engineering*, New York: McGraw-Hill Book Co., Inc., 1915.

[16] J. Dutton, “A Survey of Electron Swarm Data”, J. Phys. Chem. Ref. Data, Vol. 4, No. 3, 1975.

[17] W. R. Smythe, *Static and Dynamic Electricity*, New York: Hemisphere Pub. Corp., 1989.

[18] R. C. Weast (editor), *Handbook of Chemistry and Physics*, 55th edition, CRC Press, 1975, Cleveland, p. E-55.

[19] G. W. C. Kaye and T. H. Laby, *Tables of Physical and Chemical Constants*, Longman Scientific&Technical, 1989.

[20] L. B. Loeb, *Electrical Coronas*, Berkeley, CA: University of California Press, 1965.

[21] L. K. Warne and K. C. Chen, "Effective Impedance of Bolt Loads on Narrow Slot Apertures Having Depth," Journal of Electromagnetic Waves and Applications, Vol. 6, No. 7, pp. 891-910, 1992.

[22] R. E. Jorgenson, L. K. Warne and E. E. Kunhardt, "Lightning Induced Arcing: An LDRD Report," *Sandia Report SAND2000-3044*, Dec. 2000.

[23] R. E. Jorgenson, L. K. Warne, A. A. Neuber, J. Krile, J. Dickens, H. G. Krompholz, "Effect of Dielectric Photoemission on Surface Breakdown: An LDRD Report," *Sandia Report SAND2003-1731*, May 2003.

[24] A. V. Phelps, "A compiliation of collision cross-sections for various gases" available via anonymous FTP from jila.colorado.edu in the directory /collision_data

[25] Y.-K. Kim, K. K. Irikura, and M. E. Rudd, D.S. Zucker, M.A. Zucker, J.S. Coursey, K.J. Olsen, and G.G. Wiersma, http://physics.nist.gov/PhysRefData/Ionization/xsection.html

[26] F. W. Maxstadt, "Insulator Arcover in Air," Elec. Eng., 53, pp. 1062-1068, July 1934.

[27] E. A. Burke, "Secondary Emission from Polymers," IEEE Transactions on Nuclear Science, Vol. NS-27, no. 6, Dec. 1980, pp. 1760-1764.

Distribution:

5	MS1152	R. E. Jorgenson, 01642
10	MS1152	L. K. Warne, 01642
1	MS1152	M. L. Kiefer, 01642
1	MS1152	J. D.. Kotulski, 01642
1	MS1152	M. F. Pasik, 01642
1	MS1152	M. E. Morris, 01642
1	MS1152	M. Caldwell, 01643
1	MS1152	M. A. Dinallo, 01643
1	MS0319	R. E. Kreutzfeld, 02613
2	MS0319	S. D. Nicolaysen, 02613
1	MS0319	C. R. Sorensen, 02613
1	MS0319	J. Brown, 02613
1	MS0316	H. P. Hjalmarson, 09235
1	MS0828	M. Pilch, 09133
1	MS0139	S. E. Lott, 09905
1	MS0405	K. O. Merewether, 12333
1	MS0492	K. C. Chen, 12332
1	MS9018	Central Technical Files, 8945-1
2	MS0899	Technical Library, 09616